# Carl von Ossietzky Universität Oldenburg

# Selective Recognition by Nanoparticle-Imprinted Thin Films

## (Selektive Erkennung durch Nanopartikel-geprägte Dünnschichten)

Von der Fakultät für Mathematik und Naturwissenschaften

der Carl von Ossietzky Universität Oldenburg

zur Erlangung des Grades und Titels eines

Doktors der Naturwissenschaften (Dr. rer. nat.)

angenommene Dissertation

von Frau **Sweety Ann Samuel**, M.Sc.

geboren am 25 April 1994 in Kerala, India

Oldenburg, July 2024

Erstgutachter: Prof. Dr. Gunther Wittstock

Zweitgutachterin: Prof. Dr. Katharina Al-Shamery

# Abstract

As the utilization of artificial nanoparticles (NPs) continues to rise, there is a growing need for analytical tools capable of not only detecting NPs but also distinguishing them based on properties influencing their toxicological potential. These properties include the chemical composition of the core and ligand shell, as well as size, shape, and specific interactions with biological interfaces. Nanoparticle-imprinted matrices (NAIM) are a recent concept for detecting and sensing NPs by considering their size, shape, and surface charge. Like molecularly imprinted polymers (MIP), NAIM involves creating a polymeric matrix around template NPs attached to a substrate. After removing the template NPs, complementary cavities are formed, enabling selective capture of analyte NPs with comparable size and shape to the original templates.

In contrast to the previous NAIM systems, where conducting template NPs were used, insulating template NPs like carboxyl and amine-modified silica ($SiO_2$) NPs, and sulfate-modified polystyrene (PS) NPs are used in this thesis to imprint the cavities. This enables the removal of the template and the detection of analyte NPs through orthogonal methods. The thorough removal of template NPs and the resulting cavities were investigated using scanning electron microscopy (SEM) and atomic force microscopy (AFM). This thesis outlines various methods for tuning the matrix to enhance its affinity for the analyte NPs. This was achieved through the electrodeposition of matrices with beneficial functional groups or through post-covalent modification of the matrix. The quantification of analyte NPs within the cavities was determined through the charge transferred during the electrodissolution of analyte NPs using linear sweep voltammetry (LSV). The uptake depends on factors such as the functional groups present in the matrix, covalent modification, the pH during uptake, and the size matching of the template and analyte NPs. The electrodeposition and covalent modification of the matrix were examined with cyclic voltammetry (CV), and the presence of functional groups in the film was validated through X-ray photoelectron spectroscopy (XPS).

# Zusammenfassung

Weil die Verwendung von künstlichen Nanopartikeln (NPs) weiter zunimmt, besteht ein wachsender Bedarf an Analysewerkzeuge, die NPs nicht nur nachweisen, sondern auch nach denjenigen Eigenschaften unterscheiden können, die ihr toxikologisches Potenzial beeinflussen. Zu diese Eigenschaften gehören die chemische Zusammensetzung des Kerns und der Ligandenhülle sowie die Größe, Form und spezifische Wechselwirkungen mit biologischen Grenzflächen. Die mit Nanopartikeln bedruckten Matrizen (NAIM) sind ein neueres Konzept für den Nachweis und die Erkennung von NPs unter Berücksichtigung ihrer Größe, Form und Oberflächenladung. Ähnlich wie bei molekular geprägten Polymeren (MIP) beinhaltet das NAIM-Konzept die Schaffung einer polymeren Matrix um Templat-NPs, die an einem Substrat gebunden sind. Durch Entfernen der Templat-NPs werden komplementäre Kavitäten gebildet, die einen selektiven Aufnahme von Analyt-NPs mit vergleichbarer Größe und Form wie die ursprünglichen Template ermöglichen.

Im Gegensatz zu den bisherigen NAIM-Systemen, bei denen elektrisch leitfähige Template-NPs zum Einsatz kamen, werden in dieser Arbeit isolierende Templat-NPs wie Carboxyl- und Amin-modifizierte Siliziumdioxid-NPs ($SiO_2$) und Sulfat-modifizierte Polystyrol-NPs (PS) zur Prägung der Kavitäten verwendet. Dies ermöglicht die Entfernung der Template und die Detektion von Analyt-NPs durch orthogonale Methoden. Die gründliche Entfernung der Templat-NP und die Bildung der entstandenen Kavitäten wurden mit Hilfe der Rasterelektronenmikroskopie (SEM) und der Rasterkraftmikroskopie (AFM) untersucht. In dieser Arbeit werden verschiedene Methoden zur Einstellung der Matrix beschrieben, um ihre Affinität für die Analyt-NP zu erhöhen. Dies wurde durch die elektrolytische Abscheidung von Matrizen mit vorteilhaften funktionellen Gruppen oder durch nachträgliche kovalente Modifikation der Matrix erreicht. Die Quantifizierung der Analyt-NP in den Kavitäten wurde durch den Ladungstransfer während der elektrolytischen Auflösung der Analyt-NP unter Verwendung der linearen Sweep-Voltammetrie (LSV) bestimmt. Die Aufnahme hängt von Faktoren wie den in der Matrix vorhandenen funktionellen Gruppen, der kovalenten Modifikation, dem pH-Wert während der Aufnahme der Analyt-NPs und der Größenübereinstimmung von Templat- und Analyt-NPs ab. Die elektrolytische Abscheidung und die kovalente Modifikation der Matrix wurden mit Cyclovoltammetrie

(CV) untersucht, und das Vorhandensein funktioneller Gruppen im Film wurde durch Röntgen-Photoelektronenspektroskopie (XPS) validiert.

# Acknowledgement

# Table of Contents

# 1    Introduction

As per the International Organization for Standardization (ISO) definition, nanoparticles (NPs) are exceptionally fine particles, with at least one dimension falling within the range of 1 to 100 nanometers.[1] Owing to their small size and remarkable surface area-to-volume ratio,[2] NPs exhibit diverse physical and chemical characteristics setting them apart from their bulk counterparts. Consequently, they have gained substantial attention for a broad spectrum of applications. Depending on their chemical composition, NPs can be categorized into various types, including metal NPs, semiconductor NPs, ceramic NPs, carbon-based NPs, and polymeric NPs, among others. These NPs find extensive use in a wide array of applications, serving as effective adsorbents,[3] carriers for drug delivery,[4–6], fillers,[7,8] components in electronics,[8–11] additions to food industry,[9] ingredients in cosmetics, plasmonic absorbers,[12–15] and catalysts,[8,16,17] to name just a few. This widespread usage of NPs raises concerns about the uncontrolled release of NPs to the ecosphere, where they may have toxic effects that are different than those of the corresponding bulk chemicals. Nanotoxicology has emerged as a scientific discipline dealing with the toxicity of NPs and the specific way in which nanosized matter interacts with living organisms.[18–24]

The physical and chemical properties like size, shape, and ligand shells define the toxicity of NPs.[7,25–27] Through dermal contact, ingestion, or inhalation, NPs can enter biological organisms and can cause inflammation, oxidative stress in the lungs, and can damage the epithelial cells.[28] For example, developmental toxicity, genotoxicity, membrane damage, and cytotoxicity[29] are several potential adverse effects upon exposure to silver NPs. Studies have shown that silver NPs of 20 nm in diameter are more hazardous than larger NPs.[29] Likewise, the ligand shells on the NP surface profoundly influence the toxicity of NPs.[27] The ligand shell of NPs can interact with biological cells via the surface charge, thereby disrupting the cell structure leading to cellular death. It can also induce the formation of reactive oxygen species which are toxic to the cells when it exceeds the ambient concentration within the cells.[27,30]

In light of these considerations, an increasing need has arisen for analytical tools capable of identifying and distinguishing NPs based on the factors that influence

their potential for toxicity. Recent research has explored numerous detection and analysis methods, such as optical techniques involving light scattering [31–33], electrical diffusion charging [34], and electrochemical detection via nanoparticle collision[35–37]. Nonetheless, there remains a demand for sensing tools that can effectively respond to the size, shape, and surface charge of NPs while being simultaneously simple, cost-effective, and user-friendly.
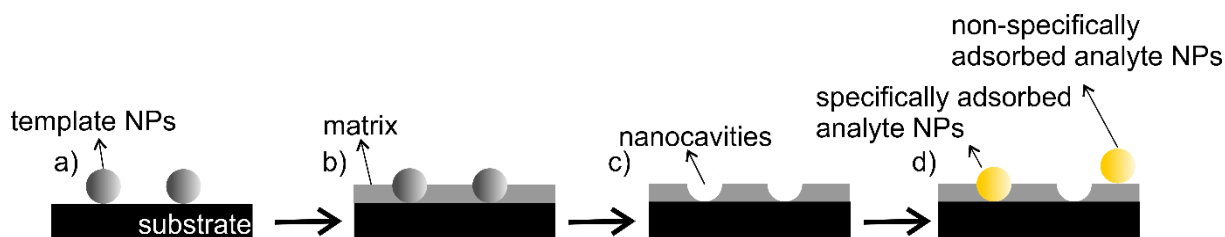


Figure 1. Schematics of the NAIM system. a) substrate after the attachment of template NPs, b) formation of the matrix around the template NPs, c) removal of template NPs forming complementary cavities and c) NAIM system after the exposure to analyte NPs.

The recent development of nanoparticle-imprinted matrices (NAIM) represents an innovative approach for the detection and sensing of NPs based on their size, shape, and surface charge characteristics.[38–43] This concept is analogous to the well-established concept of molecularly imprinted polymers (MIP).[44–47] In essence, a polymeric matrix is created around the template NPs, firmly attached to a substrate. Subsequent removal of the template NPs results in the formation of complementary cavities, designed to capture analyte NPs with similar size and shape as the original template NPs, as shown in the schematics in Figure 1. Research into NAIM systems has unveiled various factors influencing their remarkable uptake capability. One crucial parameter is the thickness of the matrix, which should not exceed the radius of the template NPs to prevent incomplete template NP removal or the formation of indistinct cavities.[41,48]

The term "specific adsorption" is used to describe those NPs situated within the cavities, while "non-specific adsorption" refers to NP attachment to the NAIM-solution interface outside of imprinted cavities (Figure 1). When NAIM films are considerably thinner than the radius of the template NP, distinguishing specific from non-specific uptake becomes more challenging, both in terms of binding strength and potential detection methods. Additionally, the chemical composition of the matrix plays a significant role in NAIM selectivity. For instance, the uptake potential of a *p*-

2

aryldiazonium-based matrix is notably influenced by the functional groups located at the *p*-position, while slight alterations in the stabilizing shell around Au NPs can have a substantial impact on their recognition by a *p*-carboxyphenyldiazonium-based matrix.[40,48].

Advancements in NAIMs can be significantly enhanced through the application of electrochemical techniques, offering precise control over matrix thickness in the nanometer range through methods like electropolymerization and electrografting.[49] Electrochemical approaches such as cyclic voltammetry (CV), chronoamperometry (CA), or linear sweep voltammetry (LSV) are cost-effective means for detecting metallic NPs via electrodissolution (read-out).[38] NAIM systems featuring electropolymerized polyphenol or electrografted diazonium-based matrices have been studied and have demonstrated stability during subsequent handling steps.[40,41,48]

This thesis places its central emphasis on developing a robust preparation protocol, which involves simultaneously producing thin films and facilitating flexible tuning for functional groups and addressing the challenges related to preserving structural rigidity, maintaining cavity shape, and achieving selective targeting of nanoparticle populations. In this thesis, NAIM systems were developed integrating insulating template NPs alongside conducting analyte NPs. The research used a combination of microscopic, electrochemical, and spectroscopic techniques for characterizing the NAIM system. The deposition of the film, along with subsequent modifications for tuning of the film, was monitored through cyclic voltammetry (CV), while the compositions of the films were analyzed using X-ray photoelectron spectroscopy (XPS). The uptake of analyte NPs was investigated using linear sweep voltammetry (LSV). Scanning electron microscopy (SEM) was employed to characterize the NAIM system at different stages of preparation. Topography imaging and thickness determination of various films were acquired using atomic force microscopy (AFM). The synthesized NPs were characterized using transmission electron microscopy (TEM).

The thesis commences by introducing the underlying concept (Chapter 1) upon which the work has been developed. Chapter 2 provides an overview of current NAIM systems and highlights key findings and conclusions. Chapter 3 outlines the high-resolution techniques utilized in the study, while Chapter 4 provides a summary of the experimental details. Chapters 5 covers the study of developed plumbagin-based

NAIM system and explore further investigations into their efficacy in the uptake of analyte NPs. Chapter 6 outlines the utilization of PS NPs as template NPs along with the associated challenges. Chapter 7 explores aryldiazonium-based NAIM systems and their effectiveness in selectively recognizing analyte NPs.

# 2    Nanoparticle-Imprinted Matrices

Nanoparticle-imprinted matrices (NAIM) are innovative materials designed for the precise recognition and capture of NPs based on their unique size, shape, and surface properties. NAIMs hold promise for various applications, particularly in the field of nanoparticle detection and sensing, offering a tailored approach for the effective and specific interaction with NPs of interest. This chapter delves into the established NAIM systems and highlights the key insights obtained from the research.

## 2.1    Realized NAIM Concepts

NAIMs share the concept of MIPs[44–47,50–52] of creating selective recognition materials. Both MIPs and NAIMs involve the use of a template to create specific binding sites within a polymer matrix. MIPs are designed to imitate the binding sites of a particular molecule, allowing them to selectively capture that molecule upon recognition. This is typically employed in chemical sensors and separation techniques.[53,54] NAIMs are tailored for the detection and capture of NPs, focusing on attributes like size, shape, and surface charge.[38,40,41,48] However, there are also important conceptual differences between NAIMs and MIPs: Molecular analytes can reach binding sites in three-dimensional MIP materials through a pore network that is created during the formation process. NPs are much larger than molecular analytes and therefore, binding sites for NP must be located at the surface of NAIMs. This difference has implications for the suitable detection techniques for the material uptake in MIPs and NAIMs.

The formation of hollow spheres by removing incorporated gold NPs (Au NPs) from the polymer matrix has been previously investigated.[55–57] In these instances, the polymer matrix was created either by polymerizing the ligand shell around the Au NPs or through reactions with other functional reagents. The primary drawbacks included the generation of materials that were insoluble and challenging to characterize.[58] Addressing these challenges, Koenig et al.[58] developed bulk nanoparticle-imprinted polymers, marking the first instance of their use in selectively recognizing Au NPs. The acrylate terminated Au NPs were copolymerized with bulk monomers, leading to the formation of nanoparticle-imprinted polymers. Subsequently, the Au NPs were removed from the system to yield nanoparticle-imprinted polymers. Significant

amounts of crosslinking agents and porogen ( a material additive that remains non-reactive with the monomer but is employed to induce pores in the resultant polymer.) were added to achieve rigid and porous nanoparticle-imprinted polymer.[58] Due to the challenges posed by intricate synthesis, limited versatility, difficulty in template removal, and non-uniformity, new approaches were devised for the development of NAIMs.

Size-selective recognition of NAIMs were first reported by Kraus-Ophir et al.[38] They effectively employed the Langmuir-Blodgett (LB) technique to transfer one to three layers of polyaniline films of thickness varying from 1 to 3 nm, along with citrate-stabilized gold NPs (Au-Cit NPs) measuring 15 nm and 33 nm in diameter, onto an indium-doped tin oxide (ITO) substrate. The removal of the Au-Cit NPs from the system via the electrooxidation of Au led to the creation of cavities within the structure. These cavities were then examined to assess their capacity for selective uptake of analyte NPs, revealing their effectiveness in recognizing NPs based on size. This study is the first to emphasize the significance of matrix thickness in achieving selective nanoparticle recognition.

Bruchier-Spaniel et al.[48] utilized the Langmuir-Blodgett (LB) method to investigate the uptake ability of a NAIM system. The matrix was developed by transferring 4 nm AuNPs stabilized with 1-dodecanethiol and cellulose acetate at the air-water interface onto an ITO surface. The thickness of the film was adjusted by depositing between one and five monolayers. The electrochemical dissolution of the Au NPs led to the creation of the cavities, which was subsequently employed to assess the uptake capability. The findings revealed a substantial enhancement in the recognition capacity of Au NPs, particularly beyond two cellulose acetate LB layers, creating deeper nanocavities that improved selectivity and supramolecular interactions. The system exhibited remarkable specificity, displaying a strong preference for Au NPs with the same alkanethiol capping agent as the originally imprinted Au NPs. A significant limitation of LB method is the coverage of matrix over the Au NPs, which leads to their incomplete removal from the NAIM system and limited control over the distribution of template Au NPs.

Hitrik et al.[39] established a NAIM system through a layer-by-layer approach. The substrate surface was initially coated with a positively charged polyethyleneimine (PEI) layer, serving to adhere the negatively charged Au NPs. Subsequently, the matrix

was constructed through the layer-by-layer adsorption of oleic acid (OA) and polyacrylic acid (PAA). The cavities formed following the electrooxidation of Au NPs were examined for their capacity to capture analyte NPs of different core materials, specifically, Au and Ag NPs. These cavities effectively recognized Au and Ag NPs with comparable sizes to those of the template Au NPs. This demonstrates that despite differences in core material of template and analyte NPs, NPs of similar sizes and shells can be recognized.

Witt et al.[41] successfully employed electrochemical deposition to achieve matrix of controlled thickness in their NAIM system. Following the adsorption of 40 nm Au NPs on 3-(aminopropyl)triethoxysilane (APTES)-functionalized ITO, a self-limiting polyphenol film with a specific thickness was electrodeposited as the matrix. The cavities created after the removal of Au NPs via electrodissolution were evaluated for their capacity to capture 20 nm Ag NPs and 50 nm Au NPs with similar ligand shells. The size selectivity of the cavities imprinted by 40 nm Au NPs was evident through the notably high uptake of 20 nm Ag NPs over 50 nm Au NPs.

A study conducted by Bruchiel-Spaniel et al.[42] aimed to examine in detail how the properties and thickness of the matrix influence the recognition capabilities of the NAIM system. The matrix was formed through the electrografting of *p*-aryldiazonium salts, each carrying distinct functional groups. Specifically, the matrix created from 4-(hexyloxy)phenyldiazonium tetrafluoroborate was compared to the matrix developed from 4-(carboxy n-hexyl ester)phenyldiazonium tetrafluoroborate to assess the recognition capabilities of the NAIM system for analyte Au NPs. The latter demonstrated the highest uptake due to the supramolecular interactions occurring between the cavities and Au NPs. The uptake potential of a *p*-aryldiazonium-based matrix was highly influenced by the functional groups present at the *p*-position. When examining the impact of film thickness on uptake capacity, it has become apparent that achieving an optimal thickness in relation to the size of the template and analyte NPs is crucial for efficient uptake. Figure 2 illustrates a schematic depicting the impact of thickness of the matrix on the selectivity of NAIM. Excessively thick matrices may result in incomplete template NP removal or the formation of poorly defined cavities. Conversely, if the matrix layer is too thin, distinguishing specific from nonspecific uptake becomes increasingly challenging, affecting both binding strength and potential detection methods.
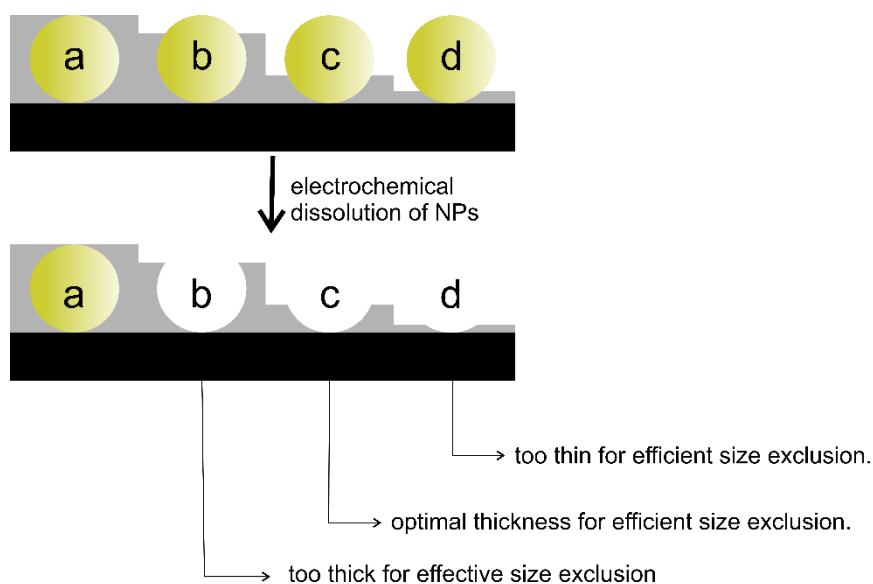
Figure 2. Schematics to show the optimal matrix thickness: a) matrix has grown over the NPs, hindering their complete dissolution., b) matrix thickness surpasses the radius of the NPs, resulting in the formation of cavities lacking size exclusion properties, c) matrix thickness within the range of the radius of the template NPs, potentially demonstrating effective size exclusion and d) matrix lacks the thickness required to demonstrate size exclusion properties.

A similar study has revealed that even subtle modifications to the stabilizing shell enveloping Au NPs profoundly impact the recognition ability of the NAIM system. Zelikovich et al.[40] illustrated this using Au NPs stabilized by various carboxylic acid-bearing thiols. In this research, three unique NAIM systems were established through the imprinting of Au NPs, each with distinct carboxylic acid-bearing thiols for stabilization. The matrix was developed via electrografting from 4-carboxyphenyldiazonium salts. Upon examining these systems for their recognition abilities with three different analyte Au NPs, it became evident that the matrix exhibited remarkable selectivity toward the originally imprinted Au NPs. A similar study was conducted with Au NP stabilized by different isomers of mercaptobenzoic acid.[59] The uptake was studied in detail using Raman Spectroscopy and electrochemistry, where matrix exhibited high selectivity towards the originally imprinted Au NPs.

NAIM systems have demonstrated the ability to selectively recognize NPs based on their size, even when the core materials differ. This size selectivity is a critical feature of NAIMs, enabling the discrimination of NPs with similar sizes but distinct core

materials. The thickness of the matrix is a critical factor in achieving effective nanoparticle recognition. An optimal matrix thickness relative to the size of both template and analyte NPs is necessary for efficient uptake. The chemical nature of the matrix plays a significant role in the selectivity of NAIM systems. The presence of functional groups and modifications in the stabilizing shell around NPs can have a substantial impact on recognition.

One of the primary challenges in NAIM development is the incomplete removal of template NPs from the matrix. When the analyte and template NPs share the same material composition, there exists a risk that incompletely removed template NPs might be erroneously counted as analyte NPs during the detection phase. The problem is addressed in the thesis through the utilization of analyte and template NPs featuring different core materials (Chapter 5 – 7). Specifically, the template NPs are insulating in nature, serving to prevent excessive film overgrowth during the electrodeposition process. The post modification of the matrix properties specifically for analyte NPs had not been pursued previously, despite the use of various matrices with different functional groups. This thesis investigated the adaptability in tuning matrix properties by introducing diverse functional groups and adjusting the pH (Chapter 5).

# 3 Applied Characterization Techniques for NAIM Systems

This chapter explores the employed high-resolution methodologies for the characterization of NAIM systems. This includes standard techniques such as cyclic voltammetry (CV) and linear sweep voltammetry (LSV) utilized in the development and study of NAIM. The utilization of optical imaging methods is impractical due to their limited resolution. Surface-sensitive techniques such as scanning electron microscopy (SEM), transmission electron microscopy (TEM), atomic force microscopy (AFM) and X-ray photoelectron spectroscopy (XPS) were utilized for a detailed examination of the system.

## 3.1 Cyclic Voltammetry

Cyclic voltammetry (CV) is an electrochemical technique employed for in-depth investigations into the electrochemical behavior of chemical species, particularly regarding their redox properties and reaction kinetics. The most basic electrochemical cell comprises an electrolyte-filled glass beaker containing a working electrode, auxiliary electrode, and reference electrode immersed in the electrolyte solution. In CV, the voltage is swept between two values ($E_1$ to $E_2$) at a fixed scan rate, $v$ (Figure 3b), however once the voltage reaches $E_2$, the scanning direction is reversed, and the voltage is swept back to $E_1$. When the potential is applied between the working and reference electrode, the current flows between the working and auxiliary electrode. This current is plotted against the applied potential.[60,61] Figure 3c shows a typical cyclic voltammogram of 1 mM ferrocene methanol in 0.1 M tetrabutylammonium hexafluorophosphate/acetonitrile (TBAPF$_6$/ACN) at 0.1 V s$^{-1}$. When the potential is swept exclusively from $E_1$ to $E_2$ (as illustrated in Figure 3a), this technique is referred to as linear sweep voltammetry (LSV).[61]

In the thesis, the blocking property of electrodeposited films were investigated with the help of a reversible redox couple. The formal potential ($E^{o\prime}$) for a reversible electrochemical reaction is the mean value of anodic ($E_{pa}$) and cathodic potentials ($E_{pc}$):

$$E^{o\prime} = \frac{E_{pa} + E_{pc}}{2}$$
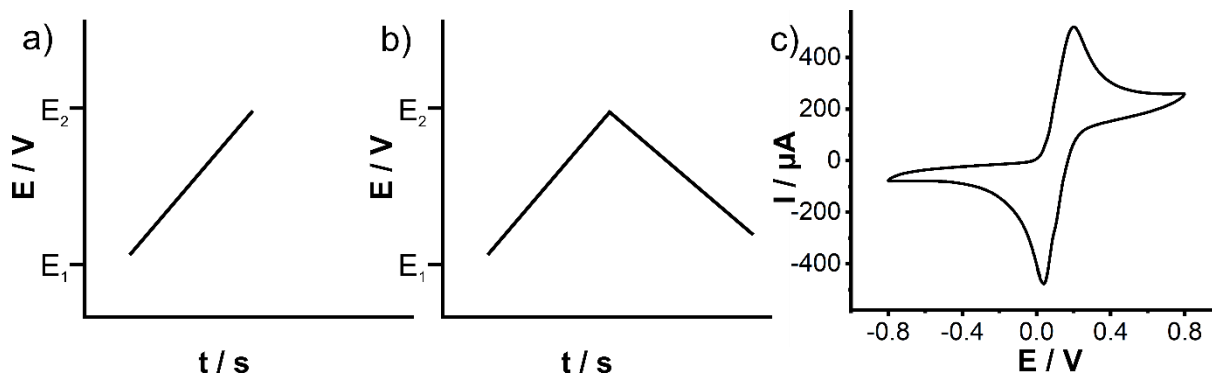
Figure 3: Potential waveform for a) linear sweep voltammetry and b) cyclic voltammetry and c) cyclic voltammogram of 1 mM FcMeOH + 0.1 M TBAPF6/ACN at 0.1 Vs$^{-1}$.

The separation between anodic and cathodic peak potentials of diffusing redox couple is calculated using the following equation:

$$\Delta E_{\mathrm{p}} = E_{\mathrm{pa}} - E_{\mathrm{pc}} = 2.218\frac{RT}{nF}$$

Peak current ($I_{\mathrm{p}}$) is proportional to the square root of scan rate $v^{1/2}$ for electrochemically reversible electron transfer process, described by the Randles-Sevcik equation:

$$I_{\mathrm{p}} = 0.4463nFcA\left(\frac{nFvD}{RT}\right)^{1/2}$$

where $R$ is the gas constant ($R$ = 8.314 J·mol$^{-1}$·K$^{-1}$), $T$ is the temperature (K), $n$ is the number of electrons involved in the Faradaic reaction, $F$ is the Faraday constant ($F$ = 96 485A s mol$^{-1}$) $c$ is the bulk concentration (mol cm$^{-3}$), $A$ is the electrode surface area (cm$^2$), $v$ is the scan rate (V s$^{-1}$), $D$ is the diffusion coefficient (cm$^2$ s$^{-1}$) and $I_{\mathrm{p}}$ is the peak current (A)[61].

In this study, chemically modified electrodes were prepared using cyclic voltammetry. These electrodes can be prepared using different techniques, such as irreversible adsorption or covalent attachment.[61] The adsorption of species onto the electrode surface alters the electrochemical characteristics of the electrode. Cyclic voltammetry was used in this study to monitor the electrodes during different stages of modification.

During the study, blocking polymers were electrochemically deposited from phenol, dopamine, or p-phenylenediamine. These blocking polymers were generated from the respective monomers, resulting in the deposition of impermeable layers that

11

effectively passivated the surface of the electrode. The growth of the non-conducting polymer film is self-limiting process resulting in thin films. The mechanism where the monomer undergoes oxidation or reduction on the working electrode, leading to the formation of a radical. The electrochemical polymerization method can be categorized into anodic or cathodic electrochemical polymerization. The process of polymer formation and growth is thought to occur through either the coupling of radicals or the reaction between a radical and a neutral monomer. Radicals can react with nearby radicals or neutral monomers, resulting in the production of the polymer.

Another method used for the development of the modified electrodes was covalent attachment. Stronger attachment to the substrate surface can be achieved through the covalent attachment of the desired component to surface groups that are either already present on the substrate or on the substrate itself. The matrices developed from aryl diazonium salts followed the latter mechanism as well as the electrografting of plumbagin monolayer followed the initial mechanism of electrografting.

The current response of electrode adsorbed species can be elucidated by the following expression,

$$I_{\mathrm{p}} = \frac{n^2 F^2}{4RT} v A \Gamma^*$$

where $\Gamma^*$ is the surface coverage of the adsorbed species in mol cm$^{-2}$. Here, the current $I_{\mathrm{p}}$ varies linearly with the scan rate, $v$, contrary to the linear dependence of current and $v^{1/2}$.


## Electrochemical Detection of Nanoparticles

Nanoparticles, if redox active can be detected through the simplest method of stripping voltammetry. It is a method where the NPs immobilized on the electrode surface are oxidized or reduced through electrochemical methods like LSV, CV or pulse voltammetry analysis.

In the thesis, LSV was employed to electrochemically detect and quantify the analyte NPs. In LSV the resulting current, $i$, is measured during the application of each potential step. Subsequently, a plot is generated by measuring the current against the applied potential. The charge required to remove the specifically adsorbed NPs can be calculated from the integrated charge, $Q_{total}$, obtained from the area under the

electrodissolution peak (explained in Chapter 5). The charge required to remove one Au NP can be calculated using,

$$Q = N.n.F$$

where $Q$ is the charge, N is the no. of atoms in one Au NP, $n$ is the number of electrons involved in the reaction and $F$ is the Faraday constant. The quantity of electrochemically dissolved NPs can be determined by utilizing $Q_{total}$ and the amount of charge ($Q$) needed to remove a gold NP.

The electrodissolution of Au exhibits distinct behaviors depending on whether it occurs in the presence of a ligand or in ligand-free electrolytes.[62] In chloride solutions, gold undergoes anodic dissolution, leading to the formation of a soluble tetrachloro-gold complex as shown in the following reaction,

$$Au + 4\ Cl^- = [AuCl_4]^- + 3\ e^-$$

In an aqueous electrolyte without ligands, gold exhibits relative stability, remaining inert up to high anodic potentials. The standard electrode potential for gold dissolution in the presence of chloride ions is 1.002 V vs SHE, and this value increases to 1.45 V vs SHE in the absence of complexing ligands.[63] With the presence of chloride ions, the dissolution rate is improved and shows a substantial rise in current with increasing concentration of chloride ions.[62]

## 3.2 Atomic Force Microscopy

Atomic force microscopy (AFM) is a scanning probe microscopy (SPM) invented by Binning et al. in 1986,[64] following the invention of scanning tunnelling microscopy (STM)[65]. STM is based on the principle of quantum tunnelling and can study conductive surfaces with atomic resolution.[65,66] In STM, a sharp metallic tip is positioned close to the surface of the sample. A drawback of STM compared to AFM is that it is less suitable for insulating or non-conductive samples.[66] This tip is usually made of a conductive material and is brought within nanometers of the sample surface, where a distance-dependent tunnelling current between tip and sample is recorded.[65] The invention of AFM made it possible to study non-conductive surfaces at a level comparable to STM. AFM operates by measuring tiny forces between a sharp tip and

a sample surface, enabling high-resolution imaging of nanoscale features.[64,67] The versatility of AFM and the ability to operate under environmental conditions make it a valuable tool in fields like nanoscience, biology and beyond.


### 3.2.1 Operation Principle and Probe Requirements

AFM operates on the concept of a cantilever-mounted tip interacting with the sample. The cantilever is equipped with a sharp tip at its free end. The schematics of AFM with scanning cantilever tip and beam deflection detection system is shown in Figure 4 Using a feedback control system, the tip scans across the surface in a raster pattern while maintaining a constant force or tip-sample distance at a set value. As the AFM tip scans across the sample surface, it encounters variations in height and surface features on the sample surface. These variations cause the cantilever to deflect. The deflection is measured by a laser beam that is reflected from the back side of the cantilever onto a divided photodiode. When the laser beam changes the position on the photodiode, the voltage output of the segments change. Using calibrations, the voltage difference between the photodiodes can be used into the position of the laser on the photodiode and thus the deflection of the cantilever. The divided photodiode is often divided into four segments labeled A, B, C, and D. These segments allow for the simultaneous and independent measurement of the cantilever vertical and lateral deflection. The vertical deflection information from the photodetector is used as a height feedback signal.[67–69] This signal is proportional to the topography of the sample. It provides information about how far the scanner must move vertically to maintain a pre-set setpoint, ensuring that the tip-sample distance remains constant during scanning.

As an AFM tip nears a sample surface, a range of forces becomes active, influencing the deflection of the cantilever. The primary forces influencing the cantilever deflection are the long-range attractive forces (van der Waals) and the short-range repulsive forces (electrostatic).[69,70] These forces are induced by fluctuating dipole moments between atoms of the tip and the sample. They can be approximated using the Lennard-Jones potential as a function of the probe-sample distance and are associated with the operational modes of SFM.[69] AFM offers various operational modes, where the three basic modes are contact mode, tapping or intermittent contact mode, or non-contact mode.[67] In contact mode, the tip is in permanent physical

contact with the sample surface, and the operations are confined to high force gradient regions within the repulsive force range. The schematic illustration of the Lennard-Jones potential is shown in Figure 5. Tapping mode AFM operates with intermittent contact between the tip and the sample surface, where the cantilever oscillates between the attractive and the repulsive regime of the curve. The non-contact mode is limited to the attractive regime of the curve.
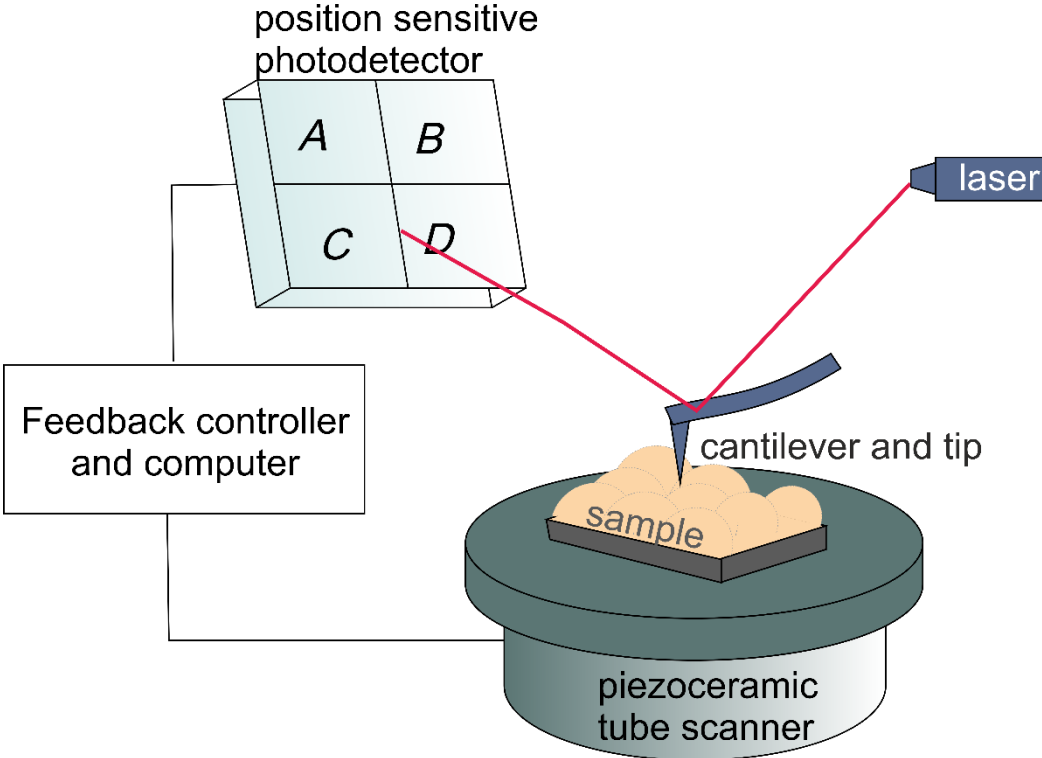


Figure 4: Schematic drawing of atomic force microscope with scanning cantilever tip and beam deflection detection system.
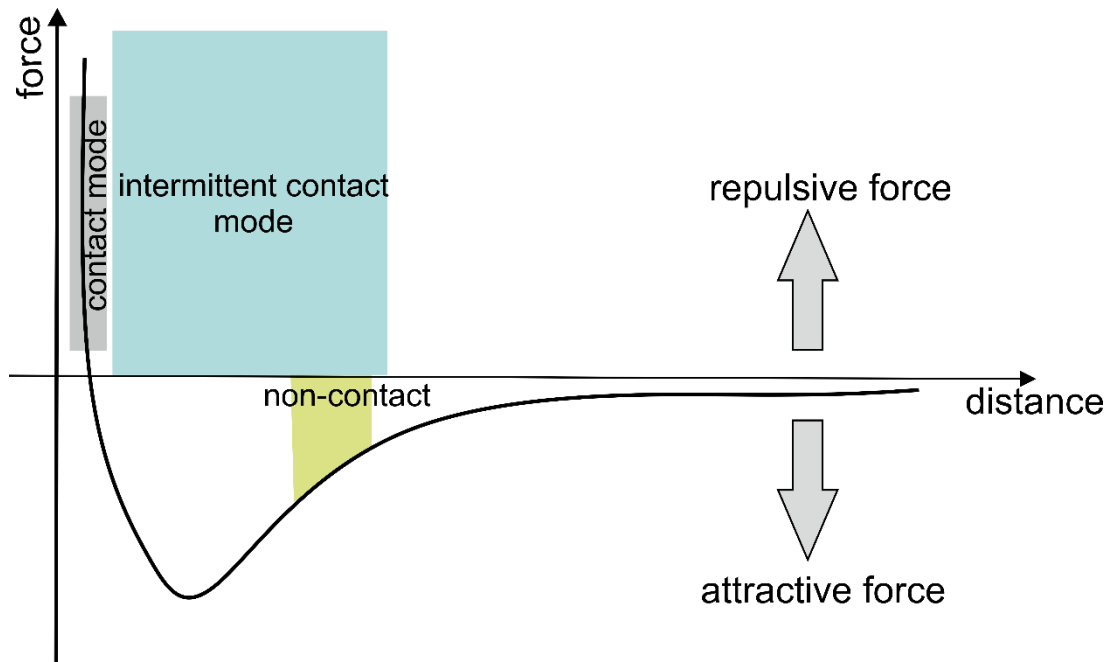
Figure 5: Schematic illustration of the Lennard-Jones potential showing the interatomic forces between the tip and the sample in dependence on their distance.

Choosing the right AFM probe depends on the specific experiment or measurement objectives, the type of sample being investigated, and the imaging or measurement mode, whether it involves topography, mechanical properties, electrical properties, or other surface interactions. AFM tips or cantilevers are available in different types and materials, each developed to suit different applications. These tips can have different shapes, including sharp, cone-shaped, or spherical. Commercially available. AFM tips are typically made of materials like silicon, silicon nitride, silicon carbide, and diamond. The choice of material depends on factors like stiffness, wear resistance, and chemical reactivity, making certain materials more suitable for specific applications.[67,71] These tips come with different spring constants, which determine their stiffness. Stiffer cantilevers with high spring constants were employed for topography studies. These cantilevers, being sufficiently rigid, prevent the oscillating tip from being drawn into the sample. Soft cantilevers were utilized to study the thickness of samples, as they are particularly well-suited for the study of soft and fragile samples in contact mode. Table 1 presents the technical specifications of the cantilevers employed in this thesis. Some AFM probes have special coatings, such as doped diamond or platinum-iridium, which can enhance their electrical conductivity and suitable for conducting samples.

Table 1. Specifications of the cantilevers used in the thesis.

| Cantilever specifications | Contact mode | | Intermittent contact mode |
|---|---|---|---|
| | MSCT | FESPA-V2 | NCHV-A |
| geometry | Triangular | rectangular | rectangular |
| coating | reflective gold | reflective gold | reflective aluminium |
| resonant frequency (kHz) | 90-160 | 50-100 | 270-400 |
| spring constant (N/m) | 0.6 | 2.8 | 20-75 |
| **Tip specifications** | | | |
| radius (nm) | 10-40 | 8-12 | 8 |

### 3.2.2 Operation Modes

**Contact-Mode.** In contact mode AFM,[69] the AFM tip is in physical contact with the sample during scanning. In contact mode, there are two imaging modes: constant force and constant height. In constant height mode, the AFM tip scans the surface of the sample at a fixed, predetermined $z$-height above the surface, as shown in the Figure 6. The topographical information is obtained by measuring the deflection of the cantilever in the $z$-direction as the AFM tip scans across the sample. In constant force mode, the force between the AFM tip and the sample is kept constant during scanning. A feedback loop continually monitors the deflection of the cantilever, which is sensitive to variations in the force between the tip and the sample. If the deflection deviates from the preset value due to sample topography or interactions, the feedback mechanism adjusts the height of the tip to maintain the deflection and thus a constant force.



contact mode          intermittent contact mode
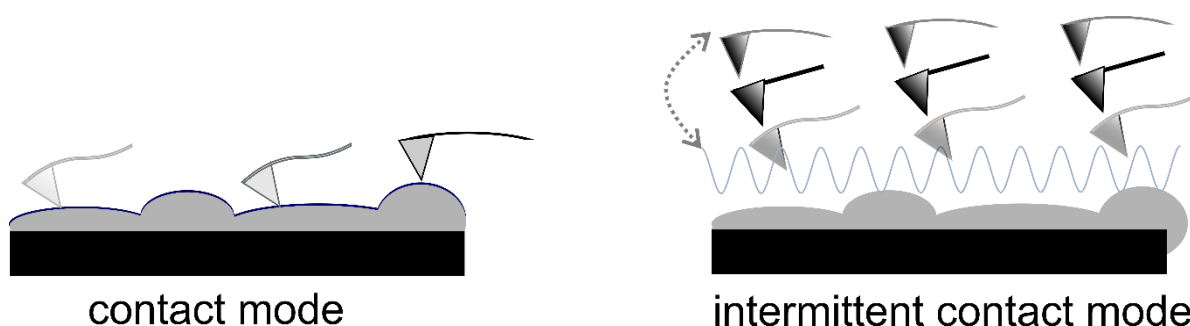
Figure 6: Scheme illustrates contact mode and intermittent contact mode.

Constant force mode is ideal for precise force measurements and high-resolution imaging but can be more aggressive on the sample. The constant force mode operates at a slower scanning speed than the constant height mode, as the feedback loop continually adjusts the tip height. When the AFM tip is scanning across the surface of a sample in contact mode, lateral forces arise between the tip and the

sample. The lateral force applies torque to the cantilever, resulting in either bending or twisting of the cantilever depending on their relative orientation. When significant, this deflection can be misinterpreted as topographical features. The AFM artefacts observed while scanning samples in contact mode and intermittent contact mode are provided in Figure 7. The presence of strangely shaped features and image distortions while imaging a 3-aminopyridine (3-AP) modified ITO in contact mode (Figure 7a) and ITO modified using a binary layer electrografted from 4-nitrobenzene diazonium salt and 4-((triisopropylsilyl) ethynyl) benzene diazonium salt (NB/TIPS) in intermittent contact mode (Figure 7b) can be observed. This can be avoided by varying the feedback parameters, tip or scanning modes.

Constant height mode is faster compared to constant force mode because it doesn't require continuous force adjustments during scanning. In this mode, the tip applies lower forces on the sample surface, reducing the risk of both tip wear and sample damage. This is particularly important when working with soft or fragile samples. However, constant height mode may encounter difficulties in obtaining precise images of highly rough surfaces, potentially leading to the disengagement of the tip or due to sample-tip collision. This can result in incomplete or distorted images as the tip cannot follow the intricate details of the surface. When dealing with rough surfaces that have significant height variations, constant force mode can adapt to these variations by adjusting the tip height to maintain the preset force. This adaptation ensures that the tip remains in contact with the surface, even on rough surfaces.
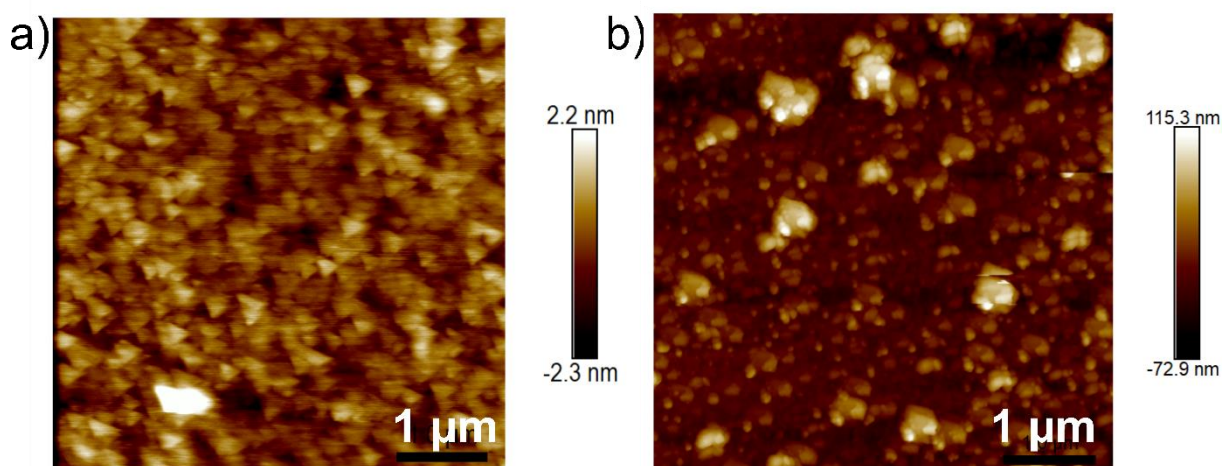


Figure 7. AFM images with artefacts obtained in a) contact mode of 3-aminopyridine modified ITO surface and b) intermittent contact mode of NB/TIPS modified ITO.

**Intermittent Contact Mode.** The intermittent contact mode (often called tapping mode) is an imaging mode in AFM that offers advantages for imaging and characterizing a wide range of samples. The AFM tip oscillates at or near its resonance frequency with an amplitude of up to 100 nm while scanning and touches the sample intermittently, as shown in the Figure 6. This causes a significant reduction in the tip amplitude. The reduction in the oscillation amplitude is utilized for the identification and quantification of topographical features. The feedback system regulates the distance between the cantilever and the sample by maintaining the amplitude as close as possible to the pre-defined amplitude setpoint. This method, which greatly reduces lateral tip-sample forces, generally results in higher resolution when compared to the conventional contact mode AFM, where the tip and sample are in permanent mechanical contact.[72] Figure 8 provides a comparison between the images obtained in contact mode and intermittent contact mode. On comparison to the intermittent contact mode image in Figure 8b, the resolution is low in the contact mode image in Figure 8a. Also, the streaks are only observed in the image obtained from contact mode. These streaks can be due to the instable tip-sample interactions in contact mode.
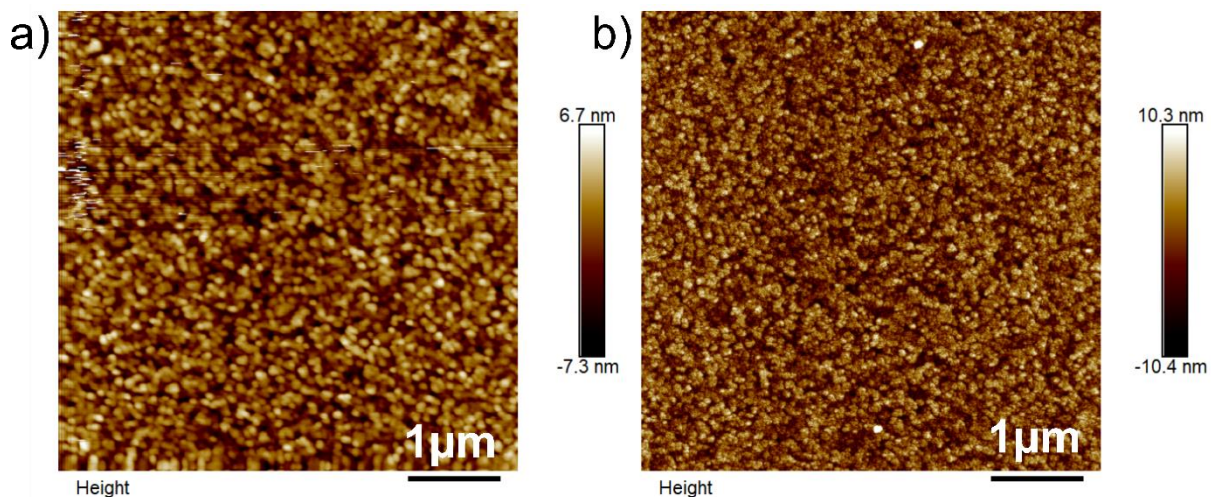


Figure 8. TIPS film modified ITO surface imaged in a) contact mode and b) intermittent contact mode.

Phase imaging[73] is used to gather additional information about the surface properties of the sample beyond topography and can be simultaneously obtained with topographic imaging in intermittent contact mode. Unlike amplitude-based imaging, phase imaging uses the phase shift in the cantilever oscillation relative to the signal sent to the piezodrive[74] due to variations in material properties like adhesion, sample hardness, or elasticity. The phase shift data are used to create phase contrast images.

Areas with different material properties or tip-sample interactions result in distinct phase shifts, which are represented as variations in contrast in the phase image. Phase imaging can be employed to examine surface alterations, providing enhanced contrast between distinct surfaces. It can be used to distinguish between different phases in polymer blends,[75] for characterizing the surface morphology of nanostructured materials, topography and properties of biological cells[76] etc. Figure 9 displays both the topography and phase images of a dense 3-aminopyridine matrix after removing template PS NPs recorded in the intermittent contact mode. In contrast to the topography image in Figure 9a, phase image in Figure 9b reveals cavities with improved contrast, where the structure of the cavities is more clear. The irregular growth of the 3-aminopyridine film can be easily identified from the phase image in Figure 9b, where in the topography image (Figure 9a) it appears as black region which could be misinterpreted as cracks.
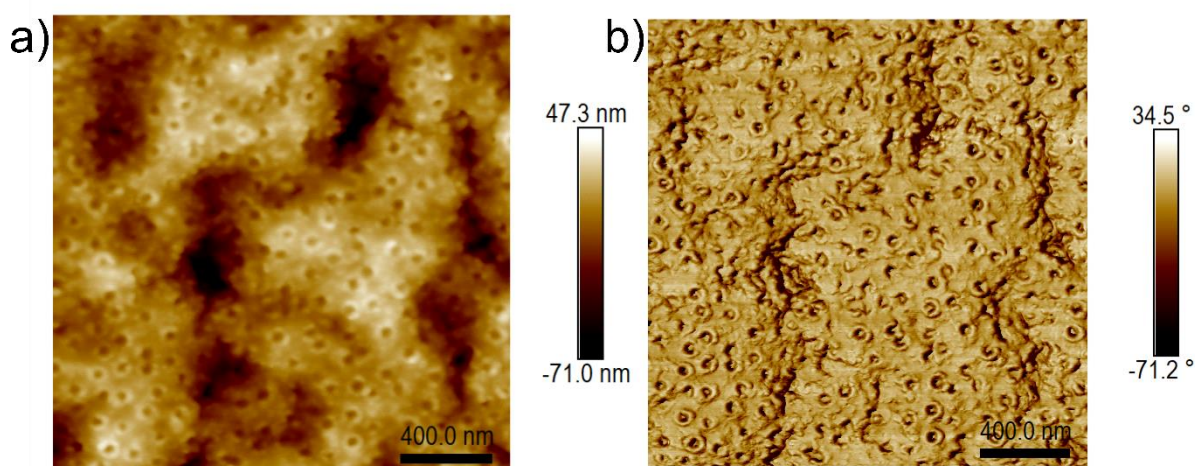


Figure 9. AFM a) topography image and b) phase image of a dense 3-aminopyridine matrix deposited on ITO surface after the removal of template PS NPs.

Non-contact mode operates on a principle similar to intermittent contact mode. It is distinguished by subtle probe oscillations, typically with a 1 nm amplitude, while the tip is positioned 50-100 Å above the surface. This mode functions within the attractive region of the intermolecular force curve. As the distance between the probe and the sample increases, the resolution of the non-contact mode diminishes due to the influence of long-range forces at greater distances.[67]

## 3.3 X-Ray Photoelectron Spectroscopy

### 3.3.1 Working Principle

X-ray photoelectron spectroscopy (XPS), also known as electron spectroscopy for chemical analysis (ESCA), is a surface-sensitive analytical technique used to investigate the elemental composition, chemical bonding, and electronic state of a wide range of surfaces. XPS is based on the photoelectric effect, first elucidated by Albert Einstein in 1905. It describes the ejection of electrons from a material surface when exposed to photons[68,77]

When high energy monochromatic X-rays strike the sample, they cause the emission of electrons from the inner atomic orbitals of atoms in the material as shown in Figure 10a. The energy of the X-rays is carefully controlled as this energy is critical because it must exceed the binding energy of the electrons in the outermost atomic shell of the sample. The core level electrons of the atoms are tightly bound, and their binding energies and atomic energy level are specific to each element. Following this, the atom, having assumed an (n − 1) electron configuration, undergoes reorganization by transferring an electron from a higher energy level to occupy the formerly vacant core hole under emission of X-rays (X-ray fluorescence) (Figure 10b). Alternatively, the vacancy in Figure 10a can be filled by an electron from an outer shrll under the emission of a second electron called Auger electron (Auger electon emisision). The ejected electrons are collected by an electron energy analyzer. The emitted photoelectron arises from the complete transfer of energy from the incident X-ray photon to a core-level electron. From the kinetic energy ($E_{kin}$) of the emitted photoelectron, binding energy ($E_B$) is determined.

According to Einstein equation, the energy of the incident X-ray ($hv$) is the sum of kinetic energy and binding energy. This could be rearranged to obtain the $E_B$, where Φis the work function of the spectrometer.

$$E_B = \ hv - E_{kin} - \Phi$$
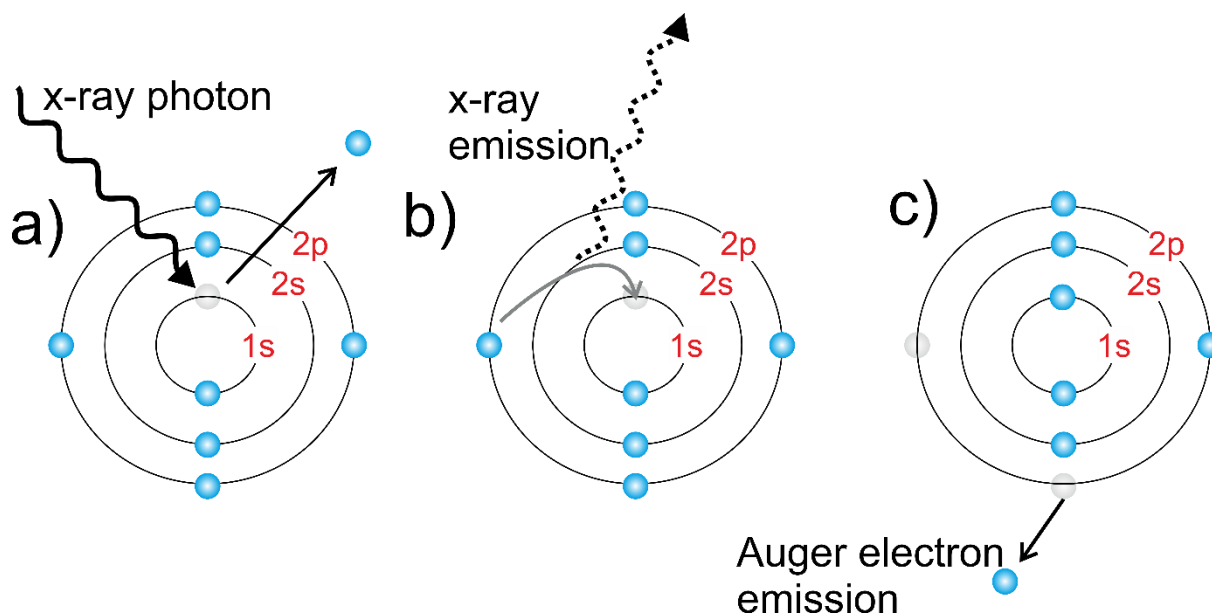
Figure 10. (a) The X-ray photon imparts its energy to a core-level electron, resulting in the emission of a photoelectron from the initial n-electron state, (b) Subsequently, the atom, now in an (n − 1)-electron configuration, may undergo a reorganization by transitioning an electron from a higher energy level to fill the previously vacant core hole, (c) In this rearrangement, as the electron described in (b) drops to a lower energy level, the atom can dissipate excess energy by expelling an electron from a higher energy level. This expelled electron is commonly referred to as an Auger electron. Alternatively, the atom can release excess energy by emitting an X-ray photon, a phenomenon known as X-ray fluorescence.

In the case of conducting samples, the energies of the photoelectron peaks can be calibrated with respect to the Fermi level of the spectrometer, and they remain unaffected by the work function of the sample. In situations where sample surfaces are not in electrical contact with the spectrometer or insulating samples, require an additional source to compensate the charge accumulated when exposed to X-rays. Therefore, charge compensation methods are employed to mitigate these effects. During charge compensation, the sample is flooded with a monochromatic low energy source (< 20 eV). In this case, the vacuum level of the sample will be in electrical equilibrium with the energy of the compensating electrons.

## Thickness studies of thin films using XPS

XPS can be utilized to analyse the thickness of the films ranging from 1 – 10 nm, which is the information depth of XPS.[78] The thickness of the films can be analyzed from the

intensity ratio of photoelectron peaks from the film modified substrate and the bare substrate using the following equation,

$$\ln \frac{I}{I_o} = \left( \frac{-d}{\lambda} \right) \sin \theta$$

where $I$ and $I_o$ are the peak intensities from modified layer and the bare substrate, $d$ is the thickness of the modified layer, $\lambda$ is the photoelectron escape depth and $\theta$ is the takeoff angle.[79]

The thickness of the homogeneous NB/TIPS film electrografted on ITO was measured using XPS. For this, In 3d peaks from bare ITO was initially recorded. Under the same experimental conditions, the In 3d peak arising from the underlying substrate after the deposition of the film was also measured. Photoelectrons leaving the substrate are scattered as it travels through the film. The scattering scales linearly with the distance these electrons must travel to escape the surface. Figure 11 shows the In 3d spectra obtained from bare ITO and ITO after modification with NB/TIPS.
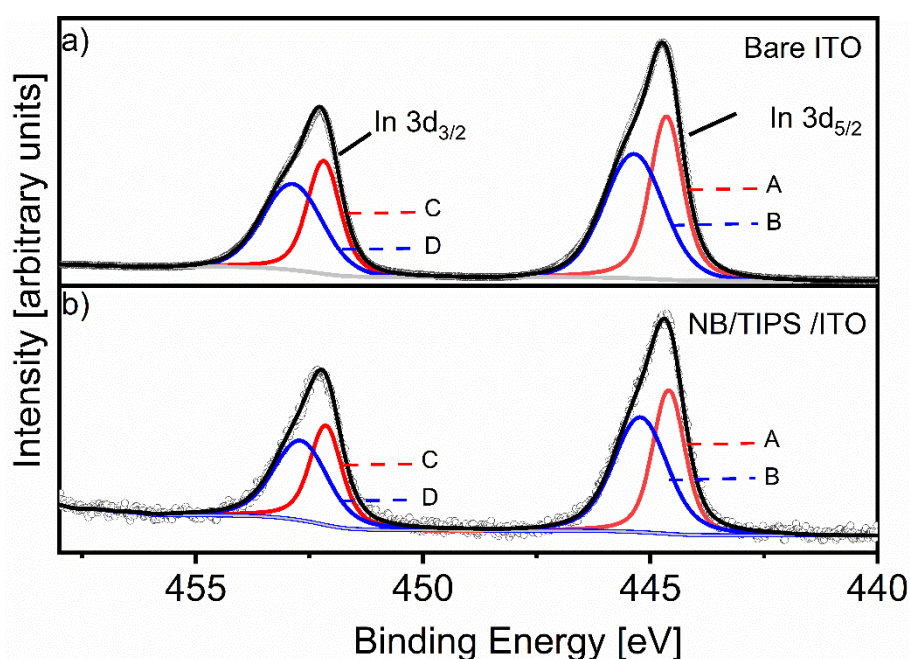


Figure 11. In 3d spectra of a) bare ITO and b) ITO after electrografting NB/TIPS film on ITO.

The In 3d spectrum can be interpreted as a set of two doublets, where the In $3d_{5/2}$ peak at $E_B$ 444.7 eV can be assigned to $In_2O_3$ and at 445.4 eV can be assigned

to surface In-OH species.[80] The intensities of these peaks originating from different samples are provided in the Table 2.

Table 2. The intensity of In 3d peaks obtained after peak fitting from bare ITO ($I_o$)and NB/TIPS/ITO ($I$).

| Peaks | Bare ITO ($I_o$) | NB/TIPS/ITO ($I$) |
|---|---|---|
| A | 72202.79 | 2960.00 |
| B | 54999.96 | 2368.72 |
| C | 49978.31 | 2048.89 |
| D | 38070.54 | 1639.61 |

These intensities are substituted for the ratio of In 3d peak intensities ($I/I_o$) in the above equation, $\lambda$ is estimated to be 3.5 nm[81] and the takeoff angle used in the experiment is 90°. From this, the thickness of the NB/TIPS film is calculated to be 11.1 nm, which is comparable to the thickness estimated from the AFM scratching method, given in Appendix B2c.

### 3.3.2  Peak Fitting

Peak fitting in XPS is important for extracting detailed chemical and electronic information from XPS spectra. It allows to quantitatively analyze surface composition, identify chemical states, detect contaminants, and gain insights into the electronic structure of materials. Generally, the interval between spectral components closely matches the observed peak widths, which is around 1 eV. As a result, in experimental spectra, it is common that spectral components overlap. To discern the necessary peak parameters, one must employ a peak-fitting procedure.

Mathematical functions for peak shapes (such as Gaussian, Lorentzian, asymmetric, or mixtures) are used to model each spectral component. These functions are adjusted to best fit the experimental data. The fitting process involves finding the parameters that minimize the difference between the modelled peaks and the actual data. The parameters typically include peak position, peak width which is related to chemical state and peak intensity which is related to element concentration. In addition to peak fitting, a background subtraction step is often performed to remove the peak contributions from the background. The prevalent approach for modelling the background was pioneered by Shirley. Once the background has been established, initial estimates for each peak parameter, derived from reasonable values from prior

experiments, are introduced. Subsequently, a least-squares fitting algorithm is employed to iteratively converge toward the final parameter values. Detailed discussions on these peak-fit quantities can be found in a series of publications. [82–85]

For assessing the quality of a peak fit in XPS or similar spectroscopic techniques, parameters such as chi-squared ($\chi^2$), peak position, peak width, peak intensity, residuals etc., are relevant. Chi-squared ($\chi^2$) is a statistical measure used to assess the goodness of fit between an observed data set and a model or theoretical data set. In the context of peak fitting in XPS or other data analysis tasks, $\chi^2$ helps evaluate how well the fitted model matches the actual experimental data. The formula for $\chi^2$ is typically expressed as:

$$\chi^2(\vec{p}) = \sum_{i=1}^{N} \frac{[M(i) - S(i,\vec{p})]^2}{M(i)}$$

Here, $M(i)$ is each data point and $S(i,\vec{p})$ is the value of the fit at the same point, A lower $\chi^2$ value indicates a better fit, suggesting that the model closely matches the observed data. A higher $\chi^2$ value suggests a poorer fit, indicating that there are significant discrepancies between the model and the data. A $\chi^2$ value close to 1 indicates a good fit, where the model accounts for most of the variability in the data. It is important to note that while $\chi^2$ is a valuable tool for assessing the quality of a fit, it should be considered alongside other parameters and visual inspection of the fitted model overlaid on the data to ensure that the fit is meaningful and realistic.

Residuals ($R(i)$) are an important parameter used to assess the quality of a peak fit. Residuals represent the differences between the observed data points and the values predicted by the fitted model.

$$R(i) = S(i,\vec{p}) - M(i)$$

The Abbe criterion can also be valuable in evaluating the quality of a fit, especially when it comes to recognizing fits that consistently deviate above or below their corresponding experimental data. It is given by,

$$\Delta_{Abbe} = \frac{\frac{1}{2}\sum_{i=1}^{N-1}[R(i+1) - R(i)^2]}{\sum_{i=1}^{N}[R(i)]^2}$$

## 3.4   Scanning Electron Microscopy

Scanning electron microscopy (SEM) is an imaging technique to visualize the surface morphology and topography of a wide range of samples. It has found applications in numerous scientific fields, ranging from materials science to biology, geology, and nanotechnology. SEM unveils details at the nanoscale level that were once beyond the reach of conventional light microscopy. By harnessing the interactions between electrons and samples, SEM provides information about surface morphology, topography, and composition. In essence, SEM is employed to record images of a sample surface by detecting various signals produced when high energy electrons are focused and interact with the surface of the sample.[86,87]

### 3.4.1   Working Principle

The working principle of scanning electron microscopy (SEM) relies on the interaction between a focused electron beam and the sample. SEM employs an electron gun, typically equipped with a heated filament or field emission source, to emit a stream of high-energy electrons. Moreover, the electron gun generates electrons that are accelerated through the application of high energy within the 0.2 kV-30 kV range. These electrons are then precisely focused and confined into a monochromatic beam, often with a diameter of 100 nm or less, using magnetic field lenses and metal slits within a vacuumed column. Subsequently, the sample surface is scanned in a raster pattern and upon impact with the surface, the electron beam engages with the near-surface region of the sample generating various signals through their interactions with the sample, as shown in Figure 12. These interactions encompass both elastic and inelastic scattering phenomena within the sample.

The accelerating voltage determines the energy of the primary electrons in the electron beam. Electrons with higher kinetic energy penetrate deeper into the sample. The interaction volume is often depicted as having a teardrop shape in SEM. The teardrop shape is a graphical representation that conveys how the primary electron beam interacts with the sample causing formation of including secondary electrons, backscattered electrons, and characteristic X-rays. These signals are detected and used to create SEM images and gather analytical information. Backscattered electrons are high-energy primary electrons that strike the atomic nuclei of the sample and are

backscattered out of the sample. These electrons typically have energy close to that of the primary beam. They are influenced by the density and atomic number of the elements in the sample. Secondary electrons are emitted from the surface of the sample when the high-energy primary electrons from the electron beam strikes the sample. These electrons are typically emitted from the outermost atomic layers of the sample. Due to the limited contrast and low surface sensitivity, achieving high resolution can be challenging. Secondary electrons are sensitive to the topography of the sample and are used for topographical imaging in SEM. They produce detailed images like morphology, revealing surface features and textures. In this thesis, the secondary electrons imaging mode was used for examining thin layers. The detection of emitted X-rays in energy-dispersive X-ray spectroscopy (EDX) within SEM instrument is a crucial process for elemental analysis. However, the sensitivity is inadequate for thin layers of a few nanometer thickness, especially when taking into account that the X-rays coming from a surface layer of about 2-3 μm depth.[87–90]
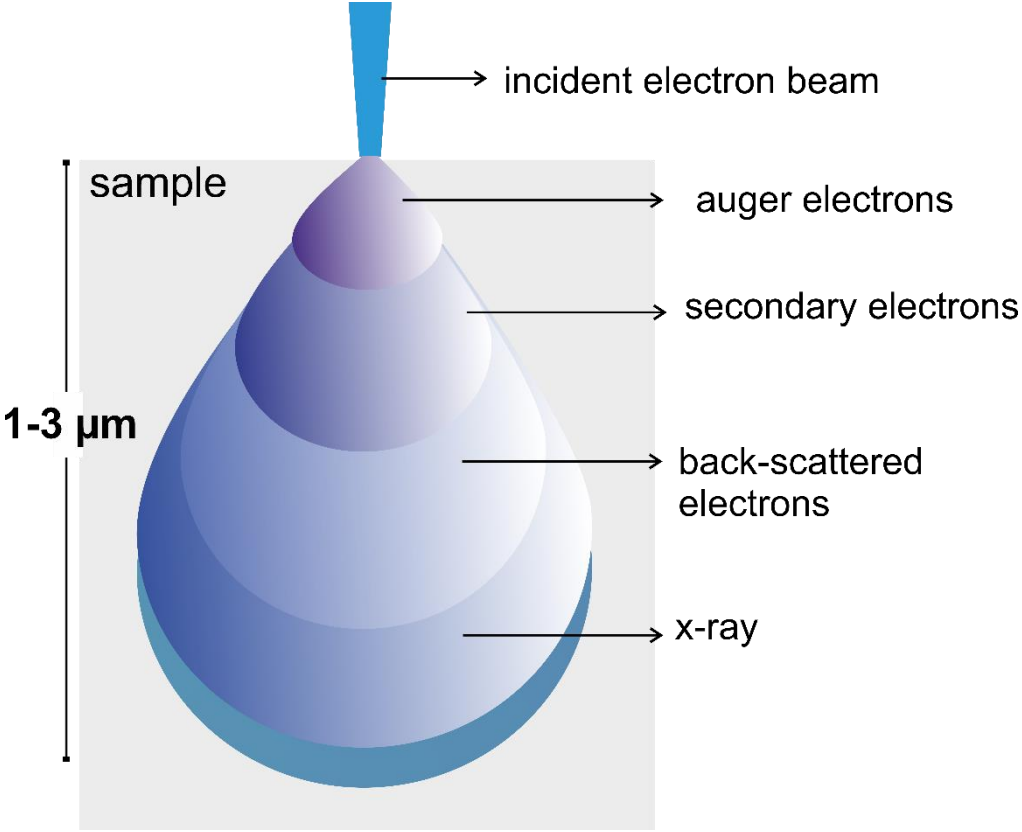


Figure 12: Schematic representation of processes resulting from electron-sample interactions.

Imaging using secondary electron detection can be conducted in both field-free and immersion modes, providing a versatile approach for achieving comprehensive, low-to-high-resolution imaging of diverse samples, potentially achieving magnifications exceeding 100,000x. Field emission scanning electron microscopy (FE-SEM) is typically conducted under high vacuum conditions because the presence of gas molecules can disrupt both the electron beam and the secondary and backscattered electrons essential for imaging purposes.

## 3.5   Transmission Electron Microscopy

Transmission electron microscopy (TEM) is a microscopy technique used to study the internal structure of materials and biological samples at the nanoscale. TEM employs a beam of electrons to image samples, allowing for much higher resolution and the ability to visualize details at the atomic and molecular levels.

### 3.5.1   Working Principle

In TEM, a high-energy electron beam is generated from an electron source, typically a heated tungsten filament or a field-emission gun. The electrons are accelerated to high velocities using electromagnetic fields. The condenser system focuses and converges the electron beam onto the sample. It consists of magnetic lenses and apertures to control the beam size and intensity. The sample, which must be extremely thin, is placed in the path of the electron beam. The electrons are transmitted through the sample and when electrons pass through the sample, they interact with the atoms and electrons in the material, leading to various interactions. Electrons that successfully transmit through the sample using a series of electromagnetic lenses producing high-resolution images by bending the electron beam and focusing them onto a detector.[91,92]

### 3.5.2.   Size Determination of the NPs

TEM enables the study of the morphology and shape of NPs with nanoscale resolution, where precise measurements of nanoparticle sizes are achievable. In this thesis, the size of the NPs was assessed from the obtained TEM images using ImageJ software.

ImageJ is a valuable software tool for extracting quantitative data from TEM images.[93–95] The first step involves calibrating ImageJ using a scale bar in the TEM

image. To distinguish NPs from the background, a threshold range is adjusted to isolate the NPs, converting the image into a binary image. All pixels in the image whose values lie under the threshold are converted to black and all pixels with values above the threshold are converted to white, or vice-versa. Overlapping NPs or NPs sticking to each other can be separated using the watershed option. Then, ImageJ can perform the analysis of NPs. The particle analysis can further be automated by entering the size range or setting the minimum size and maximum pixel. This analysis includes measurements such as NP area and other relevant metrics. From the area, the size of the NPs can be calculated. The data can be exported for further analysis in other software like Excel or Origin.

# 4    Experimental Details

In this chapter, section 4.1 lists all the chemicals and materials used to develop the NAIM systems. In section 4.2, the instrumental descriptions and sample preparations are detailed. All the following reagents were used as received. Deionized water (Elga LabWater, Celle) was used to prepare aqueous solutions.

## 4.1    Chemicals

Table 3. Chemicals used for surface preparation and NP synthesis

| Product | Formula | Supplier | Grade |
|---|---|---|---|
| absolute ethanol | $C_2H_5OH$ | VWR Chemicals | 99.8% |
| acetonitrile | $CH_3CN$ | VWR Chemicals | 99.9% |
| toluene (extra dry) | $C_6H_5CH_3$ | Acros Organics | 99.85 % |
| 5-hydroxy-2-methyl-1,4-naphthoquinone | $C_{11}H_8O_3$ | Sigma Aldrich | |
| phenol | C6H5OH | Sigma Aldrich | 99.0 % |
| 1,2-ethanedithiol | $C_2H_6S_2$ | Sigma Aldrich | 98.0% |
| cysteamine | $C_2H_7NS$ | Sigma Aldrich | |
| tetrabutylammonium hexafluorophosphate | $NBu_4PF_6$ | Sigma Aldrich | 99.0% |
| dopamine hydrochloride | $C_8H_{12}ClNO_2$ | Alfa Aesar | 99% |
| 4-nitrobenzenediazonium tetrafluoroborate | $C_6H_4N_3O_2.BF_4$ | Sigma Aldrich | 97% |
| 3-aminopyridine | $C_6H_5N_3$ | Alfa Aesar | 99% |
| 4-aminothiophenol | $C_6H_7NS$ | Sigma Aldrich | |
| *p*-phenylene diamine | $C_6H_8N_2$ | Sigma Aldrich | 98% |
| hydrochloric acid 37% | HCl | VWR Chemicals | 35.9% |
| hydrofluoric acid | HF | Craft GmBH | 5% |
| sodium nitrite | $NaNO_2$ | Sigma Aldrich | |
| potassium chloride | KCl | Sigma Aldrich | 99.5% |
| sodium bicarbonate | $NaHCO_3$ | Fluka | 99.7% |
| poly(diallyldimethylammonium chloride) | PDDA | Sigma Aldrich | 20 wt% |
| sodium dihydrogen phosphate dihydrate | $NaH_2PO_4\ 2H_2O$ | VWR Chemicals | |
| disodium hydrogen phosphate dihydrate | $Na_2HPO_4\ 2\ H_2O$ | VWR chemicals | |

| | | | |
|---|---|---|---|
| potassium hexacyanoferrate(III) | $K_3[Fe(CN)_6]$ | Alfa Aesar | 99.0% |
| hexaamineruthenium(III) chloride | $[Ru(NH_3)_6]Cl_3$ | Sigma Aldrich | 98.0% |
| ferrocene methanol (FcMeOH) | $C_{11}H_{12}FeO$ | Alfa Aesar | 97.0% |
| silver nitrate | $AgNO_3$ | Carl Roth GmbH & Co | 99.9% |
| gold(III)chloride trihydrate | $HAuCl_4\ 3H_2O$ | Sigma Aldrich | 99% |
| tannic acid | $C_{76}H_{52}O_{46}$ | Sigma Aldrich | |
| trisodium citrate dihydrate | $Na_3C_6H_5O_7.2H_2O$ | | 99.9% |

Table 4. NPs used for the study

| Product | Abbreviation | Supplier | Concentration |
|---|---|---|---|
| *Commercially purchased NPs* | | | |
| amine-modified monodispersed silica NPs | $SiO_2-NH_2$ | HiQ Nano | 20 mg/mL |
| carboxyl-modified monodispersed silica NPs | $SiO_2-COOH$ | HiQ Nano | 20 mg/mL |
| sulfate latex beads | PS | Fisher Scientific | 8% w/v |
| gold NPs, stabilized suspension in citrate buffer | Au-Cit | Sigma Aldrich | - |
| silver NPs, stabilized suspension in citrate buffer | Ag-Cit | Sigma Aldrich | - |
| *Synthesized NPs* | | | |
| citrate-stabilized gold NPs | Au-Cit | - | - |
| citrate-tannic acid stabilized Ag NPs | CT-Ag | - | - |
| amine-modified Au NPs | $Au-NH_2$ | - | - |

## 4.1.1 General Cleaning Procedure

Glassy carbon (GC) plates were purchased from HTW Hochtemperatur-Werkstoffe GmbH, and ITO coated glass slides with a surface resistivity of 8 – 12 Ω were ordered from Sigma Aldrich. The cleaning of substrates is a crucial step in preparing them for various applications, including electrochemical experiments, surface modification, and material characterization. The GC plates were polished with 0.3 μm and 0.05 μm alumina slurry on a polishing pad, followed by sonication in deionized water for 10 min. ITO substrates were cleaned in ethanol, acetone, and deionized water for 10 min each in an ultrasonic bath, followed by drying in an Ar stream.

### 4.1.2 Synthesis of NPs

The synthesis of NPs involves creating nanoscale-sized particles with controlled size, shape, composition, and properties. Different methods are available for nanoparticle synthesis, each tailored to specific properties and applications. The analyte NPs used in the study of plumbagin-based NAIM, PDA-based NAIM, PPD, and ATP-based NAIM systems were synthesized according to the procedure of Bastús et al.[96,97]

**Synthesis of Citrate-Stabilized Au NPs.** The citrate-stabilized Au NPs (Au-Cit NPs) were synthesized based on the kinetically controlled seeded growth approach established by Bastús et al.[96] to obtain monodisperse NPs. Initially, gold seeds were prepared by adding 1 mL of 25 mM HauCl$_4$ into 150 mL of 2.2 mM sodium citrate at 100 °C under vigorous stirring. The reaction continued until the solution colour changed from yellow to soft pink. When the reaction was finished, the solution was cooled down to 90 °c. This was followed by the growth steps to achieve NPs of the desired size. For this, 1 mL of 25 mM HAuCl$^4$ was added to the same reaction vessel. After 30 min, the reaction was finished. This step was repeated again. After that, the sample was diluted by extracting 55 mL of sample and adding 53 mL of deionised water and 2 mL of 60 mm sodium citrate. After the fifth growth step, gold NPs of size 40 nm were obtained.

**Synthesis of Citric Acid-Tannic Acid Complex-Stabilized Ag NPs.** The citric acid-tannic acid complex-stabilized Ag NPs (Ag-CT NPs) was synthesized based on the kinetically controlled seeded growth approach established by Bastús et al. [97] to obtain monodisperse NPs. In a three-neck round bottom flask, 100 mL of 0.1 mM tannic acid and 5 mM sodium citrate solution was boiled for 15 min at 100 °C. After 15 min, 1 mL of 25 mM AgNO$_3$ solution was added under vigorous stirring. The colour of the solution was changed to bright yellow, indicating the synthesis of Ag seeds. After cooling the reaction mixture to 90°C, the seed solution was diluted by extracting 19.5 mL of reaction solution and added 16.5 mL of deionized water. Immediately after this, the following reagents were added: 500 μL of 25 mM sodium citrate, 1.5 mL of 2.5 mM tannic acid and 1 mL of 25 mM AgNO$_3$. After 20 min, the reaction was finished. This solution was used as the seed solution for the next growth step. The process was repeated until 7th growth step to achieve 40 nm Ag NPs and until 12th growth step for 60 nm Ag NPs.

**Synthesis of Amine Modified Gold (Au-NH₂) NPs.** To the solution of 40 mL 1.42 mM HAuCl₄, 400 μL of 213 mM 2-aminoethanethiol was added. The mixture was stirred at room temperature for 20 min. Subsequently, 10 μL of 10 mM NaBH₄ was added, and the resulting solution was vigorously stirred in the dark at room temperature for an additional 10 min. The colour of the solution changed from opaque brown to wine red colour. After gentle stirring, the sample was stored in at 4°C [98]

## 4.2   Instrumentations Used for Preparation and Characterization of NAIM Systems

**Electrochemical Experiments.** Electrochemical measurements (CV, CA, and LSV) were performed with an Autolab Potentiostat PGSTAT128N (Metrohm, Filderstadt, Germany) and CHI 660 A potentiostat (CH Instruments, Electrochemical Analyzer, Austin, TX, USA) at room temperature in a three-electrode cell. Glassy carbon (GC) plates and ITO-coated glass slides were used as the working electrodes. A Pt wire or Pt sheet was used as the auxiliary electrode. The reference electrode was Ag/AgCl (3 M KCl) for electrografting and electropolymerization processes in aqueous-based electrolytes, while Ag/AgNO₃ (0.1M tetrabutylammonium hexafluorophosphate (TBAPF₆) / acetonitrile (ACN)) reference electrode was used for non-aqueous solutions. All potentials are given with respect to the used reference electrode.

**Scanning Electron Microscopy.** The characterization of NAIM at various stages of preparation and the cross-sectional studies were carried out with a fast ion beam scanning electron microscope (Helios Nanolab 600i system, FEI Company, Eindhoven, The Netherlands). The topography images were recorded in the immersion mode with a TLD detector at acceleration voltages between 1 – 10 kV, and the working distance was adjusted between 3 – 6 mm. The sample was attached to a SEM sample holder using a copper tape. For the cross-sectional studies, initially, a 10 nm thick Pt layer was deposited over the sample surface to reduce the charging. Then, a 0.4 μm deep cut was made on the sample using a Si application needle. The cross sections were visualized at an angle of 52° in the immersion mode at an acceleration voltage of 5 kV.

**Atomic Force Microscopy.** AFM measurements were carried out with a Dimension 3100 AFM equipped with a Nanoscope IIIa controller (Veeco Instruments Inc., Santa Barbara, CA, USA). Topography and phase imaging of the samples were recorded in the intermittent contact mode using an Al-coated $Si_3N_4$ cantilever (NCHV-A tip, Bruker, Camarilla, CA, USA) with a spring constant of 42 N m⁻¹. Thickness studies were

recorded in contact mode using reflective aluminium-coated FESPA-V2 tips (Bruker, CA, USA) made of antimony-doped Si with a spring constant of 2.8 N m$^{-1}$ and reflective gold-coated MSCT tip (Bruker, CA, USA) made of Si$_3$N$_4$ with a spring constant of 0.6 N m$^{-1}$. Images were obtained at a scan rate of 1.0 – 3.0 Hz in both contact and intermittent contact modes with a resolution of 512 x 512 pixels.

Thickness studies are performed as follows: The procedure commenced with selecting an area of 5 µm x 5 µm of the polymer film for analysis. The AFM tip was positioned above this area and topography was measured at a setpoint of 0 V and at a scan rate of 3.0 Hz. From this region, a 1 µm x 1 µm area was chosen, and the imaging was continued at a scan rate of 1 Hz. A predefined setpoint voltage of 10V was applied to the tip as it gently scratches the surface of the film. The lateral movement of the tip was initiated while maintaining a constant force. This lateral movement created a controlled scratch on the surface of the polymer film. This continued until the typical structure of the underlying substrate became evident. Subsequently, an area of 5 µm x 5 µm of the polymer film including the scratched region was imaged at a setpoint voltage of 0 V and a scan rate of 3.0 Hz. The software NanoScope Analysis 1.5 was used for the thickness and roughness analysis of the samples.

To extract the thickness of the films, the relative height measurements between two selected areas were measured. An area of the film was selected so that the scratched area and the intact film were included in the selected area. The cursors should be carefully placed (as shown in Figure 13), where one set at the abraded area (yellow box in Figure 13) and the other set on the film surface (red box in Figure 13). A height profile will be generated from the averaged data from the selected regions. A tool named 'step height' was used to determine the film thickness. The areas of analysis should be carefully chosen by avoiding agglomerates or other non-specific topographic features, which could interfere with the accuracy of the measurements. The roughness was also measured using the 'roughness' tool of the software by clearly defining a specific area for the measurements.
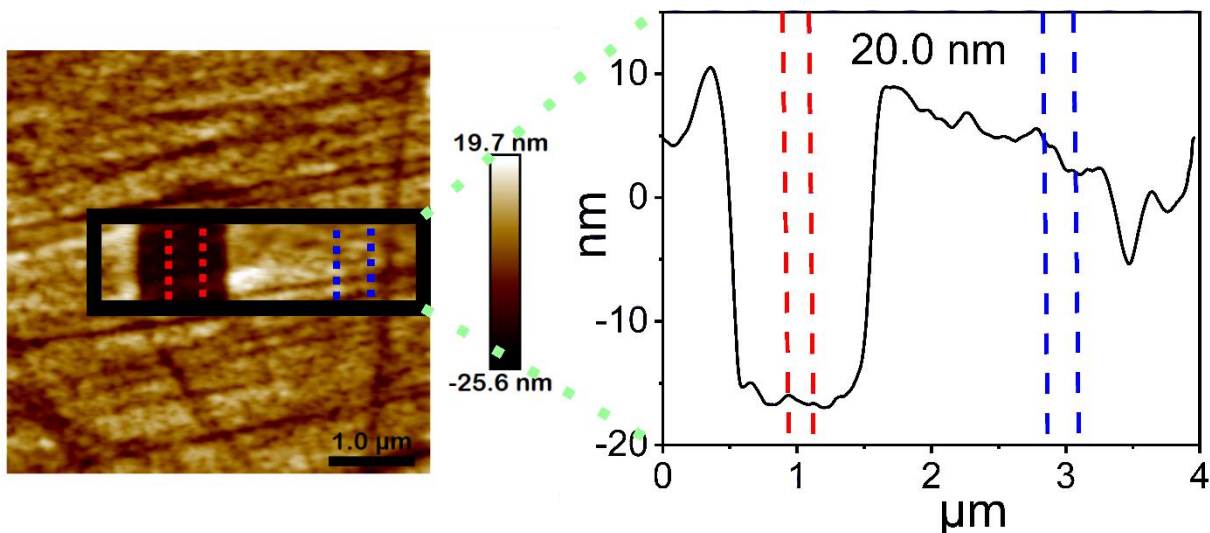
Figure 13: An example of thickness determination by AFM of a polyplumbagin-based polymer deposited on GC substrate.

**X-ray Photoelectron Spectroscopy.** XP spectra were obtained with an ESCALAB 250 Xi (Thermo Fisher Scientific, East Grinstead, UK) with monochromatized Al Kα radiation ($hv$ = 1486.6 eV). Spectra were measured with pass energies of 200 eV for survey scans. The internal electron flood gun was used for charge compensation. All spectra were referenced to remaining adventitious carbon at 248.8 eV. For data processing, Avantage software of v5.9911 was used. The obtained spectra were fitted using a smart background and convolution of Gaussian and Lorentzian contributions. XPS was used to study the NAIM systems before and after removing the analyte NPs.

**Transmission Electron Microscopy.** The size distribution of the commercially bought $SiO_2$-$NH_2$ NPs and PS NPs, synthesized Au-Cit NPs and Ag-CT NPs were studied using a JEM2100F TEM (JEOL GmbH, Freising, Germany). The $SiO_2$-$NH_2$ NPs were diluted 5 times, and the PS NPs were diluted 10 times using deionized water, whereas the Au-Cit NP and Ag-CT NP solutions were used without dilution. A 10 µL droplet of the colloidal NP solution was drop-casted on a Cu grid and dried in the air before being used for the TEM analysis. All the images were recorded at an acceleration voltage of 80 kV.

## 4.3 Immobilization of Template Nanoparticles

Immobilization of template NPs onto a substrate surface is the initial step in the development of the NAIM system. Proper control of experimental conditions is crucial to achieve precise and reliable immobilization of template NPs onto substrates.

### 4.3.1 Attachment of Amine-Modified SiO₂ NPs

A well-defined arrangement of template amine-modified $SiO_2$ NPs ($SiO_2$-$NH_2$) on GC substrate is required for the development of the plumbagin-based NAIM system. The NP solution was sonicated in the ultrasonic bath for 5 min, followed by a 30 s shaking prior to its use. This process was repeated until a homogeneous dispersion of NPs was obtained. The cleaned GC surface was activated in an aqueous solution of $NaHCO_3$ for a potential range from -1.1 to 1.8 V at 0.1 V s$^{-1}$ vs Ag/AgCl.[99] After 40 cycles, the GC plate was removed from the electrochemical cell, rinsed in deionised water, and dried in Ar. Electrochemical activation of a glassy carbon electrode prepares the electrode for various electrochemical experiments by improving its surface properties and increasing its electrochemical activity. The activation of GC enhances the electrochemical activity of the electrode by modifying its surface properties. This leads to improved current response and higher sensitivity in electrochemical experiments. It can modify specific surface properties such as roughness, porosity, and introduce useful functional groups on to the GC surface. The activated GC was then immersed in an aqueous solution of $SiO_2$-$NH_2$ NPs for 1 h. Afterwards, the $SiO_2$-$NH_2$/GC was rinsed with water to remove the weakly adsorbed NPs from the surface followed by drying in Ar.

### 4.3.2 Electrostatic Attachment of SiO₂-COOH NPs and Sulfate Modified Polystyrene NPs

The negatively charged carboxylate functionalized $SiO_2$ NPs ($SiO_2$-COOH) or sulfate-modified polystyrene NPs (PS NPs) were attached to a GC or ITO substrate using a positively charged primary layer. After cleaning, the ITO substrate or GC substrate was immersed in a solution of 0.01 wt % poly(diallyldimethylammonium chloride)(PDDA) for 20 min. Later, the PDDA-modified substrates were immersed in

the SiO$_2$-COOH NP solution for 1 h or PS NP solution for 2 h. SEM images confirmed the attachment of SiO$_2$-COOH NPs or PS NPs onto PDDA-modified ITO or GC.

## 4.4 Electrodeposition of Thin Film Matrices

### 4.4.1 Preparation of Plumbagin-Based Matrix

The electrodeposition of plumbagin was based upon Dongmo et al.[100] Initially, a stock solution of 10 mM plumbagin in acetone is prepared and stored at -20°C. From this, a 0.2 mM plumbagin solution was prepared using a 0.1 M phosphate solution of pH 4. The SiO$_2$-NH$_2$ GC was immersed in this solution and the potential was scanned between 0.1 V and -0.3 V vs Ag/AgCl for 30 cycles at 0.01 V s$^{-1}$. Afterwards, the plg(SiO$_2$-NH$_2$/GC) was exposed to 0.2 mM plumbagin solution in a 0.1 M phosphate buffer of pH 7. The potential was scanned between -0.8 to 1.4 V vs Ag/AgCl at 50 mV s$^{-1}$ for 15 potential cycles for the electropolymerization of plumbagin.

For the covalent modification, 1 mM 1,2-ethanedithiol or 1 mM cysteamine solution was prepared using 0.1 M TBAPF$_6$ in ACN. The polyplg-plg-SiO$_2$-act GC was exposed to the corresponding solution and the potential was held at -0.8 V vs Ag/AgNO$_3$ for 800 s using chronoamperometry. After 800 s, the sample was washed with ACN and deionised water. A NAIM system without covalent modification was also prepared for comparative studies.

Each NAIM system [dithiol/polyplg/plg(SiO$_2$-NH$_2$)/GC, cysteamine/polyplg/plg(SiO$_2$-NH$_2$)/GC, polyplg/plg(SiO$_2$-NH$_2$)/GC] was modified with a polyphenol (pph) layer in an aqueous solution of 50 mM phenol in 0.1 M NaH$_2$PO$_4$. The potential was cycled between -1.2 V and 1.4 V vs Ag/AgCl at 50 mV s$^{-1}$ for 5 cycles. After electropolymerization, each sample was rinsed in deionised water, and dried in Ar.

### 4.4.2 Formation of Polydopamine-Based Matrix by Electropolymerization

Polydopamine was electropolymerized on PS NP modified ITO substrate (PS/ITO) from a deaerated 10 mM dopamine solution in 10 mM phosphate buffer. The pH of the solution was maintained at 7.4 to impede the self-polymerization of dopamine. The potential of the (PS)PDDA/ITO sample was cycled between -0.8 V to 1.5 V vs Ag/ AgCl for 25 cycles at $v$ = 0.02 V s$^{-1}$. Afterwards, the sample was removed from the cell, rinsed with deionized water, and dried in an Ar stream.

### 4.4.3 Formation of Aryl Diazonium-Based Matrix by Electrografting

**3-Aminopyridine-Based Matrix.** A thin film was electrografted from in-situ generated 3-diazopyridinium cations on cleaned GC, cleaned ITO, (SiO$_2$-NH$_2$)PDDA/GC or on (PS)PDDA/ITO according to the method described by Agullo et al.[101] For the insitu generation of the diazonium salts, 40 mM NaNO$_2$ was added to a solution of 20 mM 3-aminopyridine + 0.5 M HCl at low temperature (0 - 5°C) under vigorous stirring. After 1 min, the substrate was immersed into the solution. After applying a potential of 0.8 V vs Ag/AgCl for 10 s, the substrate was cycled in the potential range between 0.8 to -0.8 V vs Ag/AgCl. After 10 potential cycles (20 cycles for (PS)PDDA/ITO)), the sample was removed, rinsed in deionised water and dried in an Ar stream.

***Synthesis of 4-((Triisopropylsilyl)ethynyl)benzenediazonium tetrafluoroborate (TIPS).*** The diazonium salt was prepared based on Leroux et. al.[102] A round-bottomed flask with 1 equivalent of 4-((triisopropylsilyl)ethynyl)aniline and 3 equivalents of aqueous HBF$_4$ was stirred in an ice bath under continuous stirring. To this stirring solution, 1.5 equivalent of NaNO$_2$ was added. The resulting solution was stirred for a duration of 2 h. Following this, the mixture was filtered and subsequently washed with 5 wt% NaBF$_4$, cold water, and cold methanol. The obtained product was then dissolved in a dimethyl chloride solvent and stored in a refrigerator. After 24 h, the solvent was removed using a freeze pump, and the product was dried under vacuum for several hours. The total yield of the product was 6.27 grams. The precursor 4-((triisopropylsilyl)ethynyl)aniline was synthesized according to Anderson et al.[103]

**TIPS/NB-Based Matrix.** A binary layer of TIPS and NB was electrografted on cleaned ITO or (SiO$_2$-COOH)PDDA/ITO according to the Leroux et. al.[104] The initial TIPS layer was electrografted from 1 mM TIPS + 0.1 M TBABF$_4$ in ACN at a scan rate of 0.05 V s$^{-1}$. After 5 cycles, the sample was rinsed in deionised water and dried in Ar stream. These samples are denoted as TIPS/ITO or TIPS/(SiO$_2$-COOH)PDDA/ITO. A second layer was electrografted on TIPS/ITO or TIPS/(SiO$_2$-COOH)PDDA/ITO from 1 mM NBD + 0.1 M TBABF$_4$ in ACN at a scan rate of 0.05 V s$^{-1}$. After 10 cycles, the sample was rinsed in deionised water and dried in an Ar stream. These samples are denoted as NB/TIPS/ITO or NB/TIPS/(SiO$_2$-COOH)PDDA/ITO.

**4-Aminothiophenol or *p*-Phenylenediamine-Based Matrix.** The 4-aminothiophenol (4-ATP) (or *p*-phenylene diamine (*p*-pd)) film was electrografted from in-situ generated diazonium salt of 4-ATP (or *p*-pd) on cleaned ITO or (SiO$_2$-COOH)PDDA/ITO according

to the method described by Gooding et. al.[105] For the insitu generation of the diazonium salts, 1 mm $NaNO_2$ was added to a solution of 1 mM 4-ATP(or *p*-pd) + 0.5 M HCl at low temperature (0 - 5 °C) under vigorous stirring. After 10 min, the sample was immersed into the solution. The sample was cycled in a potential range between 0.6 and -1.0 V vs Ag/AgCl. After 30 cycles, the sample was removed from the solution, rinsed in deionised water and dried in an Ar Stream. The samples are denoted as 4-ATP/ITO, 4-ATP/($SiO_2$-COOH)PDDA/ITO, p-pd/ITO, and p-pd/($SiO_2$-COOH)PDDA/ITO.

## 4.5    Removal of Template Nanoparticles

### 4.5.1  Etching of $SiO_2$ NPs

The $SiO_2$-$NH_2$ or $SiO_2$-COOH template NPs were removed from the NAIM systems to form complementary cavities. This was done by immersing the samples with $SiO_2$ template NPs in 5% hydrofluoric acid for 3 min. For control experiments, samples without $SiO_2$ template NPs were also immersed in 5% HF to compare. After the immersion in HF, the samples were thoroughly rinsed to remove the acid from the sample surface and dried in Ar stream. The cavities formed after the removal of template NPs are indicated as brackets () in the sample codes.

### 4.5.2  Solvent-Based Removal of PS NPs

The samples with PS NPs as template NPs were immersed in toluene for the removal of PS NP. Toluene is a good solvent for PS NPs. The samples were immersed in toluene around 20 h for the removal of PS NPs. For control experiments, samples without PS template NPs were also immersed in toluene. After the immersion in toluene, the samples were thoroughly rinsed and dried in Ar stream. The cavities formed after the removal of template NPs are indicated as brackets () in the sample codes.

## 4.6    Reuptake Studies

The size-selective recognition ability of the NAIM systems was studied by assessing the reuptake ability of these systems. The NAIM systems after the removal of template NPs were immersed in a solution of citrate functionalized Au or Ag NPs of different sizes (as analyte NPs) for 12-15 h. Control studies were carried out in a similar manner

using non-imprinted matrix systems i.e., without cavities. Afterwards, the samples were rinsed thoroughly in deionised water to remove the loosely adsorbed NPs and dried in an Ar stream. The presence of specifically adsorbed NPs was studied by LSV.

# 5    Polyplumbagin-Based NAIM

The development of a NAIM system is challenging as various factors play a role in the advancement of the system. From the previous chapters, it is evident that factors like film thickness, stability of the matrix, assembly of template NPs and their removal, film overgrowth, etc. have a significant influence on the success of a NAIM system.

In view of these challenges, we demonstrate here a new NAIM system with insulating template NPs and conducting analyte NPs as shown in Figure 14. This system allows the template removal and detection of the analyte NPs using orthogonal methods, e.g., chemical etching of template NPs and electrodissolution of analyte NPs. Electrochemical detection seems a natural choice for a recognition system supported on an electrode surface because it can potentially distinguish between NPs located in the cavities and involved in electron transfer with the electrode and those non-specifically adhering to the outer parts of the NAIM film and thus unable to electronically communicating with the electrode.[41] Furthermore, we introduce a chemical post-functionalization of the matrix to modify and adapt the recognition ability of NAIM system. A specific example of this idea was realized by assembling amine-modified silica template NPs ($SiO_2$-$NH_2$ NPs) onto an activated glassy carbon (GC) surface (Figure 14c), followed by electrodeposition of a plumbagin-based matrix (Figure 14d).[100] The unsubstituted position 3 at the quinoid ring of the polyplumbagin (Figure 14e) is then exploited for conjugate addition of a thiol, specifically of 1,2-ethanedithiol or cysteamine followed by the electropolymerization of phenol, to block the surface (Figure 14f). The reactions were followed by cyclic voltammetry (CV) and the presence of thiols and amino groups in the film was verified by X-ray photoelectron spectroscopy (XPS). After the removal of template $SiO_2$-$NH_2$ NPs in diluted hydrofluoric acid (HF), the covalently modified NAIM systems are exposed to citrate-functionalized gold NPs (Au-Cit NPs) and the uptake ability is studied and compared to a matrix without covalent modifications under different pH conditions. The amount of Au NP inside the cavities was quantified by the charge transferred during electrodissolution of the Au NPs in 3 M KCl in linear sweep voltammetry (LSV). The schematics in Figure 14 shows the different steps in developing the NAIM system.

The results obtained were published in ChemElectroChem.[106] I conducted the experiments and prepared the draft for the manuscript. This was further checked and modified by Prof. Wittstock as coauthor and supervisor.
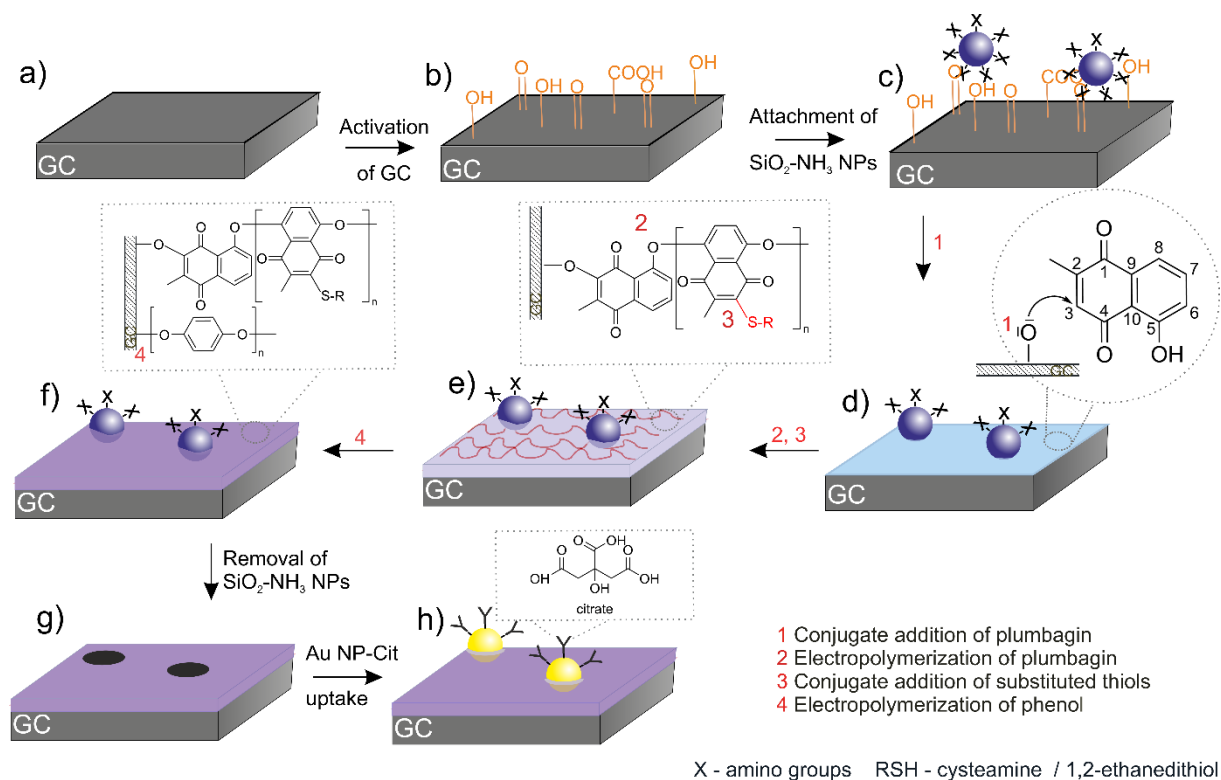


Figure 14. Schematic representation of the NAIM system. a) A precleaned glassy carbon (GC) surface; b) activation of the GC surface in 0.1 M NaHCO$_3$; c) deposition of SiO$_2$-NH$_2$ template NPs onto the activated GC surface; d) conjugate addition of plumbagin to the activated GC surface; e) electropolymerization of plumbagin followed by the conjugate addition of substituted thiols to plumbagin and f) electropolymerization of a polyphenol layer; g) removal of SiO$_2$-NH$_2$ NPs and h) uptake of Au-Cit NPs from an aqueous NP suspension. Reprinted from own publication[106] under license CC BY 4.0. Copyright 2023 The Authors.

## 5.1    Attachment of SiO$_2$-NH$_2$ NPs onto Activated GC

The selection of template and analyte NPs is crucial for determining the selectivity of a NAIM system and depends on the application, the nature of NPs and their surface properties. Herein, we relied on the approach of self-assembly,[107] where nanoparticles are arranged into ordered structures. It occurs due to the inherent properties of NPs, such as their size, shape, surface chemistry, and interparticle interactions. It is important to note that specific details like distribution and coverage of NPs on the substrate surface are significant for the efficacy of NAIM system. The template NPs

used for this NAIM system are amine-modified silica NPs (SiO$_2$-NH$_2$), which were commercially obtained. Figure 15 shows the TEM image and the corresponding size distribution of SiO$_2$-NH$_2$ NPs.
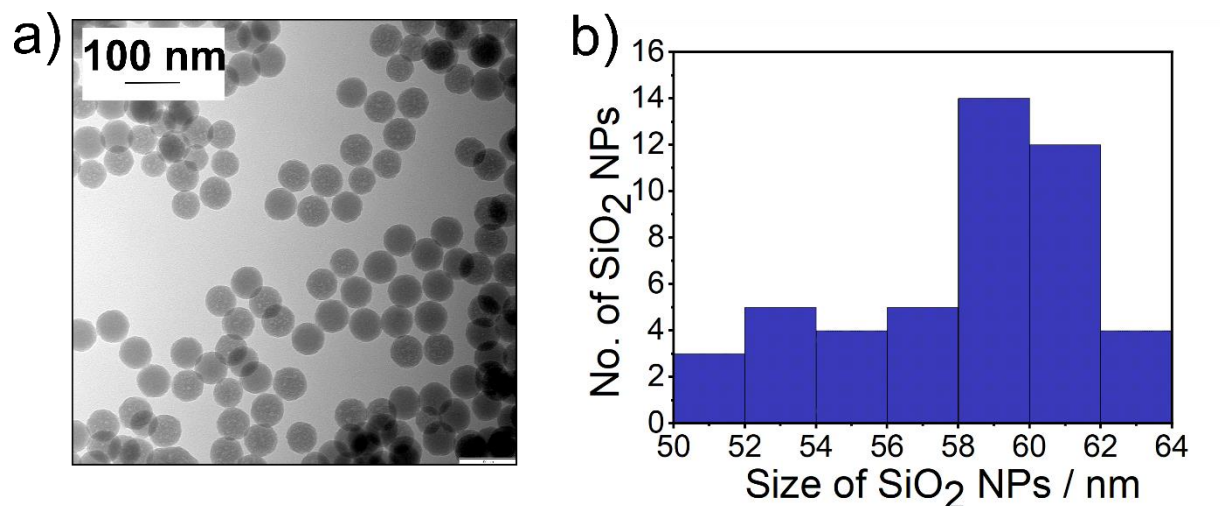


Figure 15. a) TEM images and b) size distribution of commercially bought amine-modified SiO$_2$–NH$_2$ NPs. Reprinted from own publication[106] under license CC BY 4.0. Copyright 2023 The Authors.

Initially, the glassy carbon plates were polished with 0.3 µm and 0.05 µm alumina slurry as discussed in section 4.2 to ensure a clean, uniform, and well-defined surface, promoting reliable and accurate electrochemical measurements. The cleaned GC surface is activated in 0.1 M NaHCO$_3$. This created oxygen-containing groups on the surface.[108] Also, the electrochemical pretreatment of glassy carbon aids in obtaining reproducible surfaces and offers great selectivity for different functional groups.[109] Similar pretreatments have been reported to increase the effective surface area and electron transfer kinetics.[110] The activation of GC surface is indeed required for the development of the polyplumbagin matrix, which will be explained later in this Chapter.
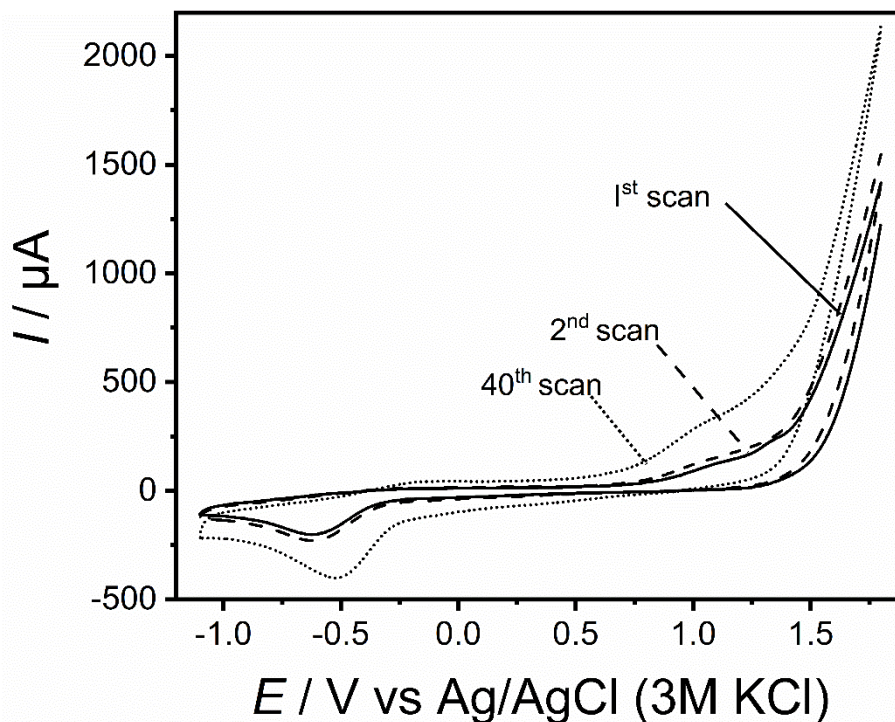
Figure 16. Cyclic voltammogram of activation of glassy carbon surface in 0.1 M NaHCO$_3$ at $v$ = 0.1 V s$^{-1}$. Reprinted from own publication[106] under license CC BY 4.0. Copyright 2023 The Authors.

The surface of the activated glassy carbon is enriched with oxygen-containing functional groups as shown in Figure 14b. The SEM image of the surface of activated GC is shown in Figure 17a. The SEM image reveals the presence of a highly porous layer that developed on the surface of the GC electrode during the activation step. This activated GC was immersed in an aqueous solution of SiO$_2$-NH$_2$ NPs for 1h. After 1h, the GC substrates were removed from the NP solution, rinsed in deionised water, and dried in Ar. Figure 4b shows the GC electrode after the immersion of activated GC in aqueous solution of SiO$_2$-NH$_2$ NPs. The SiO$_2$-NH$_2$ template NPs can be seen adsorbed to the activated GC surface which is supported by the interaction between the NH$_2$ groups in the ligand shell of the NPs and the oxygen-containing functionalities on the GC surface.
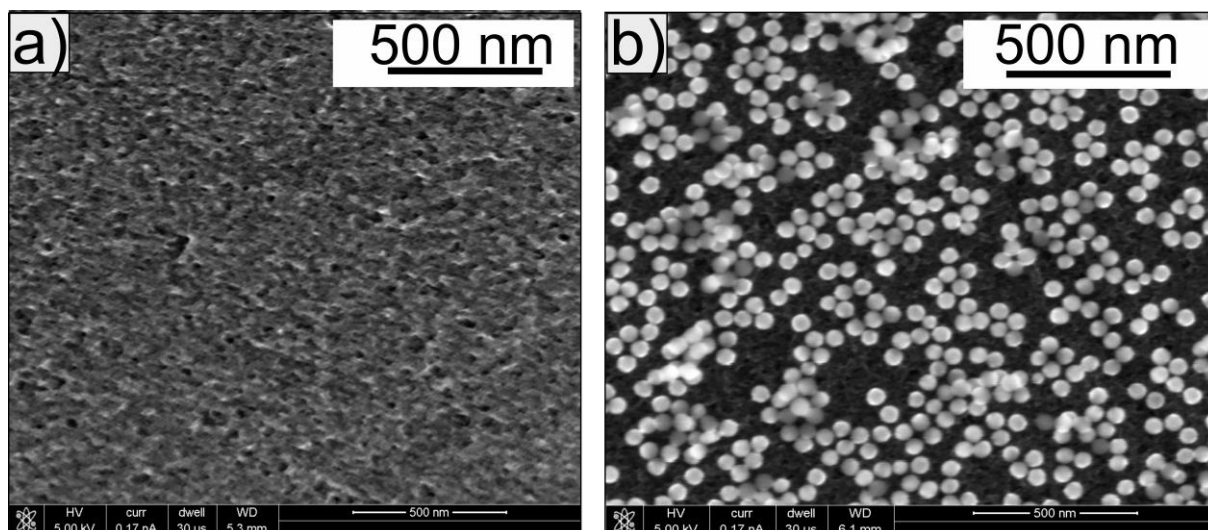
Figure 17. SEM images of a) activated GC, b) GC after a 2 h immersion in $SiO_2$-$NH_2$ NP dispersion. Reprinted from own publication[106] under license CC BY 4.0. Copyright 2023 The Authors

## 5.2 Formation of Polyplumbagin-Based NAIM

Qunione-hydroquinone (Q/QH2) compounds are well-known as organic redox-couple.[111] They are involved in the production of reactive oxygen species (ROS), which has been exploited as cathode materials,[112] dynamic self-assembled monolayers (SAMs),[113] and are integrated into smart devices,[114] biosensors,[115] etc. Besides these applications, Q/QH2 compounds exhibit therapeutic benefits and are used for the treatment of viral, bacterial, fungal infections, acne, inflammatory diseases, etc. These compounds show concentration-dependent cytotoxic properties which can be detrimental to the normal cellular function.[116]. Data is insufficient to prove the adverse effects of these compounds on human beings.

Plumbagin (5-hydroxy-2-methyl-1,4-napththoquinone), is a material of interest among the Q/QH2 compounds because of its redox chemistry. The structure of plumbagin is given in Figure 1d and the structure of surface grafted plumbagin is given in Figure 1e. The quinone redox couple is accountable for the production of ROS while the phenolic group can facilitate the formation of a thin film.[117] The electropolymerization of plumbagin is analogous to the oxidative electropolymerization of phenol leading to the formation of a self-limiting film. Electropolymerization of plumbagin by the conventional head to tail coupling[118] passivates the electrode surface with the formation of a thin insulating film.

45

A study by Dongmo et al.[100] proposed a new method for the electropolymerization of plumbagin, which circumvents the problem of electrode passivation and resulted in a conducting film. Instead of directly electropolymerizing plumbagin on the electrode surface, an initial layer of plumbagin was electrografted onto the activated GC surface via conjugate addition (Eq. (1)). For this, the bare GC surface was activated as described in section 5.1. The presence of an unsubstituted position on the quinoid ring which is prone to nucleophilic attack was exploited here. The oxygen functionalities on the activated GC surface acted as nucleophiles and attacked the unsubstituted position of the quinoid ring of plumbagin (Eq. (1)) forming a monolayer of plumbagin. This monolayer-covered surface was then used to electropolymerize plumbagin. The film obtained in this way showed substantial difference in the film properties compared to the directly electropolymerized plumbagin film onto GC.[100] The continuously growing, conducting plumbagin films exhibited improved electrocatalytic activity and provided control over the thickness of the deposited films. The polymerized plumbagin layer developed through this method is particular advantageous for the development of sensors. The free position on the quinoid ring remains unhindered even after the electropolymerization and can be exploited for the post modification of the polyplumbagin film via conjugate addition of nucleophiles. The polymerized plumbagin layer developed through this method offers flexibility and particular advantageous for the development of sensors.

### 5.2.1 Electrografting of Plumbagin on $SiO_2$-$NH_2$/GC

The GC surface was modified according to Dongmo et al[100]. Initially, the GC surface was activated in 0.1 M $NaHCO_3$ modified with $SiO_2$-$NH_2$/GC as discussed in section 5.1. When the activated GC electrode was exposed to a 0.2 mM plumbagin solution, the nucleophilic oxygen-containing functional groups on GC surface enter in a conjugate addition with the only available addition site in the plumbagin, as shown in Eq. (1).
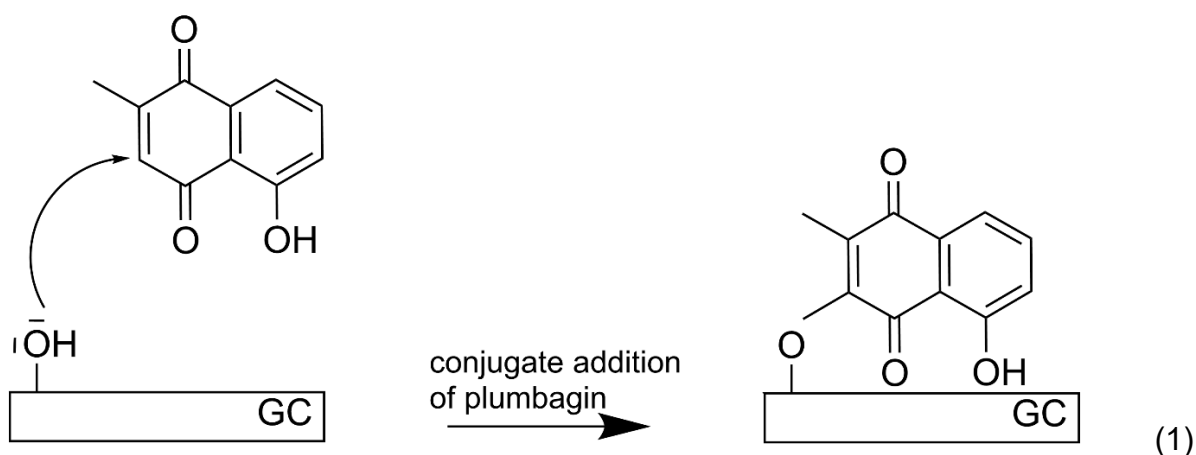
(1)

Figure 18 depicts the cyclic voltammogram of plumbagin electrografting onto activated GC. The voltammogram shows the anodic and cathodic peaks corresponding to the quinone/hydroquinone (Q/QH$_2$) moiety of plumbagin. This sample state can be abbreviated as plg(SiO$_2$-NH$_2$)/GC. A prominent reduction wave at -0.15 V vs Ag/AgCl and oxidation wave at -0.1 V vs Ag/AgCl corresponds to the Q/QH$_2$ redox couple, which is stable for several cycles.
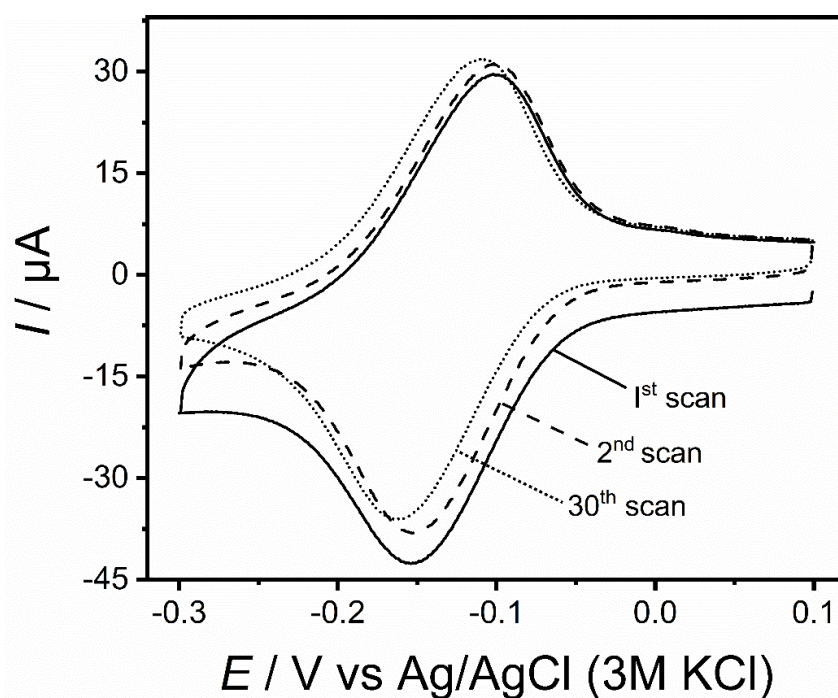


Figure 18. Cyclic voltammogram during grafting of a monolayer of plumbagin to activated GC in deaerated 0.2 mM plumbagin + 0.1 M phosphate solution, pH 4, $v$ = 0.01 V s$^{-1}$. Reprinted from own publication[106] under license CC BY 4.0. Copyright 2023 The Authors

### 5.2.2 Electropolymerization of Plumbagin Onto plg(SiO$_2$-NH$_2$)/GC

Following the electrografting of plumbagin, this monolayer-covered surface is used to electropolymerize plumbagin around the template NPs yielding a permeable film of defined and adjustable thickness.[100,119] Figure 19 depicts the cyclic voltammogram for polyplumbagin (polyplg) electropolymerization on plumbagin-modified activated GC, suggesting the formation of a permeable film. The sample code used for this stage is polyplg/plg(SiO$_2$-NH$_2$)/GC.

The cyclic voltammogram in Figure 19 indicates the continuous growing of polyplg film. An oxidation wave at 0.97 V in the first scan can be assigned to the oxidation of phenolic groups of plumbagin. A small decrease in the oxidation current for phenolic groups can be witnessed in the second scan which remains stable in the subsequent scans. Also, the signal for Q/QH$_2$ couple is present throughout the scans. All these aspects observed in the voltammogram point towards the continuous growth of the film. On adjusting the number of scans, film thickness can be controlled.[100] It is to be noted that the thickness of the matrix is a decisive factor for the success of a NAIM system.
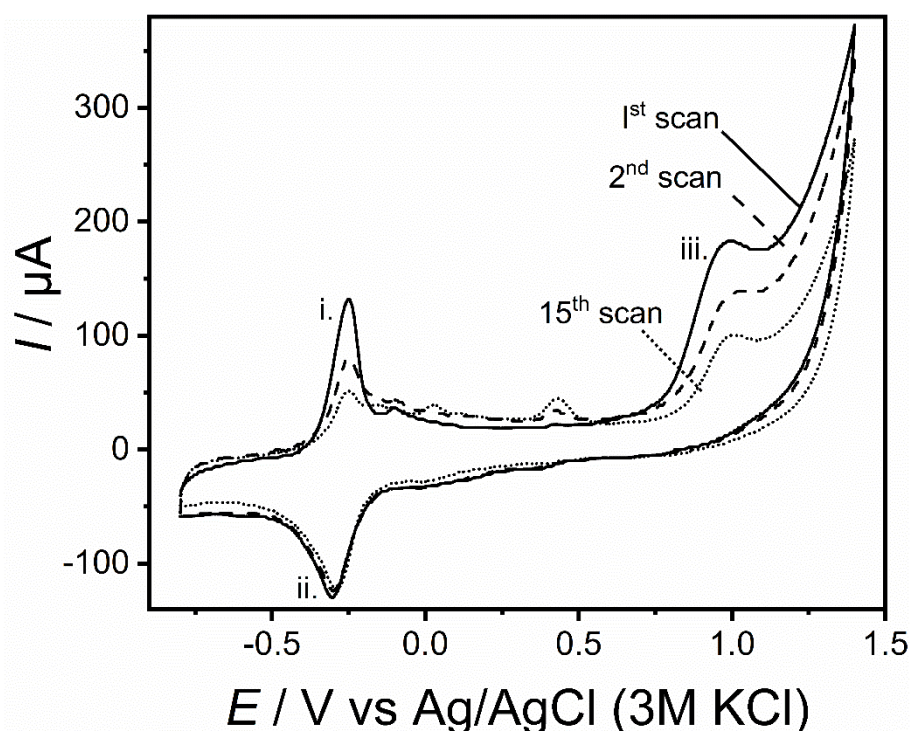


Figure 19. Cyclic voltammogram of electropolymerization of plumbagin in deaerated 0.2 mM plumbagin + 0.1 M phosphate buffer at pH 7, $v$ = 0.05 V s$^{-1}$. Reprinted from own publication[106] under license CC BY 4.0. Copyright 2023 The Authors

The topography of polyplg/plg(SiO$_2$-NH$_2$)/GC was studied with AFM. The film was homogeneous as observed in Figure 20 and root means square (RMS) roughness on a 1.00 µm × 1.00 µm area measured with an NCHV-A of 8 nm in tip radius was 4.2 nm. The strong streaks visible in the images of Figure 20 are polishing streaks on the GC substrate. The investigation by Dongmo et al. revealed that by increasing the potential cycles from 10 to 150 in the electropolymerization of plumbagin, the film thickness exhibited a range of 10 nm to 70 nm.[100]
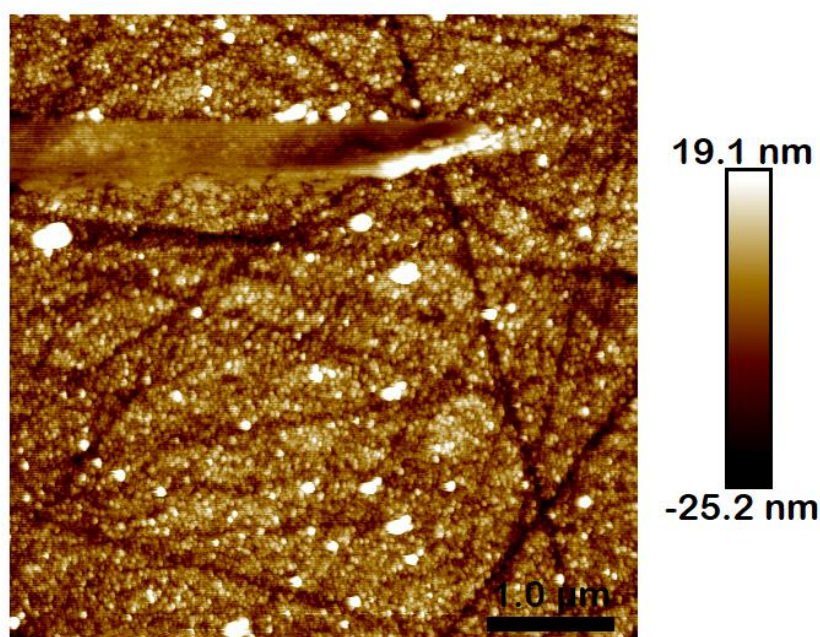


Figure 20. AFM topography image of polyplg/plg/GC recorded in intermittent mode using a NCHV-A AFM tip ($k$ = 42 N m$^{-1}$).

The mechanism of electropolymerization of plumbagin over plg(SiO$_2$-NH$_2$)/GC is similar to phenol electropolymerization. On applying high positive potential, the oxidation of phenylate anion generates phenoxyl radical. These radicals can couple with other molecules of plg, preferably at the para position to form a dimeric radical which on further oxidation forms neutral dimer by the loss of a proton. Following reactions produce oligomers leading to the formation of a film on the electrode surface[120] as shown in the mechanism in Eq.(2). This opens a way for further modifications of the plumbagin-based matrix. It is detailed in the next section 5.2.3.

(2)
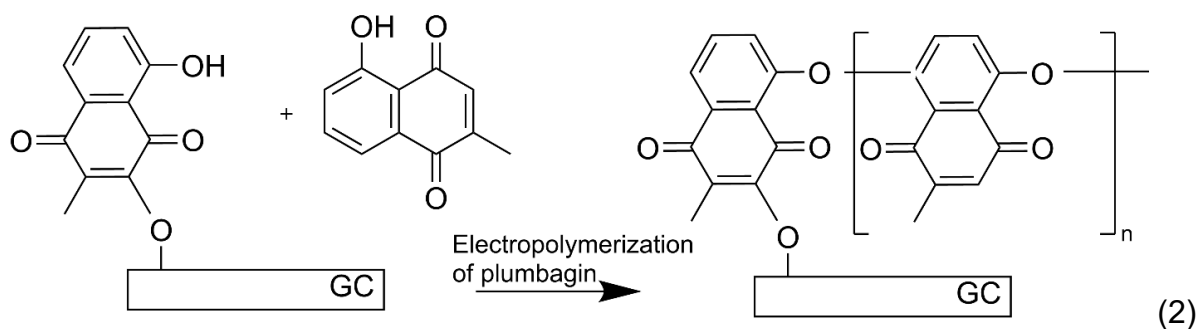
### 5.2.3. Conjugate Addition of Substituted Thiols

The selectivity of the NAIM matrix depends on many factors as discussed before. The selectivity can be tuned towards the ligand shell of the NPs either by choosing a matrix of useful functional groups which attracts the analyte NPs or by varying the ligand shell of the analyte NPs to complement the matrix. Post-functionalization of the matrix can introduce functional groups into the matrix, that can be exploited for specific interactions with analyte NPs and their ligands.



(3)
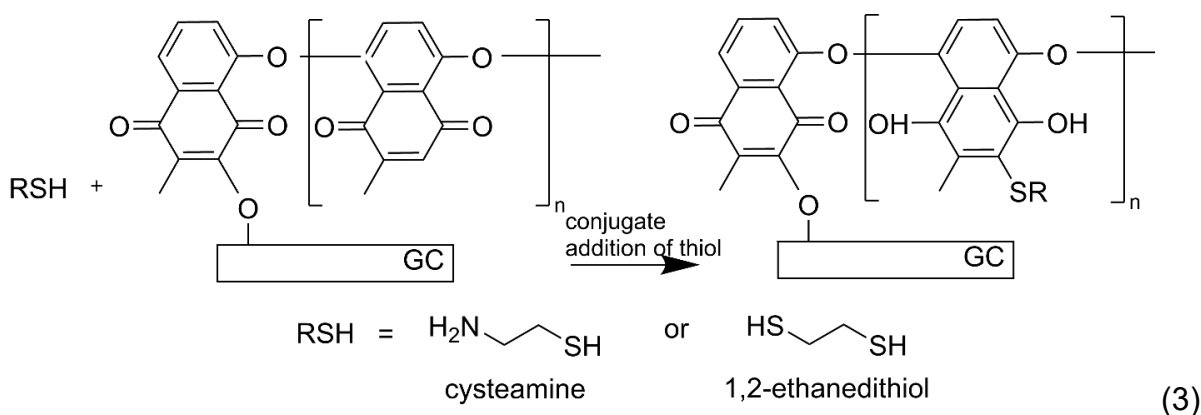
The electropolymerized polyplg layer has unsubstituted carbon atoms at the quinone ring systems available for a conjugate addition [Eq.(3)], that is used in this study for such modifications of the matrix.[99,121,122] Quinone compounds are used in several studies for the detection of thiols which can be a simple and direct alternative to supreme tools like chromatographic or electrophoretic techniques.[123–125] A highly selective determination of sulphydryl thiols was possible through the 1,4-addition of thiols to the catechol, thereby influencing the redox chemistry of quinones. The changes in the redox chemistry was assessed through cyclic voltammetry and used to

quantify the concentration of thiol.[124] Similarly, detection of homocysteine by catechol-modified GC electrode was studied by cyclic voltammetry.[125] When homocysteine attacks the carbon of catechol, a shift in the redox potential of the surface-bound quinone species was observed. Also, a decrease in the reduction current and an increase in the forward peak with the increase in the concentration of homocysteine was noticed. This is in fact considered as the influence of cysteine attack on catechol, a direct indication for the addition of thiols to quinone moiety.[125]

For the post modification of the NAIM matrix, polyplg/plg($SiO_2$-$NH_2$)/GC was used as the substrate. At this stage, the unsubstituted carbon atom on the plumbagin ring is free for further attack by nucleophiles. The carbon atom of the initial electrografted plumbagin was already involved in the electrografting process and is not available for the thiol addition. Accordingly, the electropolymerized polyplumbagin layer was subjected to conjugate addition of 1,2-ethanedithiol or cysteamine to introduce thiol- or amine-functional groups at the unsubstituted carbon atom as shown in Eq. (3).[125–127]

The substrates were covalently modified as described in section 4.6.1. A NAIM system without the covalent modification was also prepared for comparison. The sample codes are dithiol/polyplg/plg($SiO_2$-$NH_2$)/GC and cysteamine/plg($SiO_2$-$NH_2$)/GC, respectively. The chronoamperogram during the conjugate addition of thiols is shown in Figure 21a. Figure 21b shows the cyclic voltammograms at a scan rate of $v = 0.1$ Vs$^{-1}$ in plumbagin-free phosphate buffer corresponding to the oxidation and reduction of the quinone group, before and after thiol addition. A reduction in the redox activity of plumbagin after the insertion of thiols into the system can be noticed which in turn is direct evidence for the matrix modification.[118]
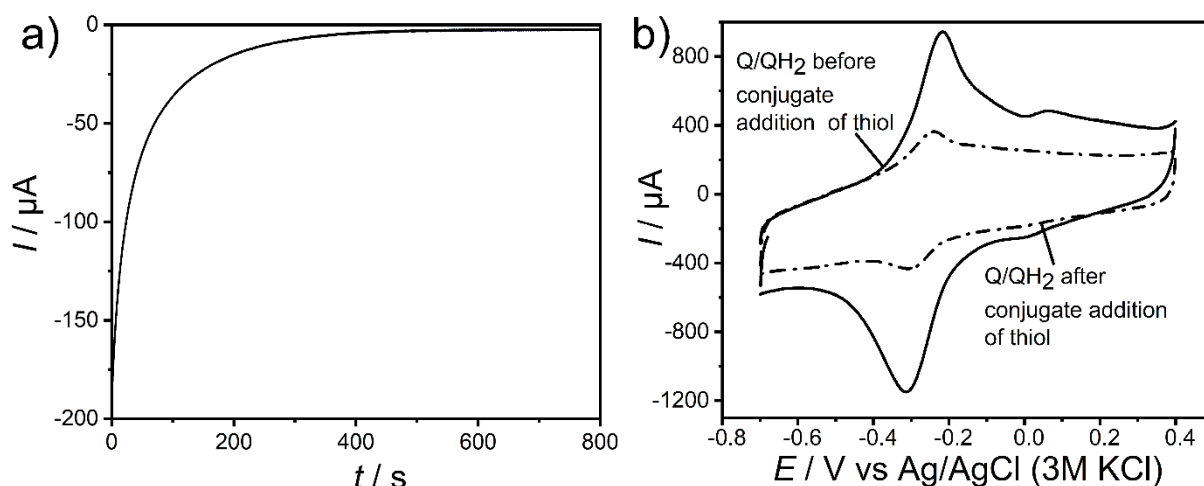
Figure 21. a) Chronoamperogram during conjugate addition of 1,2-ethanedithiol to the polyplg/plg/GC at -0.8 V vs Ag/AgNO₃; b) cyclic voltammogram of the quinone/hydroquinone redox couple in plumbagin-free phosphate buffer; 1) before and 2) after conjugate-addition of 1,2-ethanedithiol; v = 0.1 Vs⁻¹. Reprinted from own publication[106] under license CC BY 4.0. Copyright 2023 The Authors

XPS was employed to investigate the integration of functional groups into the matrix of films. Figure 22a, 22b and 22c are the N 1s and S 2p X-ray photoelectron spectra of the polymer film (without template NPs) after covalent attachment of cysteamine and 1,2-ethanedithiol. The N 1s spectra was fitted using two components at 399.8 eV and 402.4 eV; they correspond to the $NH_2$-C and protonated amine, respectively.[128,129] The S 2p spectra from cysteamine and 1,2-ethanedithiol are described by a one doublet component for each spectrum for S $2p_{3/2}$ and S $2p_{1/2}$ at 163. eV and 164.8 eV. The small signal at 168.0 eV in the cysteamine-modified sample indicates a low fraction of oxidized sulfur components.[130,131] This confirms the integration of the functional groups into the matrix.
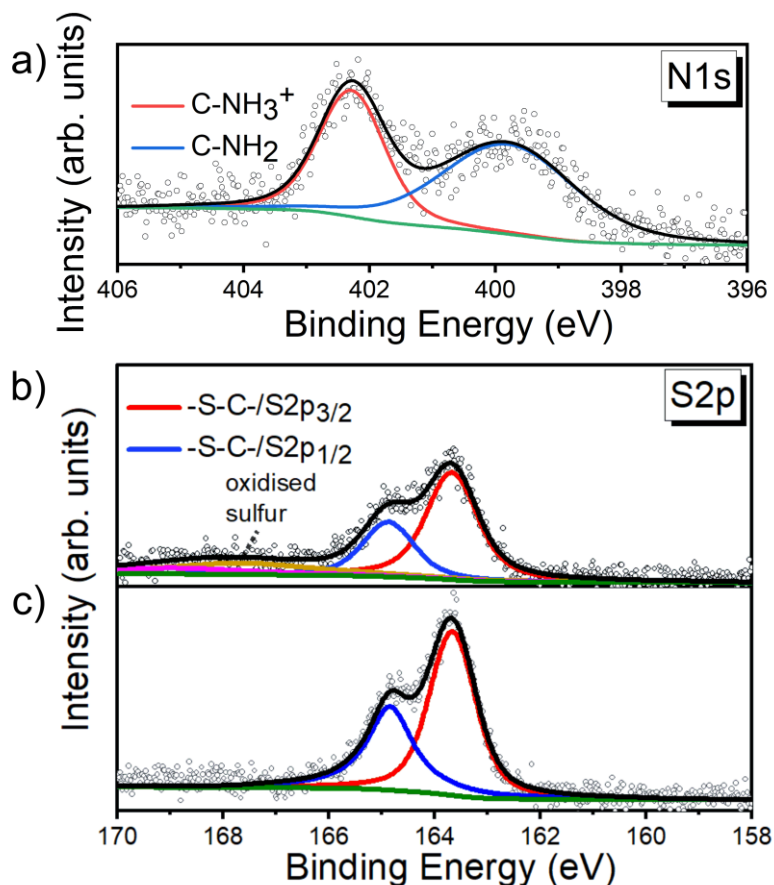
Figure 22. a) N 1s and b) S 2p spectra after conjugate addition of cysteamine and c) S 2p spectra after conjugate addition of 1,2-ethanedithiol to an electropolymerized polyplumbagin layer on plumbagin-grafted activated GC.[106] Reprinted from own publication[106] under license CC BY 4.0. Copyright 2023 The Authors

### 5.2.4. Electropolymerization of Phenol

Electropolymerization of phenol leads to the formation of self-limiting[120], thin, insulating films which are characterized as tight and compact films on metal surfaces.[132] The self-inhibiting electropolymerization of phenol was carried out at the poly-plumbagin film or after the conjugate addition of thiols to the polyplg/plg/GC substrates as shown in Eq.(4). The mechanism of phenol electropolymerization is analogous to that of plumbagin described in section 5.2.2. At positive potentials, phenoxy radicals are formed which couple with other radicals to form dimers, followed by the formation of oligomers. Polymerization ceases when the surface is completely covered by the polymerized phenol film. Then, the monomer cannot penetrate the film anymore, the current decreases to a minimum, a direct signal towards the formation of

an insulating film.[133] The electropolymerized polyphenol films finds applications in biosensors, immobilization of enzymes like glucose oxidase,[134] as coatings to prevent electrode fouling,[133] etc.
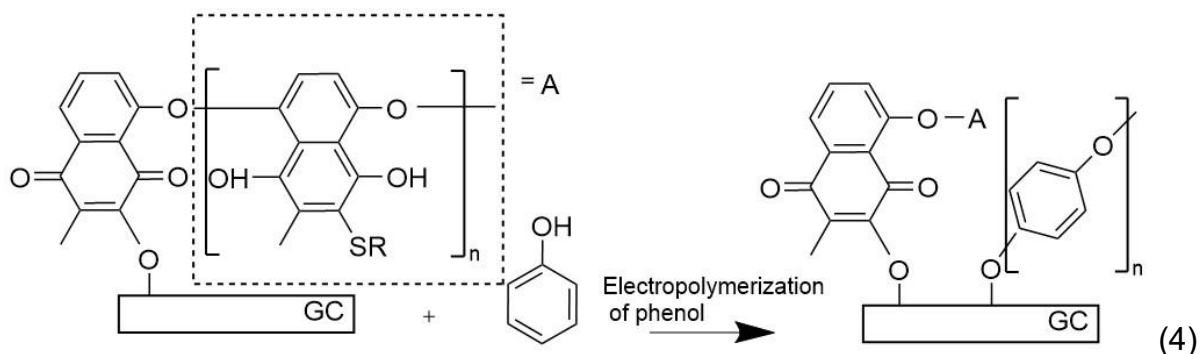


(4)

Figure 23 shows the cyclic voltammogram for electropolymerization of phenol on dithiol/polyplg/plg($SiO_2$-$NH_2$)/GC in 50 mM phenol for five potential cycles. After the prominent oxidation peak at 0.95 V in the first cycle, the anodic current decreased in all subsequent potential scans pointing towards the formation of an insulating layer. The state of this electrodes is abbreviated as pph/polyplg/plg/GC.



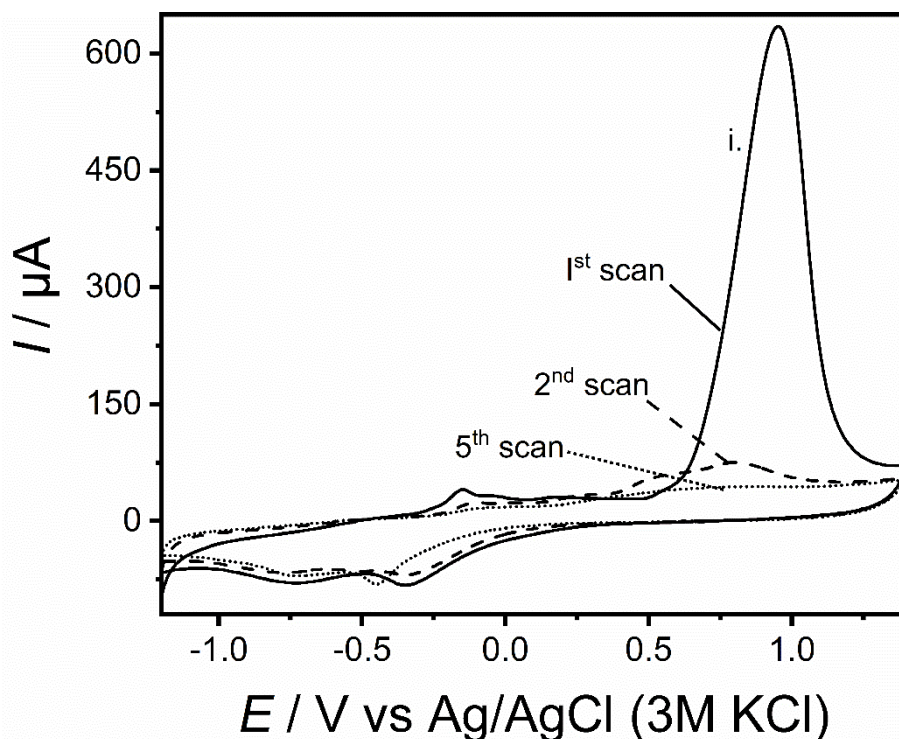Figure 23. Cyclic voltammogram of electropolymerization of phenol on dithiol/polyplg/plg($SiO_2$-$NH_2$)/GC in 50 mM phenol + 0.1 M $NaH_2PO_4$ at $v$ = 0.05 V $s^{-1}$. Reprinted from own publication[106] under license CC BY XX. Copyright 2023 The Authors

### 5.2.5  Permeability Studies of the Matrix

A matrix film with good barrier properties allows to distinguish analyte NPs in the cavity with electronic contact to the substrate electrode from those attached to the film outside the cavity. In the schematics presented in Figure 24, the differentiation between matrices lacking blocking properties (I) and those having effective barrier properties (II) is illustrated. In case I, the NPs whether specifically or non-specifically attached, are electrochemically removed in a suitable potential range, making it challenging to discern between the two types of adsorptions. In Case II, as depicted in Figure 24, the diagram illustrates a matrix featuring effective barrier properties, thereby impeding electrical contact between the surface-adsorbed NPs and the underlying GC substrate. This distinction effectively identifies both specifically and non-specifically adsorbed NPs.

The blocking property of the matrix systems at different stages of preparation (GC as polished, activated GC, polyplg/plg/GC) was studied with $[Fe(CN)_6]^{3-}$ as the redox-active probe. The voltammogram on bare GC demonstrates a quasi-reversible curve (curve 1), typical for $[Fe(CN)_6]^{3-}/[Fe(CN)_6]^{4-}$. The redox curves for $[Fe(CN)_6]^{3-}/[Fe(CN)_6]^{4-}$ were prominent on activated GC (curve 2) and polyplg/plg/GC (curve 3) indicates the permeability of the polyplumbagin film prepared according to Dongmo et al.[100] (Figure 25). To form a dense, less permeable film, self-inhibiting electropolymerization of phenol was carried out at the poly-plumbagin film or after the conjugate addition of thiols to the polyplg/plg/GC substrates. The blocking property of the film after electropolymerization of phenol was assessed through the similar method mentioned before. The matrix becomes impermeable to the used hydrophilic molecular redox probe $[Fe(CN)6]^{3-}/[Fe(CN)6]^{4-}$, proving an improved barrier property of the NAIM system. This can be observed in Figure 25, curve 4, where the redox curves corresponding to $[Fe(CN)6]^{3-} / [Fe(CN)6]^{4-}$ is missing. From the redox probe analysis, it is evident that the electropolymerization of phenol improves the blocking property of the NAIM system.
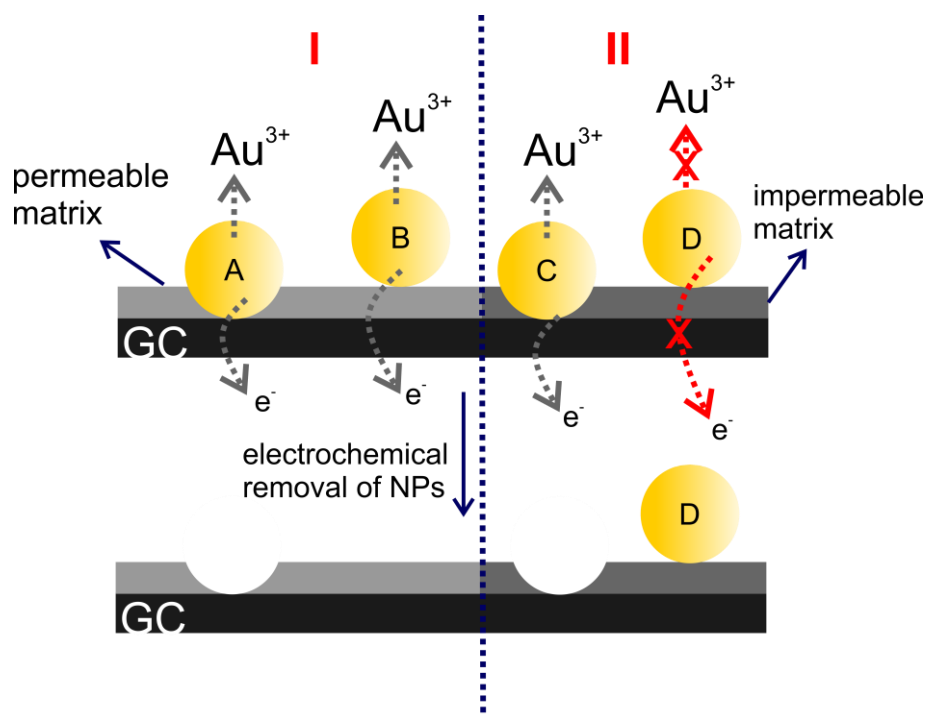
Figure 24. Schematics illustrating the contrast between matrices with effective barrier properties (II) and matrices lacking barrier properties (I).



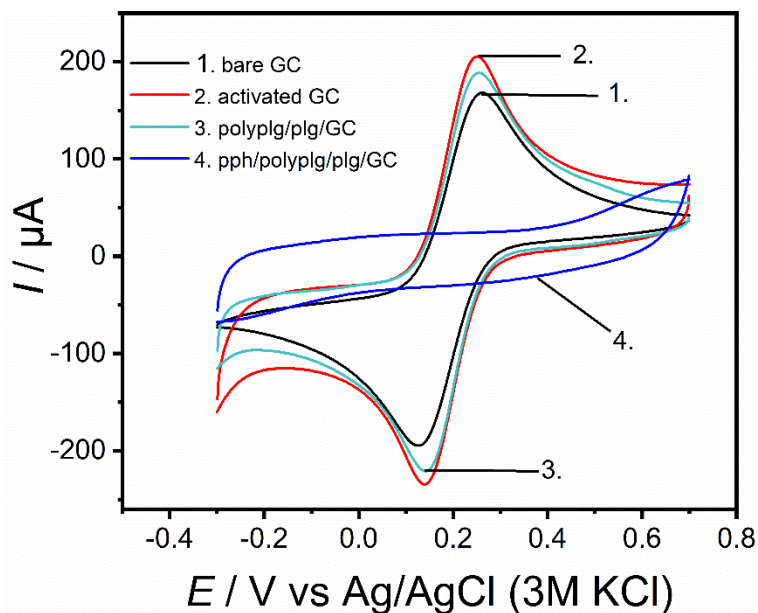Figure 25. Redox probe studies at 1) polished GC, 2) activated GC, 3) polyplg/plg/GC, and 4) pph/polyplg/plg/GC in 2 mM $K_3[Fe(CN)_6]$ + 0.1 M KCl at 0.1 $Vs^{-1}$. Reprinted from own publication[106] under license CC BY 4.0. Copyright 2023 The Author.

## 5.3 Topography and Thickness Studies of the Polyplumbagin-Based Matrix

The topography and thickness of different NAIM systems were studied with AFM. The studied films were homogeneous. The root means square (RMS) roughness were measured to be 3.8 nm, 3.5 nm, and 4.7 nm for pph/polyplg/plg/GC, pph/dithiol/polyplg/plg/GC, and pph/cysteamine/polyplg/plg/GC, respectively. The strong streaks visible in the images of Figure 26 are polishing streaks on the GC substrate that are also visible on the activated GC electrode in Figure 17a.

The thickness of the matrices was measured by scratching a 1.00 µm × 1.00 µm area using a FESPA-V2 tip in contact mode. Afterwards, the thickness was extracted from a profile of the topographic image (Appendix A (Table A:a-c)). Repeating this at different regions of the film, a film thickness ranging from 20 nm to 23 nm was measured for the films. Reminding that the overall diameter of the $SiO_2$-$NH_2$ NPs is approximately 55 nm, suggests that the nanoparticle should fit within a cavity at least half of its diameter for effective molecular recognition.
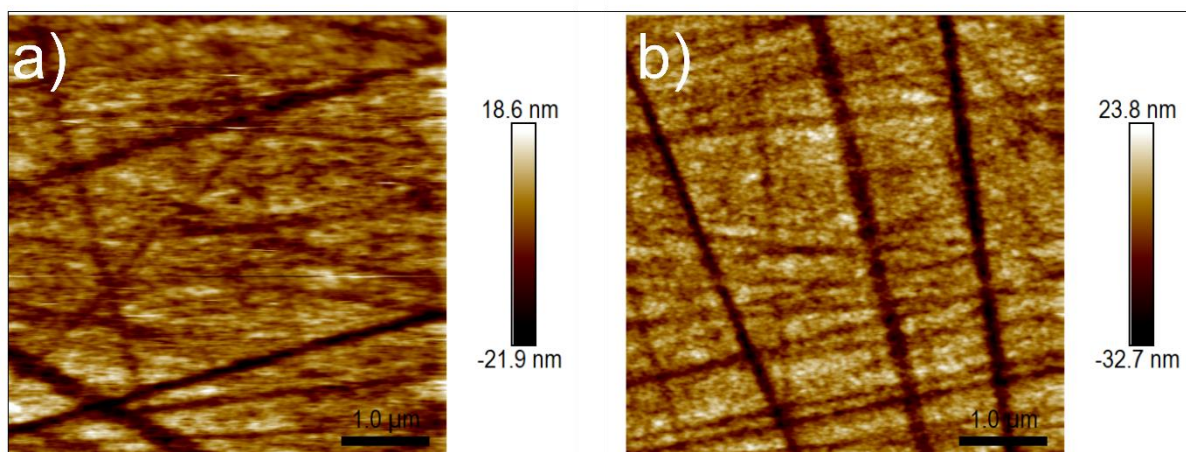


Figure 26. AFM topography image of a) pph/polyplg/plg/GC b) pph/cysteamine/polyplg/plg/GC recorded in intermittent mode using a NCHV-A AFM tip ($k$ = 42 N m$^{-1}$). Reprinted from own publication[106] under license CC BY 4.0. Copyright 2023 The Authors

## 5.4   Reuptake Studies

After the development of the NAIM system, the template $SiO_2$-$NH_2$ NPs were removed by a 3 min exposure to 5% hydrofluoric acid (HF). Caution: The corrosive and toxic nature of HF calls for extensive safety precautions and specific handling procedures.[135] The etching of $SiO_2$ by hydrofluoric acid (HF) is a well-known process in semiconductor manufacturing and microfabrication. HF is used as an etchant for $SiO_2$ because it reacts with $SiO_2$, which is the main component of most silicon wafers used in semiconductor devices and integrated circuits. The etching process follows the chemical reaction:[136]

$$SiO_2 + 6HF \longrightarrow 2H^+ + SiF_6^{2-} + 2H_2O \tag{5}$$
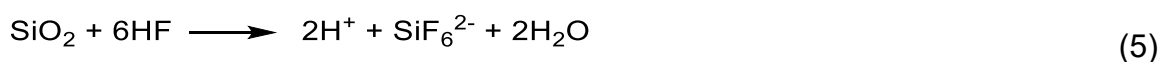
An exposure of samples with silica template NP and matrix (pph/dithiol/polyplg/plg($SiO_2$-$NH_2$)/GC, pph/cysteamine/polyplg/plg($SiO_2$-$NH_2$)/GC, pph/polyplg/plg($SiO_2$-$NH_2$)/GC to HF for 3 min removed the $SiO_2$-$NH_2$ NPs from the system leaving open cavities. SEM imaging of various regions of the NAIM system in Figure 27a and b confirmed the complete removal of template NPs. In case of insulating $SiO_2$-$NH_2$ template NPs, well-defined cavities could be identified in the SEM images in Figure 27a and b, they are marked by colored lines to extract their diameter. The size of the cavities is measured by SEM to be roughly (53 ± 3) nm using ImageJ software (Figure 27c). The value is comparable to the diameter of the used template $SiO_2$-$NH_2$ NPs. When using conducting template NPs, the film tends to overgrow the template NPs and the likelihood of obtaining a collapsed cavity or a partially closed cavity is high, resulting in an incompetent NAIM system. This finding shows that the use of insulating NPs can prevent the overgrowth over the template NPs during electrodeposition of the matrix.
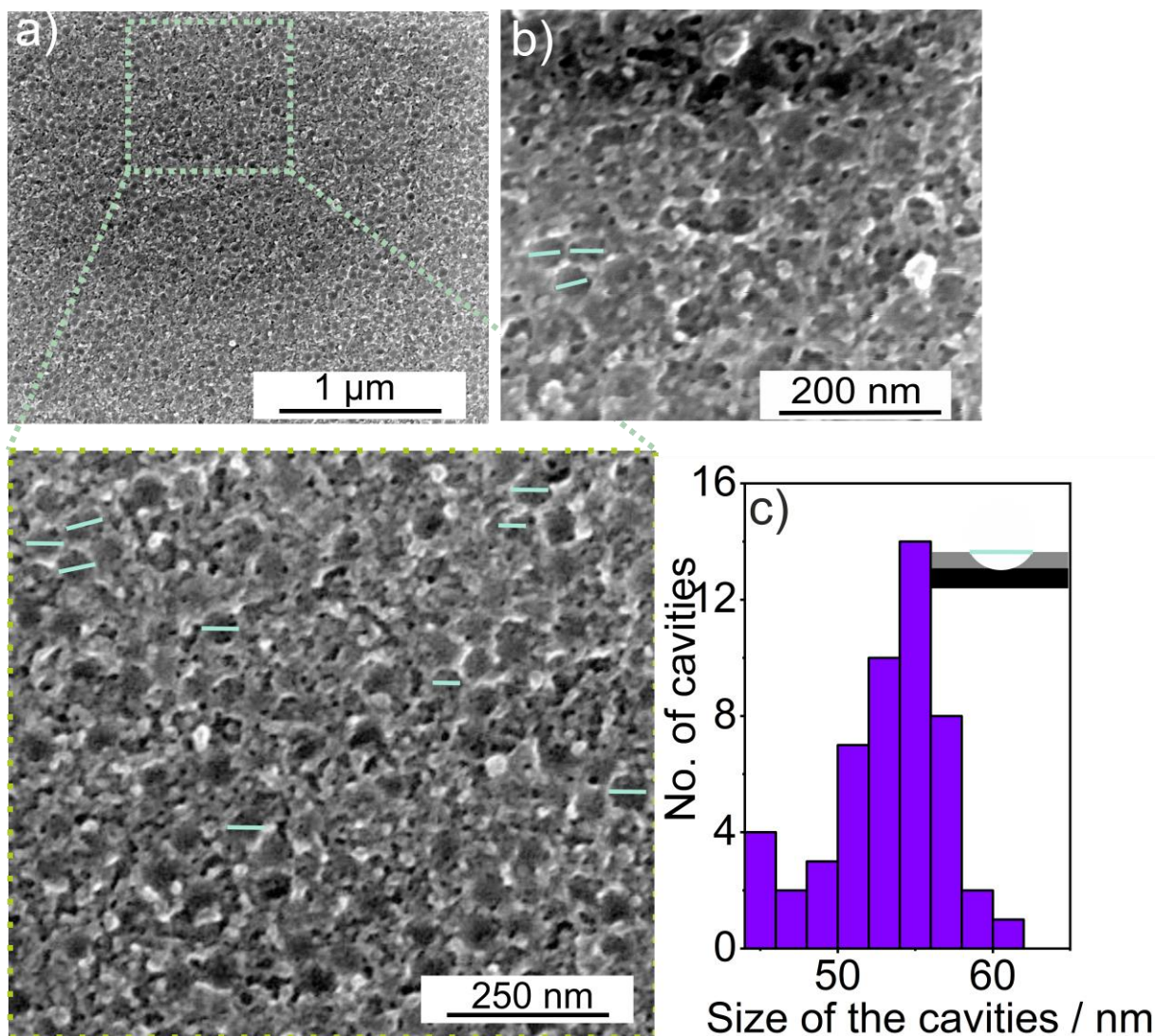
Figure 27. a) and b) SEM image of pph/polyplg/plg(°)/GC after the removal of SiO$_2$-NH$_2$ NPs, in the inset a selected area is enlarged for a better view and c) the size distribution of the cavities. The inset shows a scheme of a well-defined cavity with the marker at which the diameter was read. Reprinted from own publication[106] under license CC BY 4.0. Copyright 2023 The Authors

After rinsing with deionized water and drying in Ar stream, the cysteamine-modified matrix (pph/cysteamine/polyplg/plg(°)/GC), the 1,2-ethanedithiol-modified matrix (pph/dithiol/polyplg/plg(°)/GC), and the matrix without modification (pph/polyplg/plg(°)/GC) were immersed in an aqueous suspension of Au-Cit NPs with a diameter of approximately 55 nm for 12 h at pH 5 in order to assess the selectivity and the uptake ability. Monodisperse Au-Cit NPs were synthesized based on the kinetically controlled seeded growth approach established by Bastús et al.[96] Figure 28a shows the TEM image and the corresponding size distribution of Au-Cit NPs. The

brackets ( ) indicate the cavities formed after the removal of template $SiO_2$-$NH_2$ NPs. After 12 h, the samples were rinsed in water and dried in Ar. These samples were studied for the uptake of Au-Cit NPs.
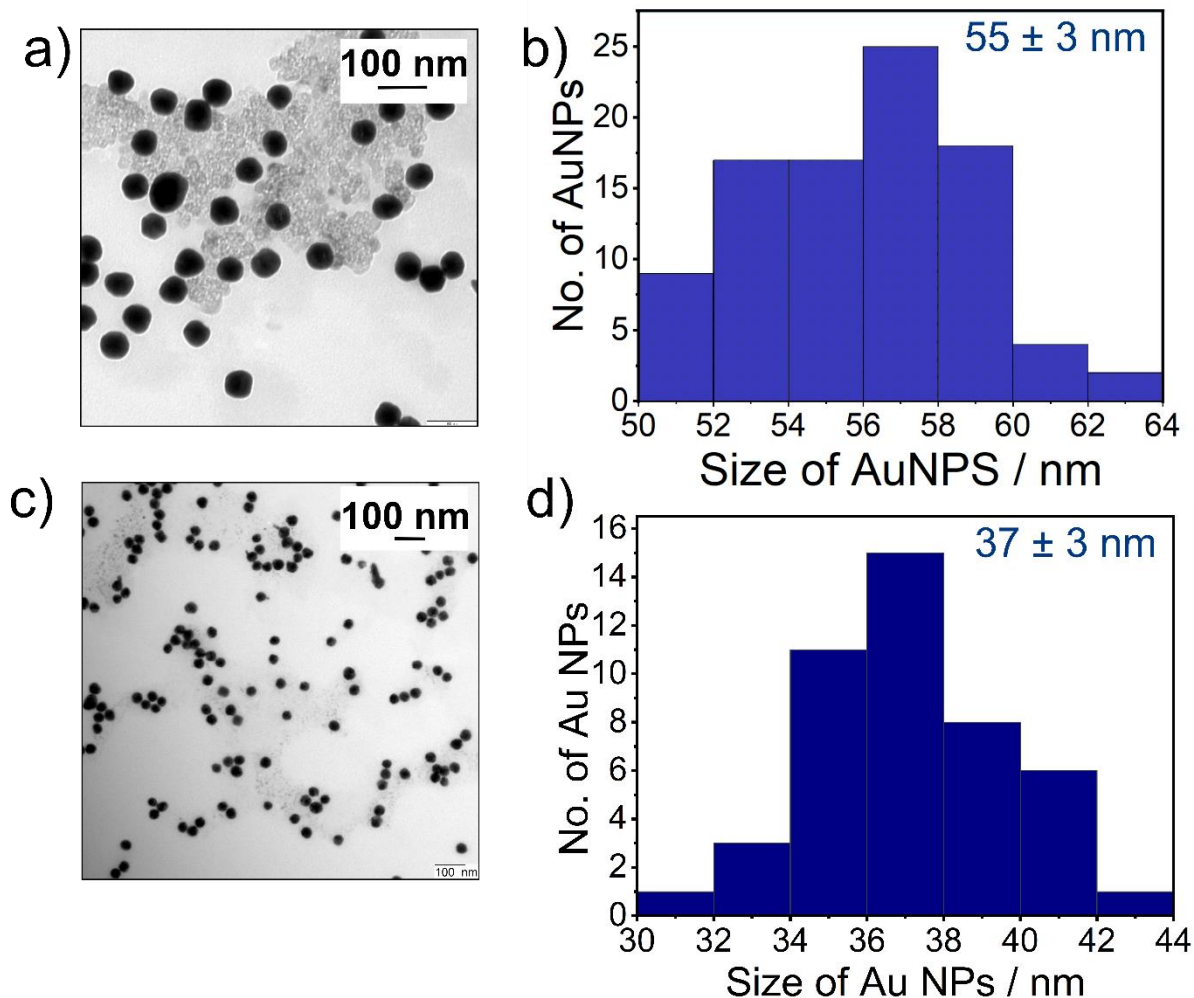


Figure 28. a) TEM image of citrate-stabilized Au-Cit NPs of size (55 ± 3) nm, b) size distribution of citrate-stabilized Au-Cit NPs of size (55 ± 3) nm, c) TEM image of citrate-stabilized Au-Cit NPs of size (37 ± 3) nm and d) size distribution of citrate-stabilized Au-Cit NPs of size (37 ± 3) nm. Reprinted from own publication[106] under license CC BY 4.0. Copyright 2023 The Authors

Electrochemical methods are one of the most suitable methods to address the analyte NPs because they can aid in distinguishing the NPs inside the cavities and the randomly attached NPs outside the cavities (Figure 24). Due to the lack of electrical contact, the non-specifically attached NPs will not dissolve or will do so at a much lower rate. Control experiments were conducted with NAIM systems prepared in the same manner but without imprinting the template NPs. These samples were exposed to Au-

Cit NPs for 12 h prior to the LSV experiments. These systems cannot specifically uptake NPs due to the absence of cavities.

SEM images after the uptake of Au-Cit NPs are shown in Figure 29. The presence of AU-Cit NPs on the surface of the samples are visible from the SEM images. To examine the Au-Cit NPs in the cavities, a cross-section of a pph/cysteamine/polyplg/plg(Au-Cit)/GC was prepared by focused ion beam (FIB) cutting at a precise location on the sample. Before, a 10 nm thick Pt layer was deposited over the sample surface to reduce the charging of the sample. An individual Au-Cit NP can be observed in Figure 30 that occupies a cavity along with few unoccupied cavities. The unoccupied cavities are indicated by arrows in Figure 16. The height of these cavities (22.1 – 22.7 nm) matches the average thickness of the film obtained from AFM imaging in (20-23 nm). The cavity width (27.3nm, 38.8 nm for the two examples analysed in Figure 30 is somewhat smaller than the diameter of the imprinted $SiO_2$-$NH_2$ NPs [(58.8 ± 2) nm] as expected for a film whose thickness does not match exactly the radius of the template NPs. We thank Dr. Vita Solovyeva for her expertise and assistance during the acquisition of SEM-FIB cross-sectional images.
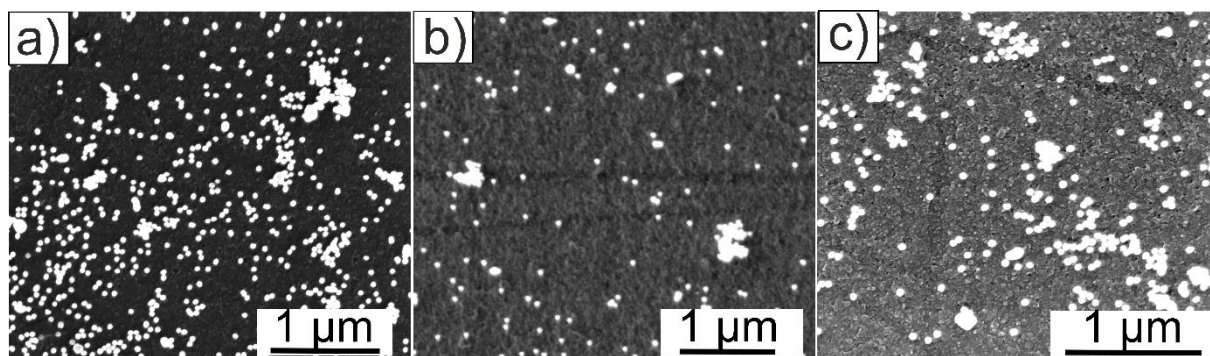


Figure 29. SEM images of a) cysteamine modified NAIM, b) 1,2-ethanedithiol modified NAIM and c) NAIM without modifications after immersion in Au-Cit NPs for 12 h.
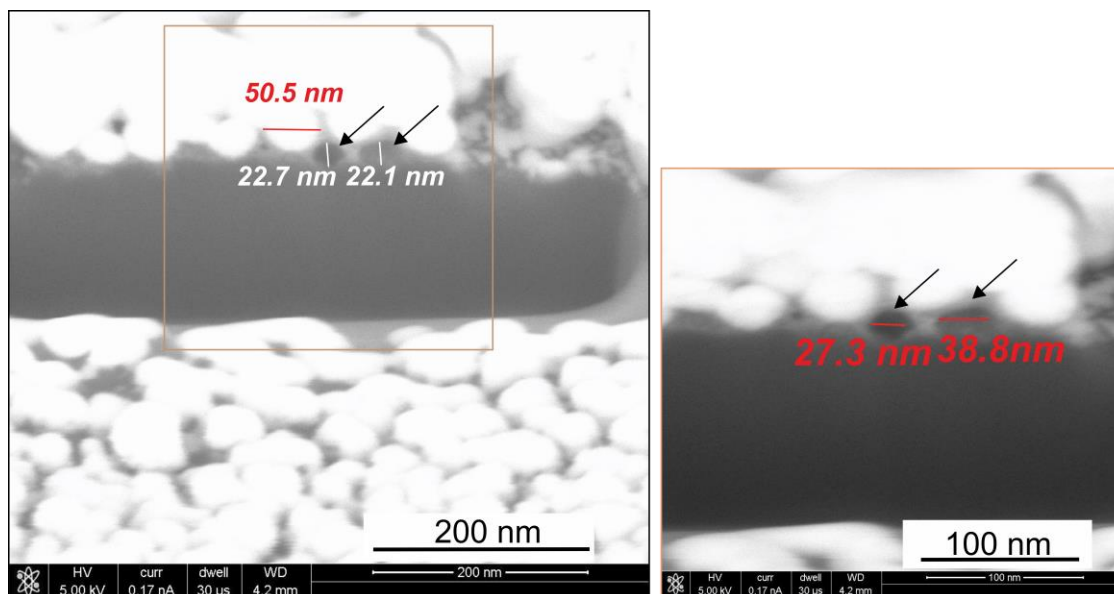
Figure 30. SEM images of FIB cross-section of a cysteamine-modified NAIM after the uptake of analyte Au-Cit NPs. Reprinted from own publication[106] under license CC BY 4.0. Copyright 2023 The Authors

After the uptake of Au-Cit analyte NPs at pH 5, the samples were subjected to LSV studies in 3 M KCl.[137] The LSV curves associated with different matrix modifications are shown in Figure 31. Control experiments with NAIM systems prepared in the same manner but without imprinting the template NPs are depicted with the dashed lines. On analyzing the LSV curves in Figure 31, a sharp peak corresponding to the oxidation of Au in chloride-containing electrolyte can be noticed at 0.9 V for a pph/cysteamine/polyplg/plg( )/GC and pph/dithiol/polyplg/plg( )/GC. For the matrix without covalent modifications (pph/polyplg/plg( )/GC), a peak can be observed at 0.86 V. A slight shift in the oxidation potential could be due to the interactions of NPs with various modifications.
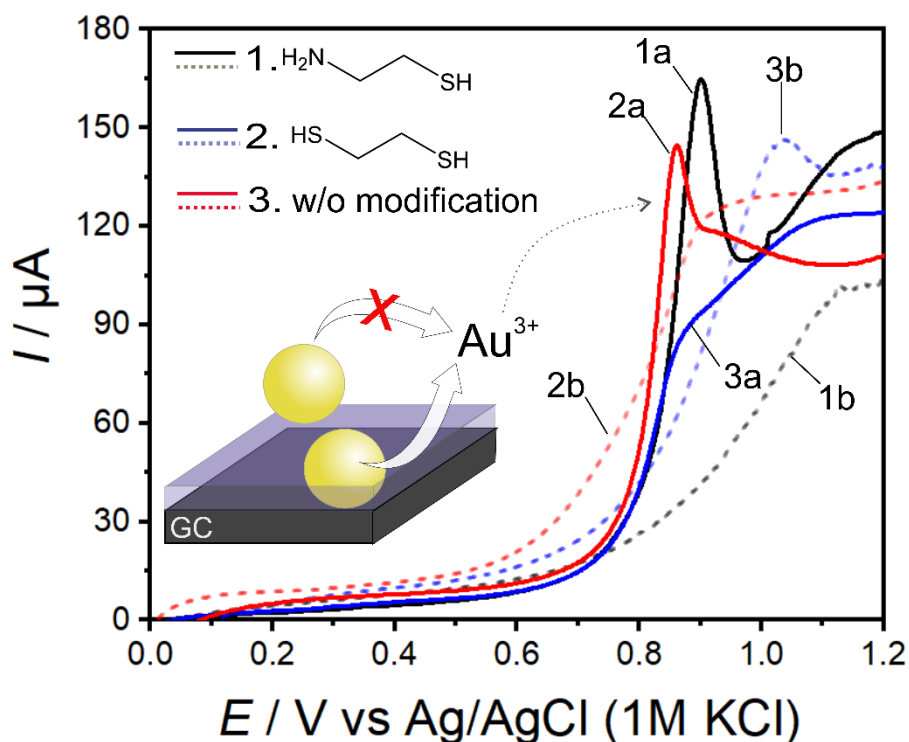
Figure 31. LSV curves in 3 M KCl at $v$ = 0.05 V s$^{-1}$ for Au-Cit NP dissolution from imprinted (1a) and non-imprinted (1b) cysteamine-modified NAIM, imprinted (2a) and non-imprinted (2b) dithiol-modified NAIM and imprinted (3a) and non-imprinted (3b) matrix without modifications after uptake of Au-Cit NPs at pH 5. Reprinted from own publication[106] under license CC BY 4.0. Copyright 2023 The Authors

The influence of matrix modifications on the recognition ability of these NAIMs is evidently reflected in the LSV scans in Figure 31. The highest uptake ability is displayed by the cysteamine-modified matrix followed by the matrix without modifications, while the 1,2-ethanedithiol-modified matrix exhibits the lowest uptake. This trend in the uptake can be explained by the presence of citrate groups on the Au NP surface[138] and the pH at which the uptake studies are performed. At pH 5, the negatively charged citrate ions interact with the positively charged protonated amines. Thus, a cysteamine-containing NAIM precedes the other NAIMs in the uptake process.[139] Apart from the aforementioned reason, the prospect of a hydrogen bond formation between the citrate oxygen and the protic hydrogens present in the plumbagin matrix can also promote the uptake process. This explains the uptake ability demonstrated by the original matrix without modification.

63

The dashed lines in Figure 31 correspond to the LSV curves associated with the non-imprinted samples. The sharp peak associated with the oxidation of Au NPs is absent in all the non-imprinted samples. However, a rising background current, specifically a shoulder between 1.0 V vs Ag/AgCl and 1.1 V vs Ag/AgCl can still be observed in the non-imprinted NAIM systems and is also present in the imprinted systems. This signal can originate either from the matrix or from the electrodissolution of non-specifically attached Au-Cit NPs at higher overpotentials. The origin of a small peak in Figure 31 in both imprinted and non-imprinted samples in the range of 0.95 V to 1.1 V vs Ag/AgCl (depending slightly on modification) was investigated. For this, the NAIM system (pph/polyplg/plg(SiO$_2$-NH$_2$)/GC) was subjected to a LSV scan in 3 M KCl before the uptake of Au-Cit NPs. The potential range is the same as used for the oxidation of Au-Cit analyte NPs. The absence of a shoulder peak in the range of 0.95 V to 1.1 V (as observed in Figure 31) in the first, second and third LSV scans in Figure 32 implies that the peak in Figure 31 is not caused by the plumbagin-based matrix. When the very same NAIM system is subjected for electrooxidation in 3 M KCl after exposure to an aqueous suspension of Au-Cit NPs, the shoulder peak 1b reappears as shown in Figure 32b as noticed during the LSV scans of almost all the samples previously exposed to Au-Cit. Therefore, this peak possibly appears due to the electrooxidation of Au-Cit NPs non-specifically adsorbed on the surface of the matrix, without any direct attachment to the GC working electrode. The absence of a similar shoulder in oxidation studies on pph/polyplg/plg(SiO$_2$-NH$_2$)/GC in Figure 32a, i.e., without exposure to Au NP suspension, proves that the occurrence of this peak cannot be linked to the matrix.

It is known that metal NPs attached to impermeable and insulating films can facilitate electron transfer reactions across the film that otherwise would not occur.[140,141] Electrodissolution of metal NPs can exhibit potential shifts in positive or negative direction depending on the interaction with the surface.[142] It is therefore assigned to the electrooxidation of non-specifically attached Au-Cit NPs. The behavior of non-imprinted samples substantiates the fact that the oxidation current obtained at 0.8 - 0.9 V from imprinted samples is associated only with the specifically adsorbed NPs which could occupy the cavities and are in direct contact with the glassy carbon electrode.
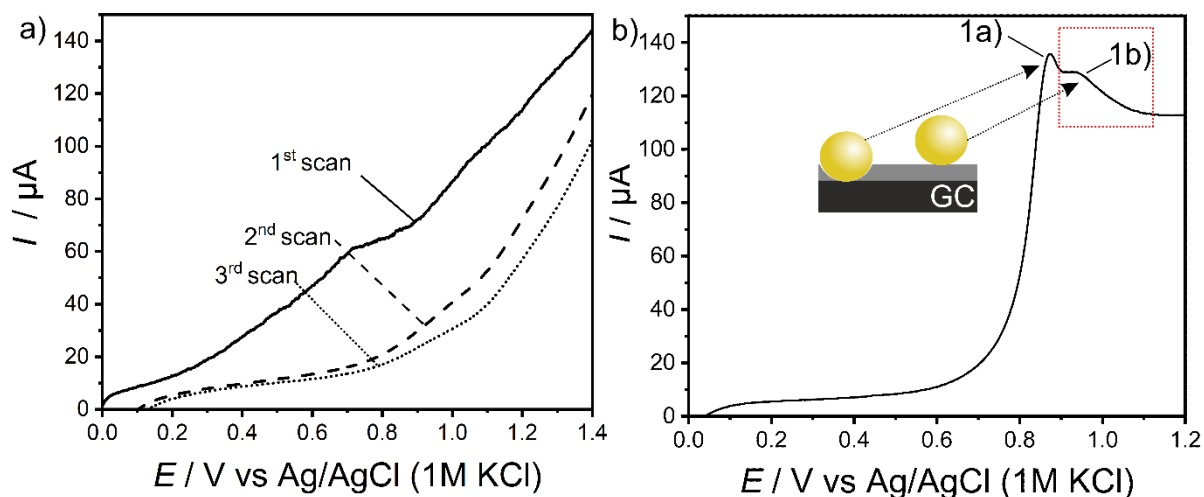
Figure 32. LSV scans obtained in 3 M KCl at $v$ = 0.05 V s$^{-1}$ from a) pph/polyplg/plg(SiO$_2$-NH$_2$)/GC before Au-Cit NP uptake and b) pph/polyplg/plg(Au-Cit)/GC after Au-Cit NP uptake. Reprinted from own publication[106] under license CC BY 4.0. Copyright 2023 The Authors

Surprisingly, the recognition ability of the matrix modified with 1,2-ethanedithiol at pH 5 is not very high as evidenced by the rather small Au oxidation peak in Figure 31, curve 2a. The well-known thiol-gold chemistry would suggest a very high uptake by this matrix. Subsequently, the impact of pH on the selectivity of a dithiol-modified matrix is studied to understand the uptake ability of the matrix. After removal of template NPs, the NAIM system is exposed to Au-Cit NP solution at pH 10. The amount of specifically retained Au NPs is quantified by LSV (Figure 33)

A distinct oxidation peak at 0.9 V vs Ag/AgCl for Au NP dissolution is clearly visible from the first LSV curve in Figure 33, curve 1. In the second scan, the peak is shifted to 0.82 V vs Ag/AgCl. Compared to the uptake by the identical NAIM at pH 5, the oxidation current is noticeably higher than in Figure 31, curve 2a. The formation of Au-S bonds between dithiol attached to the matrix and the Au NPs is likely responsible for the preferential uptake of Au-Cit NPs by a dithiol-modified matrix. The Au-S bond formation begins with the cleavage of the S-H bond of the thiol followed by the chemisorption of thiolate onto gold via a covalent bond.[143,144] The concentration of thiolate anions increases at pH 10 promoting the Au-S bond formation at the Au NPs.[145] To compare the uptake efficiency of all the NAIM systems, the total number of electrochemically oxidized Au-Cit NPs was calculated by integrating the area under the oxidation peak. A detailed calculation is given below. The result from the calculations is summarized in Table 5.

For comparison, the uptake ability of a cysteamine-modified matrix was also studied at pH 10. Figure 33, curves 3 and 4 show the first and second LSV scans corresponding to the Au-Cit NP dissolution. The sharp oxidation peak for Au-Cit NP dissolution observed with the dithiol-modified matrix (Figure 33, curve 1) is absent in case of cysteamine-modified matrix at pH 10. A rising background current can be observed in a similar potential range, where the oxidation of Au-Cit NP is expected. This also makes it difficult to distinguish the oxidation curve from the background current. In the second LSV scan, a small signal at 0.78 V vs Ag/AgCl can be assigned to the electrochemical dissolution of Au-Cit NPs, which is further diminished in the subsequent scans (not shown).
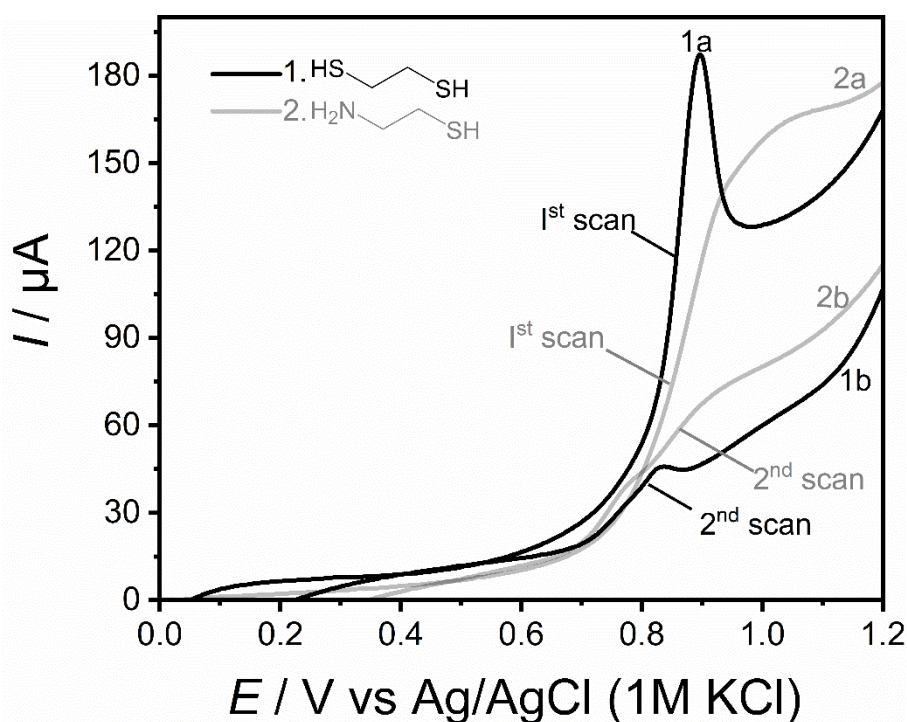


Figure 33. LSV curves in 3 M KCl at $v$=0.05 V s$^{-1}$ for a dithiol-modified NAIM (1, 2) and cysteamine-modified NAIM (3, 4) after the uptake of Au-Cit NPs at pH 10. The first and second LSV scans are shown. Reprinted from own publication[106] under license CC BY 4.0. Copyright 2023 The Authors

Among the studied NAIM systems, 1,2-ethane dithiol-modified NAIM at pH 10 shows the highest uptake efficiency, which can be explained by the enhanced gold-thiol interactions at pH 10. This is followed by cysteamine-modified NAIM at pH 5. The matrix without modifications has some uptake ability at pH 5 followed by the 1,2-ethanedithiol-modified matrix at pH 5. The lowest uptake ability is noticed for the

cysteamine-modified matrix at pH 10, owing to the weak interactions between the NPs and the matrix.

To compare the different NAIM systems regarding their uptake ability, the number of electrochemically dissolved NPs for each NAIM systems were calculated from the area under the Au-Cit NP oxidation curves (Figure 34).[41] The electrooxidation of Au-Cit NPs in 3 M KCl, where KCl acts as an electrolyte as well as a complexing agent, oxidizes the Au-Cit NPs from the NAIM systems, as shown in the following reaction:

$$Au + 4\ Cl^- = [AuCl_4]^- + 3\ e^- \hspace{3cm} (6)$$

The total number of electrochemically dissolved NPs per unit area is calculated for pph/cysteamine/polyplg/plg/( )/GC (pH 5), pph/cysteamine/polyplg/plg/( )/GC (pH 10), pph/dithiol /polyplg/plg( )GC (pH 5), pph/dithiol/polyplg/plg/( )/GC (pH 10), and pph/polyplg/plg/( )/GC (pH 5). The area under the LSV curves obtained from the Au-Cit NP oxidation was integrated and related to the scan rate $v = 0.05$ V s$^{-1}$ to yield $Q_{total}$ (Table.5)
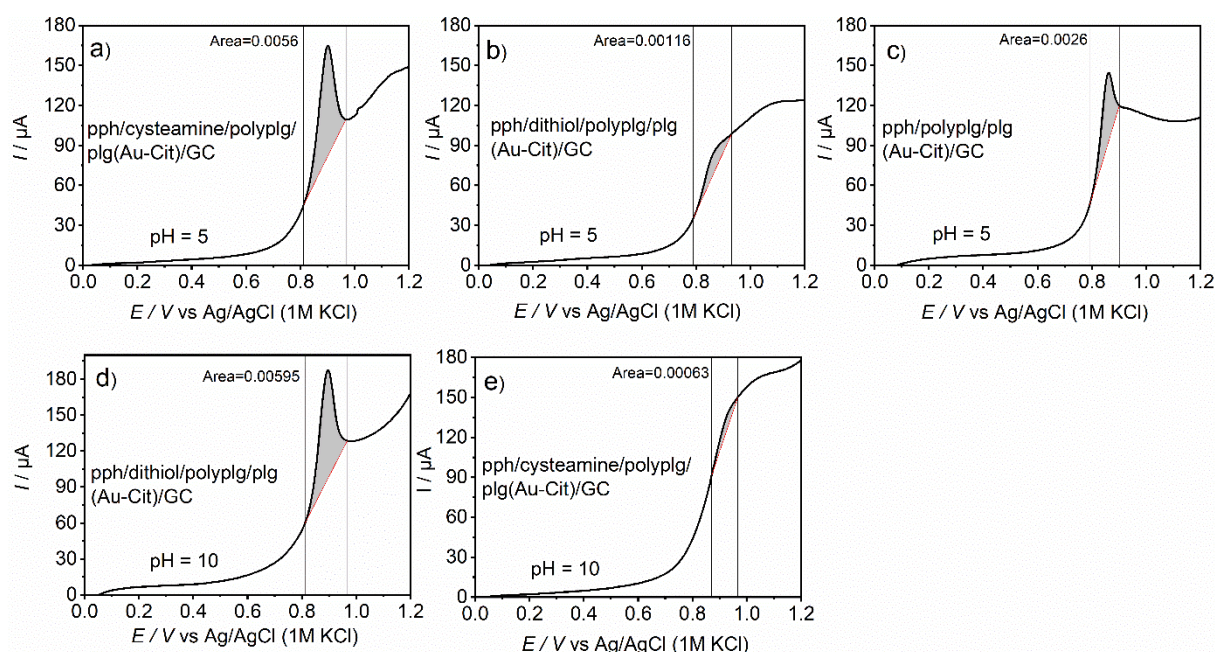


Figure 34. LSV curves for Au-Cit NP dissolution in 3 M KCl solution at $v = 0.05$ V s$^{-1}$ used for the charge calculations; a) cysteamine-modified matrix after uptake of Au-Cit NPs at pH 5; b) 1,2-ethane dithiol-modified matrix after uptake of Au-Cit NP at pH 5; c) matrix without modifications after uptake of Au-Cit NPs at pH 5; d) 1,2-ethane dithiol modified matrix after uptake of Au-Cit NPs at pH 10; e) cysteamine-modified matrix after uptake of Au-Cit NPs at pH 10. Reprinted from own publication[106] under license CC BY 4.0. Copyright 2023 The Authors

$$Q = \frac{1}{v} \int_{E_1}^{E_2} I(E)dE \tag{7}$$

The amount of charge required to remove one Au NP of diameter 55 nm is calculated as follows:

Molar mass of Au, $M_{Au}$ = 196.96 g mol$^{-1}$

Density of Au, $\rho$ = 19.32 g cm$^{-3}$

Diameter of Au NP 2 $r_{NP}$ = 55 nm (from TEM analysis)

Radius of Au NP, $r_{NP}$ = 27.5 nm

Volume of Au NP,

$$V_{Au\ NP} = \frac{4}{3}\pi r^3 = 8.7 \times 10^{-17}\ \text{cm}^3 \tag{8}$$

Mass of one individual Au NP,

$$m_{NP} = \rho\ V_{NP} = 1.7 \times 10^{-15}\ \text{g} \tag{9}$$

Amount of Au atoms in one Au NP of 55 nm diameter,

$$N_{atom} = \frac{m_{NP}}{M_{Au}} = 0.85 \times 10^{-17}\ \text{mol} \tag{10}$$

Charge required to remove one Au NP ($n$ = 3, $F$ = 96 485 As mol$^{-1}$),

$$Q_{NP} = N_{atom} \cdot n \cdot F = 2.5 \times 10^{-12}\ \text{As} \tag{11}$$

The area-related charge is obtained by $Q_{total}$ by the electrode area of $A$ = 0.5 cm$^2$ (Table 5).

$$Q/A = \frac{Q_{total}}{A} \tag{12}$$

The total number of electrochemically dissolved NPs can be calculated from

$$\Gamma_{NP} = \frac{Q/A}{Q_{NP}} \tag{13}$$

The total number of electrochemically dissolved NPs is given in the Table 5.

Table 5. Calculated charge and number of electrochemically dissolved Au NPs by integrating the area under Au NP oxidation peaks; v = 0.05 V s$^{-1}$.

| NAIM systems | Peak area [A mV] | Charge ($Q_{total}$) [As] | $Q/A$ [As·cm$^{-2}$] | $\Gamma_{NP}$ [NPs cm$^{-2}$] |
|---|---|---|---|---|
| pph/cysteamine/polyplg/plg(Au-Cit)/GC (pH 5) | 0.0056 | 1.1 × 10$^{-4}$ | 2.2 × 10$^{-4}$ | 9.1 × 10$^7$ |
| pph/cysteamine/polyplg/plg(Au-Cit)/GC (pH 10) | 0.00063 | 1.3 × 10$^{-5}$ | 2.5 × 10$^{-5}$ | 1.0 × 10$^7$ |
| pph/dithiol/polyplg/plg(Au-Cit)/GC (pH 5), | 0.00116 | 2.3 × 10$^{-5}$ | 4.6 × 10$^{-5}$ | 1.9 × 10$^7$ |
| pph/dithiol/polyplg/plg(Au-Cit)/GC (pH 10) | 0.00595 | 1.2 × 10$^{-4}$ | 2.4 × 10$^{-4}$ | 9.6 × 10$^7$ |
| pph/polyplg/plg(Au-Cit)/GC (pH 5) | 0.0026 | 5.2 × 10$^{-5}$ | 1.1 × 10$^{-4}$ | 4.2× 10$^7$ |

The SiO$_2$-NH$_2$ NPs were manually identified and counted to be 156 NPs from a 1 μm × 1 μm area of a SEM image. This translates to a particle density of 1.56 × 10$^{10}$ NPs cm$^2$. Assuming all the template NPs on removal lead to the formation of well-defined cavities which allows electrical contact to the underlying glassy carbon substrate, the estimated density of the electrochemically dissolved NPs can be related to the estimated density of cavities. The uptake efficiency of each NAIM systems can be calculated based on this assumption.

The estimated number of electrochemically dissolved NPs are given in the Table5, ranging from 1 to 9.1 × 10$^7$ NP cm$^{-2}$. The uptake efficiency is calculated for each NAIM system and provided in the Table 6. This is only a small fraction. At present, the exact reasons are not clear. However, it seems that only a perfect fit of the NP at the bottom of a cavity enables their electrochemical detection, as shown in the schematics in Figure 36. In contrast attachments to the side wall of a cavity does not lead to a signal generation as it has been observed before.[41]

To study the size selectivity of the NAIM system, smaller analyte NPs were synthesized according to Bastús et al.[96] The synthesized Au-Cit NPs were analyzed using TEM. Figure 28b shows the spherical structure of the Au-Cit NPs of size (37 ± 3) nm. To illustrate the size-selective recognition of the NAIM matrices, the Au-Cit NPs with a diameter of (53±3) nm were replaced by Au-Cit NPs with smaller diameter of (37±3) nm.

Table 6. Calculated uptake efficiency of different NAIM systems

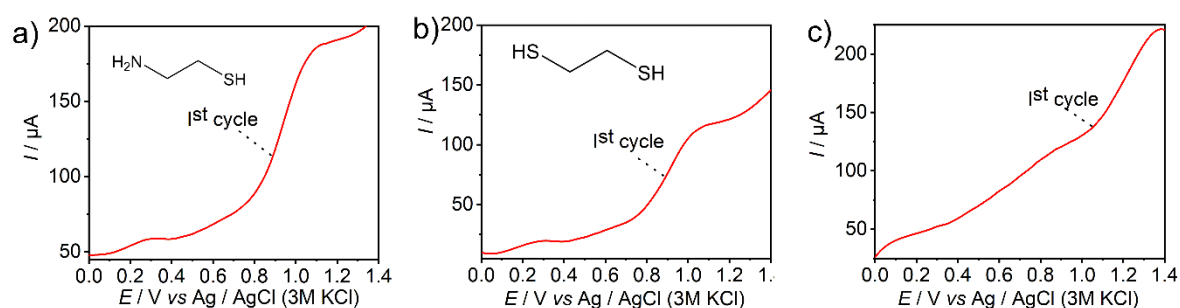| NAIM systems | Uptake efficiency |
|---|---|
| pph/cysteamine/polyplg/plg(Au-Cit)/GC (pH 5) | $5.8 \times 10^{-3}$ |
| pph/cysteamine/polyplg/plg(Au-Cit)/GC (pH 10) | $6.4 \times 10^{-4}$ |
| pph/dithiol/polyplg/plg(Au-Cit)/GC (pH 5) | $1.2 \times 10^{-3}$ |
| pph/dithiol/polyplg/plg(Au-Cit)/GC (pH 10) | $6.2 \times 10^{-3}$ |
| pph/polyplg/plg(Au-Cit)/GC (pH 5) | $2.7 \times 10^{-3}$ |



Figure 35. LSV curves in 3 M KCl solution at $v$ = 0.05 V s$^{-1}$ for the oxidation of Au-Cit NPs (35 ± 3) nm in diameter at a) cysteamine-modified b) 1,2-ethane-dithiol-modified and c) matrix without modifications having cavities formed by SiO$_2$-NH$_2$ template NPs with (58 ± 3) nm, uptake at pH 5. Reprinted from own publication[106] under license CC BY 4.0. Copyright 2023 The Authors

The uptake experiment is repeated with all three NAIM systems at pH 5. The Au-Cit analyte NPs for this test were (37 ± 3) nm in diameter and, thus, is much smaller than the template SiO$_2$-NH$_2$ NPs. The NAIM system with covalent modification by cysteamine and dithiol as well as the matrix without modifications were exposed to Au-Cit NPs (37 ± 3) nm in diameter at pH 5 for 12 h and analysed for the uptake ability. The LSV curves for the Au-Cit NP oxidation are shown in Figure 35. The curves do not show the sharp peak at 0.9 V vs Ag/AgCl typical for the oxidation of Au-Cit NPs in

cavities. This implies that those NAIM system cannot selectively recognize the smaller analyte NPs. A plausible explanation could be that the NPs are non-specifically adsorbed to the matrix surface due to the workable interactions explained before and fail to occupy the bottom of the cavities as shown in Figure 36. It could be also possible that NPs tend to attach to the side walls of the cavities, as observed in the previously studied NAIM systems,[41,146] without any contact to the GC electrode (Figure 36a and c). A broad peak between 1.0 V and 1.1 V vs Ag/AgCl can be observed in the LSV scans. As explained in the context of Figure 31, this is probably due to the oxidation of these non-specifically attached Au-Cit NPs. The incapacity in recognizing smaller analyte NPs can corroborate the size-selective recognition ability of these NAIM systems.
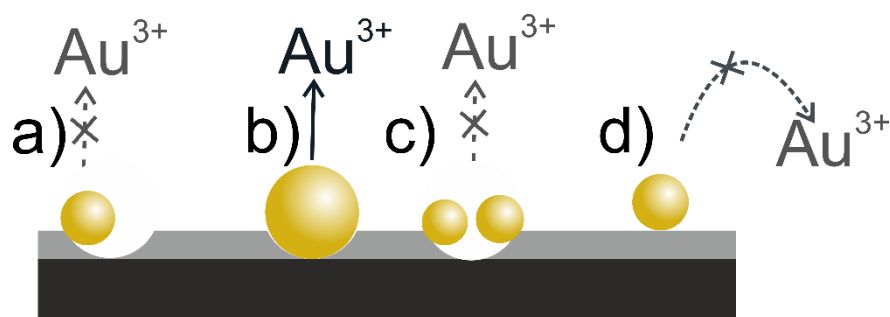


Figure 36. Schematics showing the size selectivity of the NAIM system. a) smaller Au-Cit analyte NPs attached to the sidewalls of the cavities; b) Au-Cit NPs occupying the cavities of matching size; c) multiple smaller Au-Cit NPs occupying larger cavities and d) non-specifically adsorbed Au-Cit NPs. Reprinted from own publication[106] under license CC BY 4.0. Copyright 2023 The Authors

Overall, three different NAIM systems are designed for studying the influence of matrix modifications on NAIM selectivity. The possibility for post modification of the plumbagin-based matrix on an activated glassy carbon substrate gives way for the utilization of different functional groups for the recognition process between the NAIM and the ligand shell of the analyte NPs. This advantage is demonstrated by covalent modification of polyplumbagin matrices with cysteamine or 1,2-ethanedithiol. The thiol moiety is an excellent nucleophile for conjugate addition to the quinone rings within the polyplumbagin layer. The matrix modified by cysteamine shows the highest uptake at pH 5 due to the interactions between protonated amino groups of cysteamine and

citrate groups on Au-Cit NPs while the dithiol-modified matrix shows the highest uptake at pH 10.

The impact of pH on the recognition ability is remarkable. At pH 10, the dithiol-modified matrix shows five times higher uptake efficiency than at pH 5. This is linked to the formation of more thiolate anions in alkaline solution, leading to an increased interaction with Au-Cit NPs. Due to the chemistry of the matrix as well as the introduced functional groups, the Au-Cit NPs can establish different interactions like electrostatic, hydrogen bonding or covalent bonding with the matrix. Therefore, the covalent matrix modifications have a remarkable effect on the recognition ability of the NAIM systems.

Along with the modifications, the size matching of the analyte and template NPs has a profound impact on the selectivity of the NAIM. The analyte NPs and template NPs should be in the same size range for the NAIM system to exhibit high uptake efficiency. These studies can be diversified by varying size, shape and type of the template NPs and different matrix modifications to adapt the system for different analyte NPs.

# 6 NAIM Systems with Polystyrene Template NPs

To expand the variety of template and analyte NPs available for orthogonal removal methods, NAIM systems with PS NPs were tested. Polystyrene is generally considered biocompatible, making it suitable for biomedical and technological applications.[147] The hydrophobic core of polystyrene NPs (PS NPs) allows their surface modification. It makes them valuable tools for investigating cellular uptake, protein adsorption, and other interactions at the nanoscale.[148]

PS NPs are selected as the template NPs as it offers several advantages. PS NPs are available in different sizes and with various surface modifications. This work used sulfate-modified PS NPs to study the NAIM systems. By controlling the synthesis conditions, the size, shape, and surface properties of PS NPs can be tailored to specific applications. These NPs can be developed with different surface modifications like sulfate, amine, aldehyde, etc. This tunability allows to optimize the NPs for their intended purposes.[149,150] The changes on the surface of the NPs make it easier to assemble the NPs onto the relevant substrate, which is the initial step in the development of the NAIM system. PS NPs are stable and can resist degradation, making them suitable for long-term storage and applications where prolonged stability is essential.[149]

The hydrophobic PS NPs, with their non-polar hydrocarbon chains, result in limited solubility in water-based solutions due to their poor interaction with polar water molecules. However, the solubility of PS NPs can be influenced by several factors, including the size and surface functionalization of the NPs and the type of solvent used.[151] In general, PS NPs exhibit better solubility in non-polar and organic solvents. When placed in organic solvents, the hydrophobic polystyrene chains can interact more favorably with the solvent molecules, resulting in better solubility. Typical organic solvents used for dissolving PS NPs include toluene, chloroform, xylene, and tetrahydrofuran (THF), among others. The solubility of PS NPs in various non-polar solvents is attractive to remove such NP from a NAIM system, for which they may be used as template NPs.

## 6.1 Attachment of Sulfate-Modified Polystyrene NPs onto ITO

The preliminary step in developing the NAIM system is to modify the substrate surface with template NPs. The ITO substrate was cleaned, as explained in Chapter 4 and dried in the Ar stream. The template PS NPs is negatively charged due to the sulfate groups on the surface of the NPs. As discussed in the previous chapter, we relied on the self-assembling approach to obtain good coverage of PS NPs.

The initial step involves adsorbing a positively charged primer layer, poly(diallyldimethylammonium chloride) (PDDA), chemisorbed on the surface of cleaned ITO substrate (PDDA/ITO). Figure 37 shows the high-resolution N 1s XP spectra of PDDA-modified ITO with a peak at 403.1 eV corresponding to the presence of quaternary amines ($N^+$). In contrast, a peak at 400.1 eV indicates the presence of tertiary amines ($N^0$). However, in the chemical structure of PDDA, (structure of PDDA shown in the inset of Figure 37) tertiary amines are absent. Pei et al.[152] demonstrated the occurrence of tertiary amine in the structure of PDDA, however, the underlying reason for this occurrence remains unknown. The PDDA layer on ITO attracts negatively charged sulfate-modified polystyrene NPs (PS NPs) of size approximately 60 nm diameter. XPS confirms the presence of a primer layer.
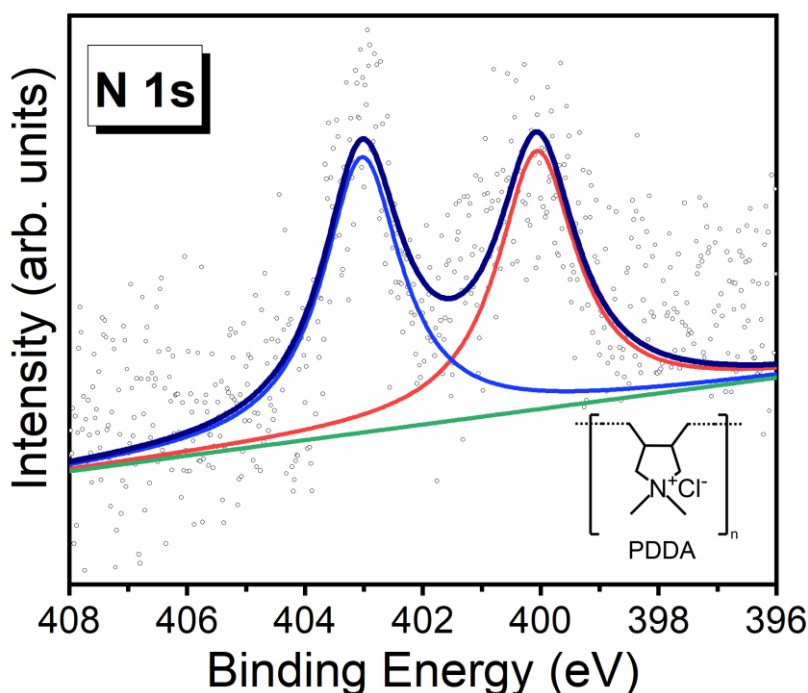


Figure 37. N 1s spectra of PDDA-modified ITO formed after the modification of ITO surface with a primer layer of PDDA. The inset shows the chemical structure of PDDA.

The distribution of PS NPs on the surface of ITO depends on the quality and coverage of the initial PDDA layer. A 2 h immersion of PDDA/ITO in a colloidal solution of PS NPs is sufficient for attaining a surface covered uniformly with PS NPs. Figure 38a shows the TEM and corresponding size distribution of the template PS NPs. image The SEM and AFM images after the adsorption of PS NPs are shown in Figures 38b and 38c. We denote the ITO surface decorated with PS NPs as (PS)PDDA/ITO for brevity. SEM and AFM images show the well-assembled PS NPs on the surface of PDDA/ITO. Figure 38d is the phase image of (PS)PDDA/ITO, which shows the presence of NPs. A dark region in the center of a few NPs with a brighter outline can be observed in Figure 38b, which is probably due to the charging effect in observing a non-conductive sample in SEM.
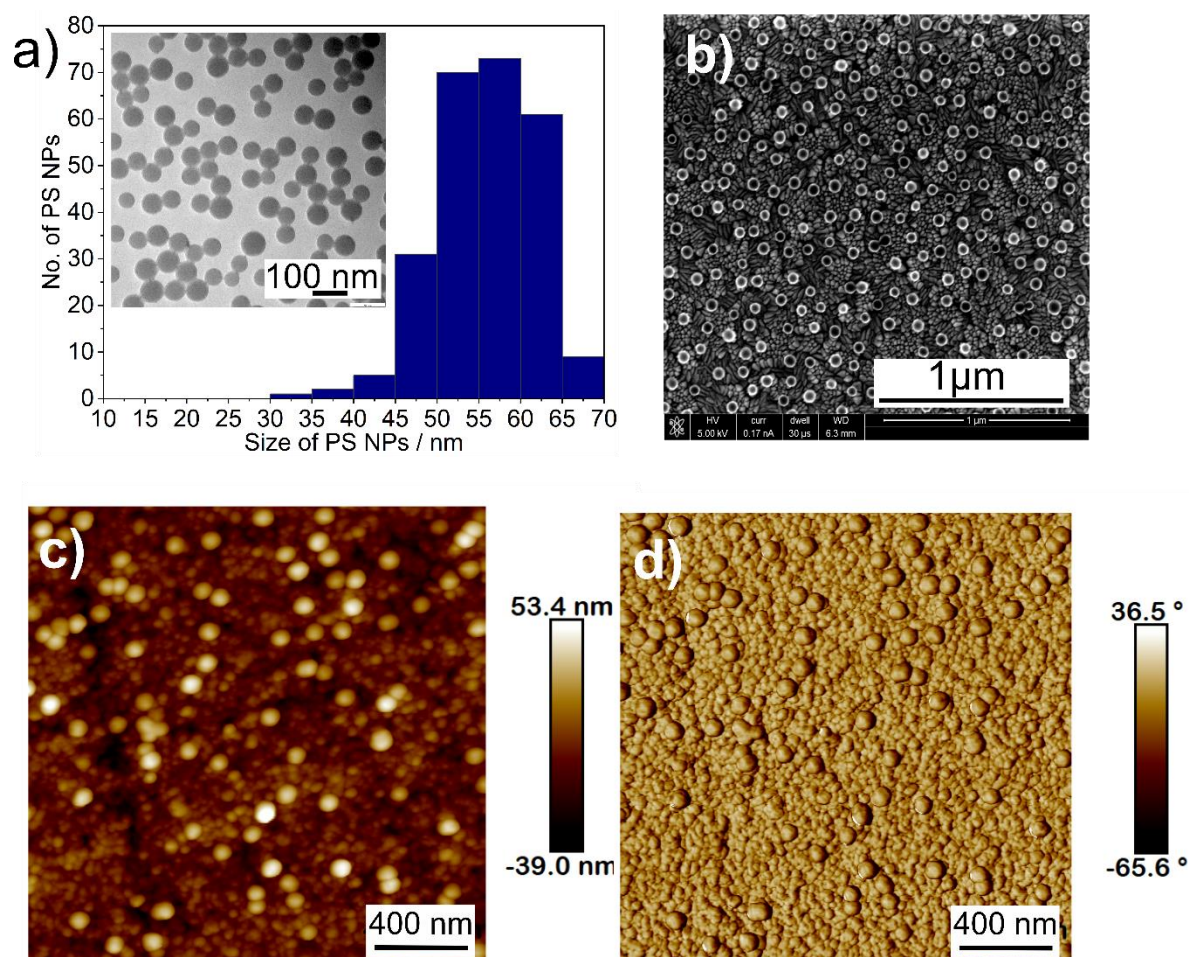


Figure 38. a) Size distribution of commercially bought sulfate-modified PS NPs. TEM image of the PS NPs is shown in the inset, b) SEM image of (PS)PDDA/ITO, c) AFM topography image, and d) AFM phase image of (PS)PDDA/ITO.

## 6.2 Formation of Insulating Polymer Films over PS/PDDA/ITO

The formation of thin polymer films via electrochemical methods is a promising route toward developing functional surfaces. The properties of the consequential film coatings depend on the electrolytes, deposition conditions, precursors, etc.[153] Dependence on electrochemical processes for thin film deposition results in homogeneous, uniformly thick films even on rough substrates.[154] The process can be monitored in real time and can be controlled in case of necessity.[155]

### 6.2.1 Polydopamine-Based NAIM

Dopamine was used to create a polymer matrix polydopamine (PDA). The Lewis structure of dopamine is shown in Figure 40. PDA offers advantages as NAIM material because it is stable and can be deposited on various substrate materials with tunable film thickness.[156] It also contains functional groups like amine, imine, and catechol that can be used in the recognition process.[157–159] PDA is a synthetic polymer that mimics the structure of the naturally occurring pigment dopamine. The exceptional adhesive nature of PDA is one of its remarkable advantages. A facile approach was introduced by Lee et al.[157] to form a thin and versatile coating of polydopamine on various surfaces. The method is simple and easy to implement, but the process makes it difficult to obtain homogeneous films. The schematic in Figure 39 shows the different steps involved in developing the NAIM system.



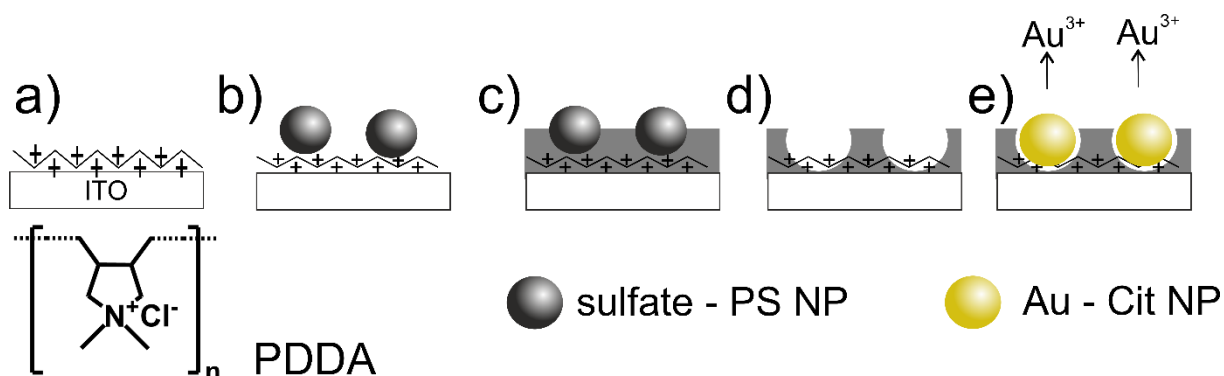Figure 39. Illustration of electropolymerized NAIM with insulating PS template NPs: a) PDDA-modified ITO substrate to promote adhesion of sulfate-PS NPs b) adhesion of sulfate-PS NPs to PDDA-modified ITO; c) electropolymerization of the polydopamine matrix, d) cavities formed after the removal of the insulating template NPs by dissolution; e) uptake of Au-Cit analyte NPs followed by the electrodissolution of Au-Cit analyte NPs.

The stability and reproducibility of the film are substantial for the NAIM system. Studies have shown that the electrochemical deposition of PDA leads to stable and homogeneous films.[158] Electropolymerization of dopamine is possible as it can undergo electrochemical oxidation and subsequent polymerization to form a PDA film. This process offers precise control over film properties and is versatile, making it valuable in various fields, including materials science, biomaterials, and sensor development. The electropolymerization of dopamine follows the ECE mechanism (Figure 40).[160,161] Initially, an electron transfer (E) by exchanging two protons and two electrons. This step is followed by a chemical step (C) of cyclization reaction via conjugate addition, as shown in Figure 40. This step leads to the formation of leucodopaminochrome. This is later oxidized to dopaminochrome, forming the polydopamine film.
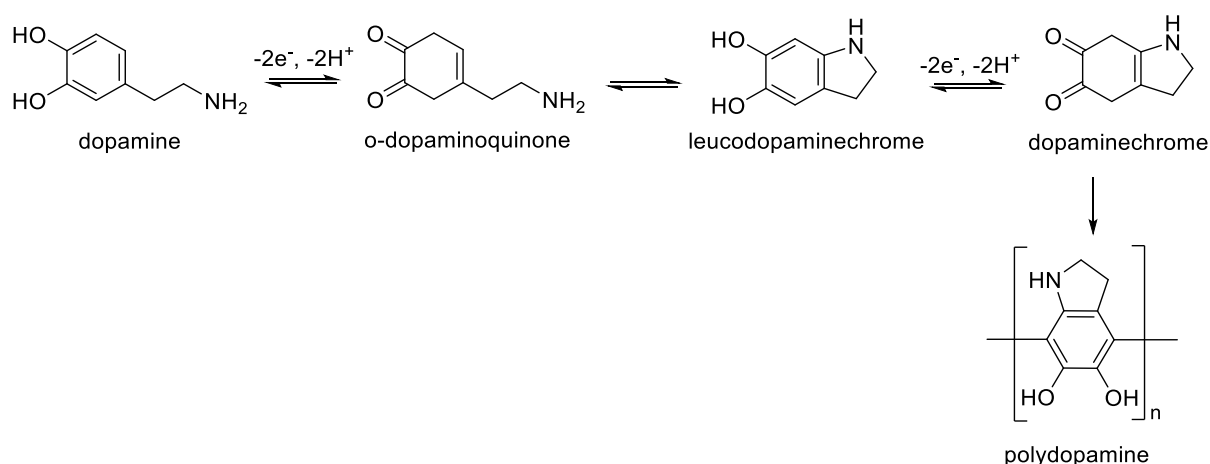


Figure 40. Mechanism of electropolymerization of dopamine.

PDA electropolymerization was performed on a (PS)PDDA/ITO substrate in a phosphate buffer solution with a pH of 7.4, as described in section 4.6.2. Figure 41a shows the cyclic voltammogram of polydopamine electropolymerization from a 10 mM dopamine solution in deoxygenated 10 mM phosphate buffer of pH 7.4 on ITO decorated with PS NPs. The formation of insulating PDA film is evident from the decrease in the cathodic and anodic current with the number of potential cycles. The film thickness can be controlled by the number of potential cycles during the electropolymerization.[161] The (PS)PDDA/ITO surface after polydopamine electropolymerization is studied by SEM. The PS NPs are not disturbed during the

77

process of polydopamine electropolymerization, which can be confirmed by the SEM image in Figure 41b. The change in the contrast of PS NPs before and after electropolymerization is maybe due to the electrodeposition of a partial layer of polydopamine over the PS NPs, explained later in the chapter.
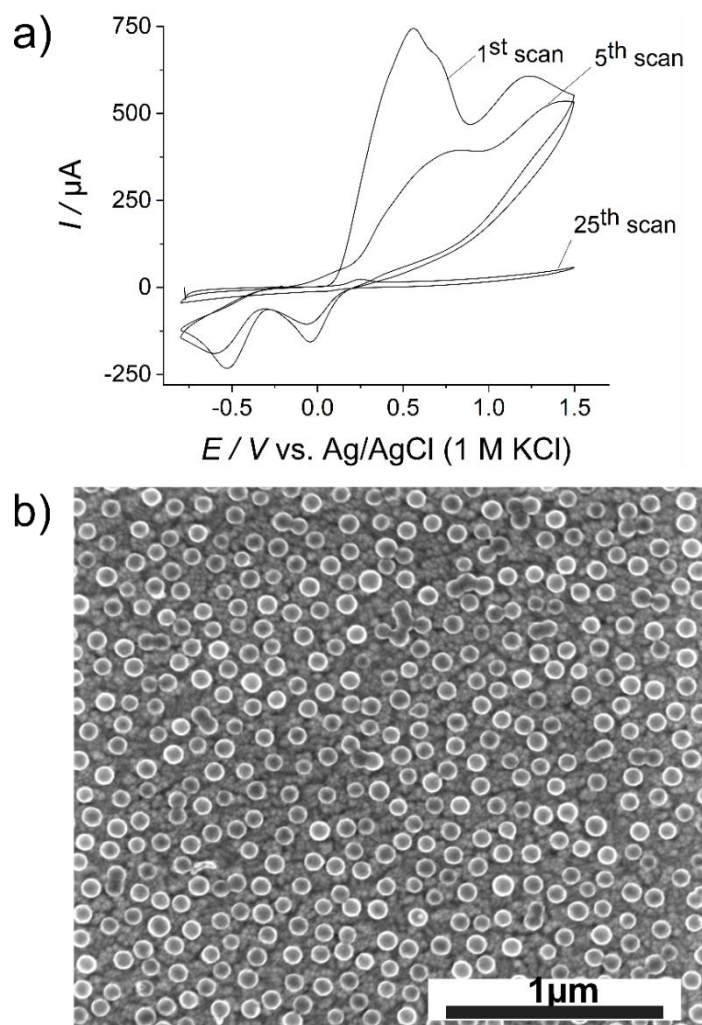


Figure 41. a) The 1st, 5th, and 25th CV scans during the electropolymerization of dopamine on (PS)PDDA/ITO from a 10 mM dopamine solution in deoxygenated 10 mM phosphate buffer of pH 7.4, b) SEM image of (PS)PDDA/ITO after the electrodeposition of polydopamine film.

AFM images of electropolymerized polydopamine (without PS NPs) reveal a smooth homogeneous topography (Figure 42a). The RMS roughness of the film is 3.31 nm for an area of 1.45 µm × 1.38 µm. The thickness of the PDA film is determined to be approximately 24.1 nm by the AFM scratching method in contact mode (Figure 42b). This system will be denoted as PDA/(PS)PDDA/ITO.
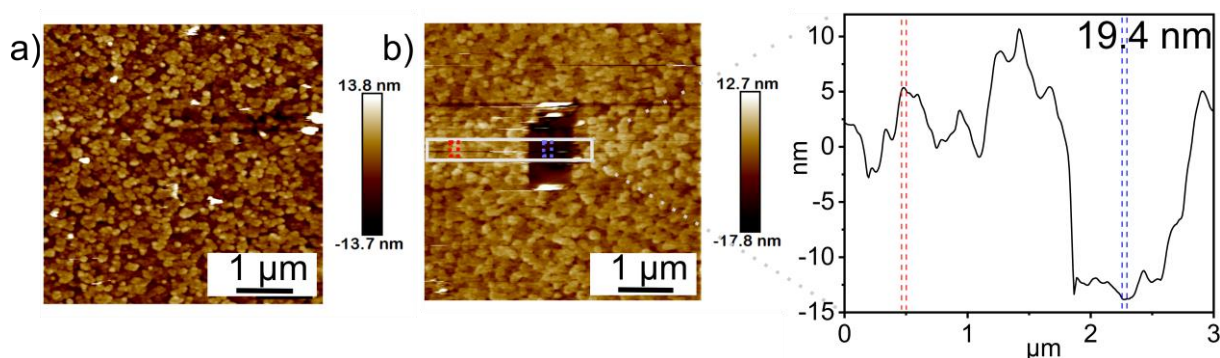
Figure 42. a) AFM topography image of the polydopamine film deposited on ITO in intermittent mode and b) AFM thickness analysis of polydopamine in contact mode.

The PDA film permeability is studied in 1 mM [Ru(NH$_3$)$_6$]Cl$_3$ + 0.1 M KCl. The well-defined quasi-reversible redox peaks in Figure 43a, curve 1 corresponds to the [Ru(NH3)6]$^{3+/2+}$ response on (PS)PDDA/ITO. Cyclic voltammograms of PDA/(PS)PDDA/ITO in 1 mM [Ru(NH$_3$)$_6$]Cl$_3$ + 0.1 M KCl revealed the insulating behavior of a pinhole-free film (Figure 43b, curve 2). This contrasts with the behavior of the NAIM system after removal of the PS NP templates. A 20 h immersion in toluene removes the PS template NPs. The ensemble of cavities behaves like a random array of nanoelectrodes (Figure 43b, curve 3). A sigmoidal curve, as observed in Figure 7b, curve 3, is expected if the hemispherical diffusion layers of the individual nanoelectrode do not overlap. This is expected if the distance between two active nanoelectrodes is about 10 times the diameter of the electrode.[162,163] The average distance between the template NPs measured is (127 ± 26) nm in Figure 44. The average diameter of the cavities (the black region in the center) is (44 ± 2) nm. Details of this estimation are provided in Figure 44. The ratio of distance to diameter is calculated to be 2.9, which is less than expected to have a sigmoidal curve. This contrast may be because not all the cavities formed after the dissolution of PS NPs are electrochemically active or because the diameter of the contact area to the substrate electrode is considerably smaller than the black regions evaluated from the SEM image. The percentage of electrochemically active cavities is calculated according to Witt et al.[41] to 19.5% by considering the cavities in the NAIM as a randomly arranged array of microelectrodes, where each cavity acts as a recessed microelectrode.
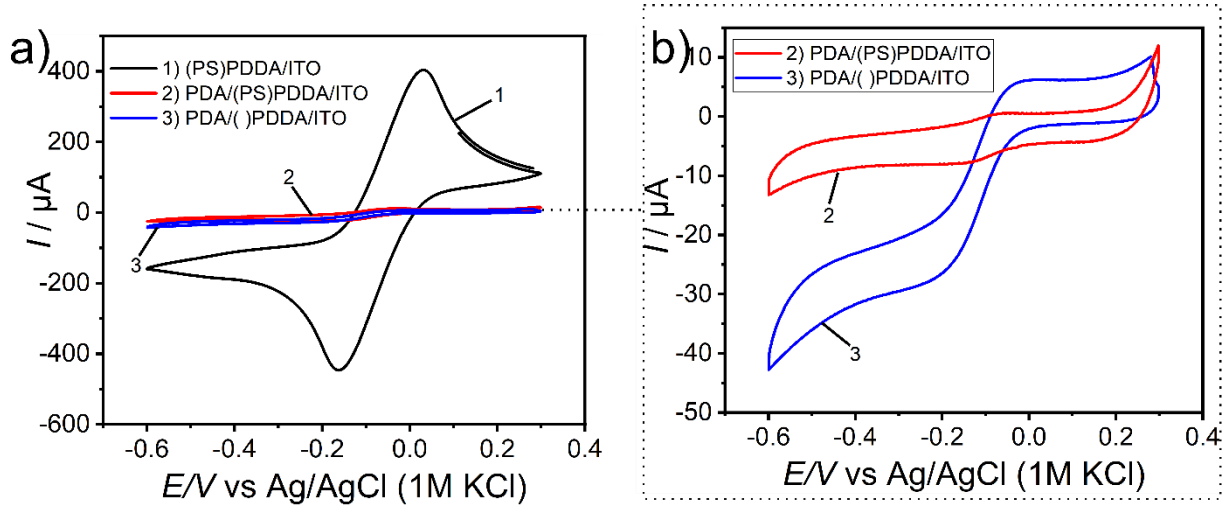
Figure 43. Redox probe studies a) at 1) (PS)PDDA/ITO, 2) PDA/(PS)PDDA/ITO, and 3) PDA/( )PDDA/ITO in 1 mM [Ru(NH₃)₆]Cl₃ + 0.1 M KCl at a scan rate of 0.1 V s⁻¹, b) magnified plot of curves 2 and 3 of (a).

If all the cavities were considered open and electrochemically active, the total current density can be calculated using Eq. (1). The symbols have the following meaning:

$\Gamma_{NP}$, the total number of NPs calculated from Figure 38b is $60 \times 10^8$ cm⁻²

$n$, the number of electrons transferred during the reaction of the redox probe is 1

$F$, Faraday constant = 96,485 As mol⁻¹

$D$, diffusion coefficient of the redox probe = $9.1 \times 10^{-6}$ cm⁻² s⁻¹

$c^*$, solution concentration of the redox probe = $1.0 \times 10^{-6}$ mol cm⁻³

The ratio $X$ between the diffusion-limited currents at an inlaid nanodisk electrode $i_d$ and a recessed nanoelectrode $i_{RAM}$ of the same radius is given by,

$$X = 1 + \frac{4l}{\pi r_{RAM}} = \frac{i_D}{i_{RAM}} \tag{1}$$

$r_{RAM} = al\sqrt{\pi} = 1.6 \, nm$, where $a$ is the diameter of the cavities and $l$ is the film thickness.

$$= 1 + \frac{4 \times (20 \times 10^{-7} \, cm)}{3.14 \times (1.6 \times 10^{-7} \, cm)} = 17$$

$$\text{Expected } j_{RAM} = \Gamma_{NP} \times \frac{1}{x} 4nFDc^* r_{RAM} \qquad (2)$$

$$= 1.98 \times 10^{-4} \; A \; cm^{-2}$$

The ratio $\Pi$ of active nanocavity to the number of template NPs can be calculated using the following equation:

$$\Pi = \frac{i_{RAM}}{A j_{RAM}} \cdot 100 \; \% \qquad (3)$$

$$= 19.5\%$$
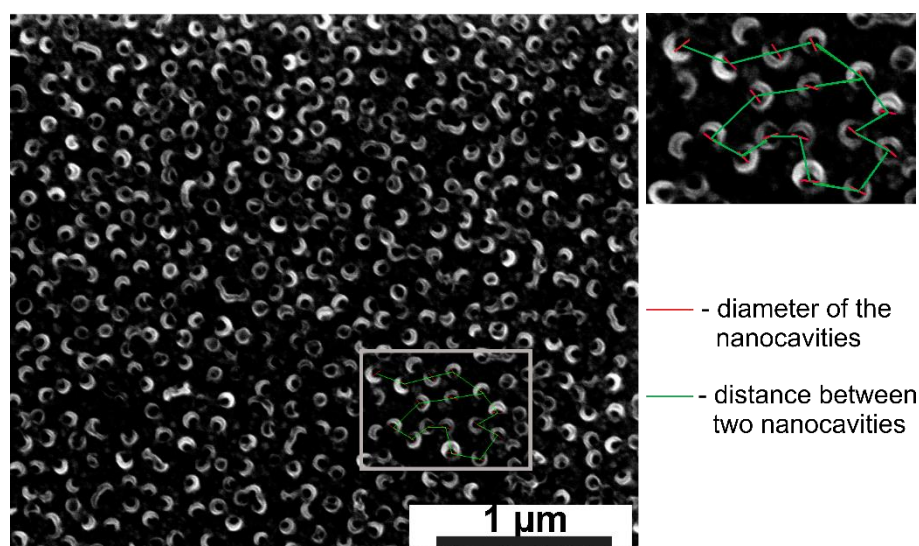


Figure 44. SEM image of the cavities formed after the dissolution of the PS NPs. The enlarged region is used for the size analysis of the nanocavities and cavity distance.

However, Figures 45a and 45b show that the shape of the cavities is reminiscent of a doughnut with cavities of 40 – 50 nm diameter, where Figure 45b is visualized at 52° for a clearer picture of the cavities. The doughnut shape can be caused by the tendency of dopamine to self-polymerize in alkaline solution by a chemical reaction of catechol and amine groups without electron transfer.[164][157] The hydrophilized surface of the PS NPs may support the deposition of chemically polymerized PDA on them.[164] The schemes in Figure 45c1 – c3 show schematic representations of the partial coverage of the PS template NPs by PDA, leading to the formation of doughnut-shaped cavities after the dissolution of the template. Similar results were observed when

81

toluene was replaced with chloroform as a solvent of PS dissolution. Previous studies have shown the tendency of PDA to coat the surface of PS NPs in suspension, a phenomenon that has been exploited to form stable hollow spheres widely used in drug delivery.[164]
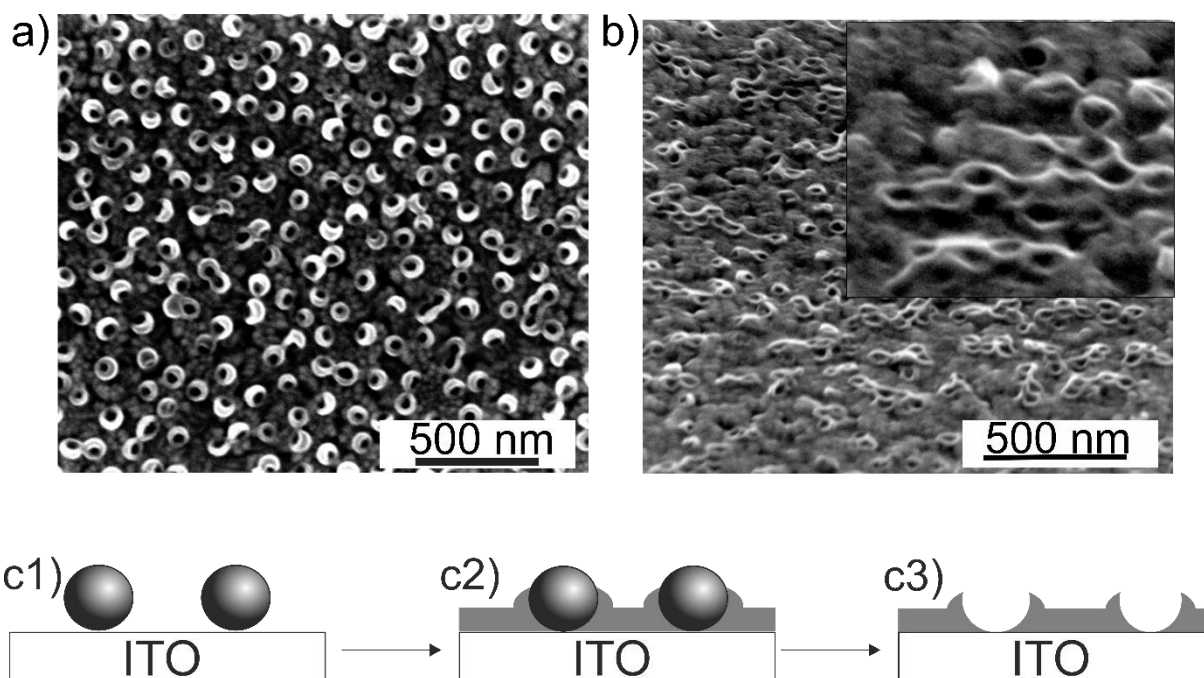


Figure 45. SEM image a) recorded after the dissolution of PS NPs from the PDA-based NAIM, b) of the cavities recorded at 52° tilt. In the inset, a region is magnified for clarity; c) Schematic of the PDA/(PS)PDDA/ITO: PDDA/ITO surface modified with PS NPs (c1) followed by the electropolymerization of PDA matrix which partially coats the NPs (c2) and the removal of PS NPs from the matrix forms dough-nut shaped cavities (c3).

In a study by Xie et al.,[165] sulfonated PS NPs were used as sacrificial templates on which PDA was self-polymerized at a basic pH. On removal of PS NPs, doughnut-shaped cavities like the ones discussed in this chapter were formed, which found applications in drug delivery. Similarly, studies by Wang et al.[164] have shown a similar approach where PDA was self-polymerized on the sulfonated PS NPs. Followed by PS NPs removal, similar cavities were formed, which were found to be helpful in the field of tissue engineering and regenerative medicine. The rough surface of PS NPs due to the sulfate groups also facilitates the adhesion of PDA onto them.

The extent of detachment of polydopamine coating before and after immersion in toluene is investigated with the aid of XPS (Figure 46). The XPS study was done to study the extent to which a 20 h immersion in toluene affects the PDA film on ITO. The N 1s spectra of polydopamine before and after immersion in toluene are fitted with three peaks corresponding to =N-R around 398.2 eV, R-NH-R at 399.5 eV, and R-NH$_2$ at 401.3 eV, proving the presence of a stable film even after immersion in toluene.[166]
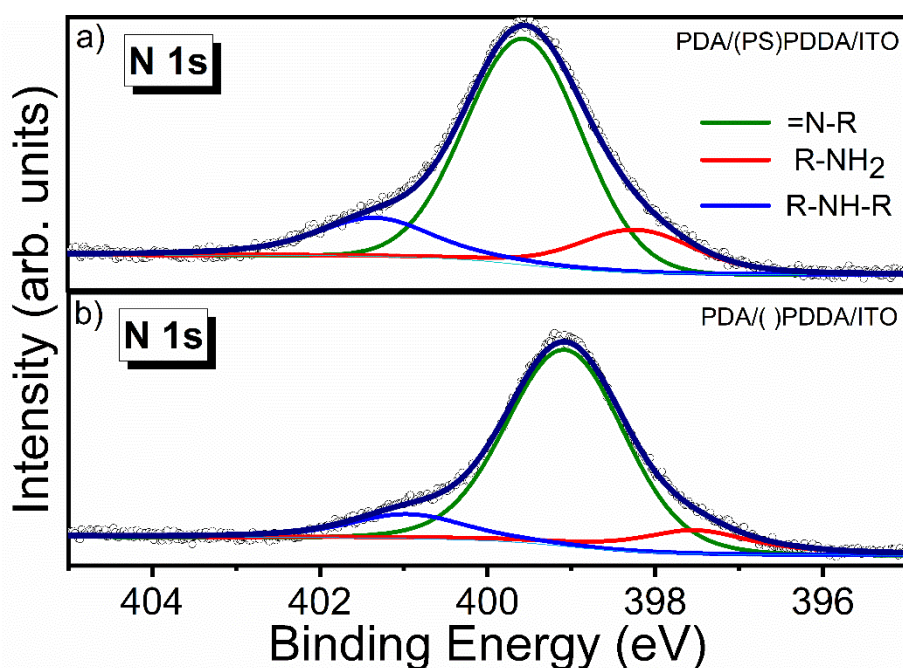


Figure 46. N 1s XP spectra of PDA/(PS)PDDA/ITO a) before and b) after immersion in toluene for 20 h for the removal of PS NPs.

Due to the overgrowth of PDA film over PS NPs, the formed cavities were doughnut-like after the dissolution of PS NPs. Such holes affect the uptake ability of the NAIM system. Also, the PDA overgrowth makes the removal of PS NPs difficult and time-consuming. It requires prolonged exposure to toluene for the removal of PS NPs. Some cavities are distorted due to the long exposure. Since there is no control over the self-polymerization process, the reproducibility of the system is also challenging.

### 6.2.2 *p*-Phenylene diamine-Based NAIM

A brief study is conducted with other polymer films to probe the problem of film overgrowth when polydopamine is used as the matrix. Initially, a *p*-phenylenediamine (*p*-pd)-based matrix was studied to optimize the parameters. Electropolymerization of

aromatic diamines offers several distinct advantages. These advantages stem from the unique properties of aromatic diamines. The presence of multifunctionality due to the free amino group per repetitive unit makes it more attractive as a polymer film. Electropolymerization provides precise control over the deposition of the polymer film onto the electrode surface. This controlled deposition allows for the fabrication of uniform and well-defined thin films with tuneable thickness, crucial for ensuring consistent and reproducible films.[167,168]
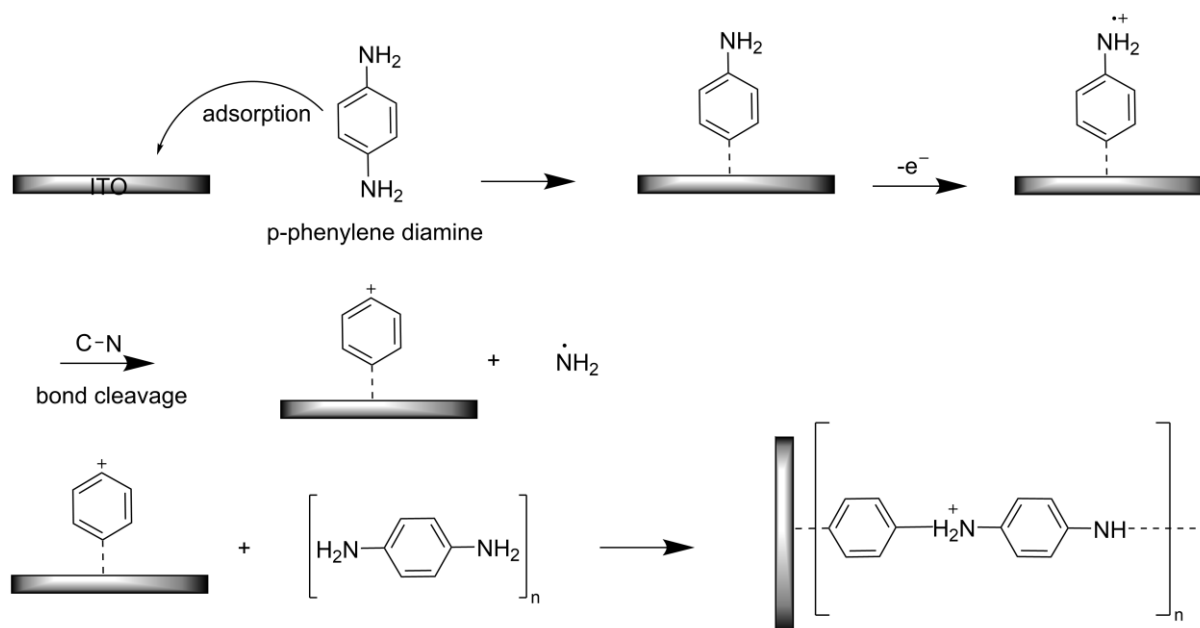


Figure 47. Mechanism of electropolymerization of *p*-pd leading to forming a homogeneous layer on ITO.

A *p*-pd film was initially electropolymerized on a cleaned ITO from 5mM *p*-pd in 0.1 M sodium phosphate buffer of pH 7 for 25 potential cycles. The mechanism for electropolymerization of *p*-pd is shown in Figure 47.[169,170] Figure 48a shows the cyclic voltammogram for the electropolymerization of *p*-pd. Initially, the *p*-pd monomer adsorbs on the surface of the ITO substrate followed by the oxidation of the monomer. An oxidation peak at 276 mV corresponds to forming a radical cation after removing an electron from one of the amino groups. This is followed by the cleavage of the C-N bond, forming a radical cation, which attacks the *p*-pd monomers in solution. A small reduction peak can be observed at 53 mV (Figure 48b). This might be due to the reduction of radical cations, forming the *p*-pd monomer.[171]

84
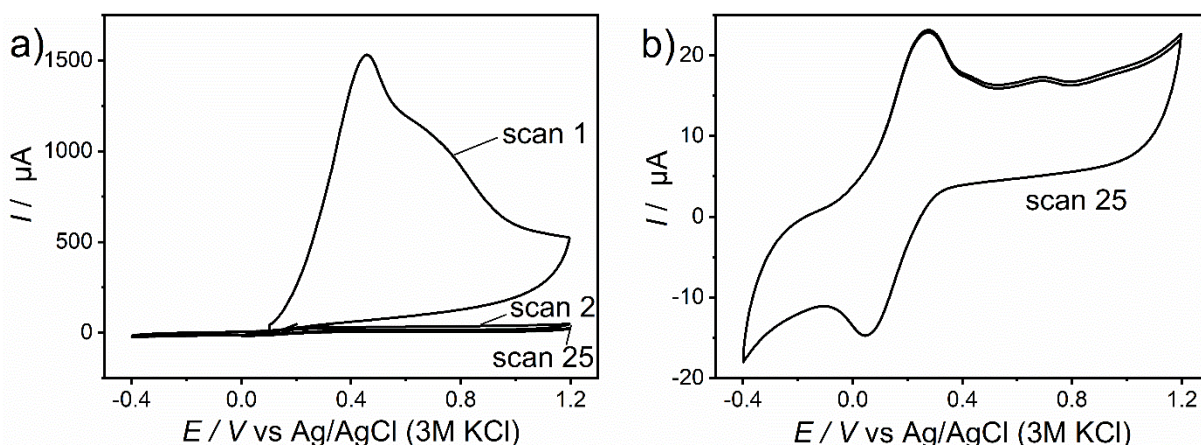
Figure 48. a) The 1st, 2nd, and 25th CV scans during the electropolymerization of *p*-phenylene diamine on (PS)PDDA/ITO from a 5 mM p-phenylene diamine solution in deoxygenated 0.1 M phosphate buffer of pH 7, b) 25th CV scan during the electropolymerization of p-phenylene diamine is shown for clarity.

Film topography was studied in tapping mode using an NCHV-A tip of tip radius 8 nm. AFM image of the polyphenylene diamine film deposited on bare ITO is shown in Figure 49a. From the AFM studies, the presence of a smooth polymer film can be inferred. The RMS roughness of the film is 3.4 nm for an area of 1 μm × 1 μm. The thickness of the film is an essential parameter for the NAIM system. The thickness of the deposited *p*-pd film on ITO (*p*-pd/ITO) was studied by the AFM scratching method to be 19 – 20 nm (Figure 49b).
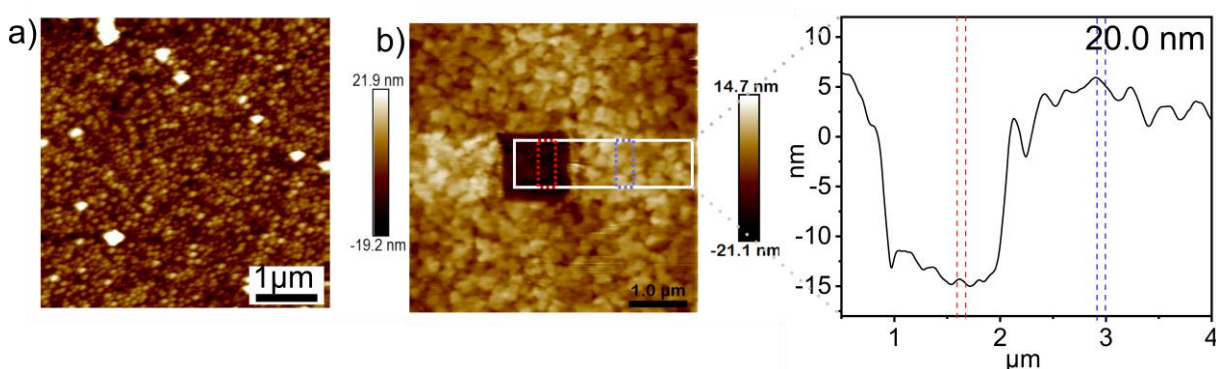


Figure 49. a) AFM topography image of polyphenylene diamine film deposited on ITO in intermittent mode and b) AFM thickness analysis of polyphenylene diamine in contact mode.

After optimizing *p*-pd film deposition conditions and thickness, the *p*-pd film was electropolymerized on a PS NP-decorated PDDA/ITO. The film was electropolymerized under a similar situation as explained before. Figure 50a shows the SEM image after the electropolymerization of *p*-pd. Subsequently, the sample (*p*-pd/(PS)PDDA/ITO) was immersed in toluene for 20 h to remove the PS NPs from the sample in order to form the cavities. SEM images recorded after the exposure to toluene reveals doughnut-shaped cavities, as observed in the PDA-based NAIM system, along with a few irregular cavities (Figure 50b). Figures 50c and d show the AFM topography and phase images recorded after the dissolution of PS NPs.



Figure 50. SEM image a) of (PS)PDDA/ITO after the electropolymerization of *p*-pd; b) recorded after the dissolution of PS NPs from the *p*-pd-based NAIM; c) topography image and d) phase image of the cavities recorded in the intermittent contact mode.

### 6.2.3 Polyphenol-Based NAIM

Later, PDA and *p*-pd were replaced with polyphenol (pph) film to examine the NAIM system. The electropolymerization of phenol is a well-kno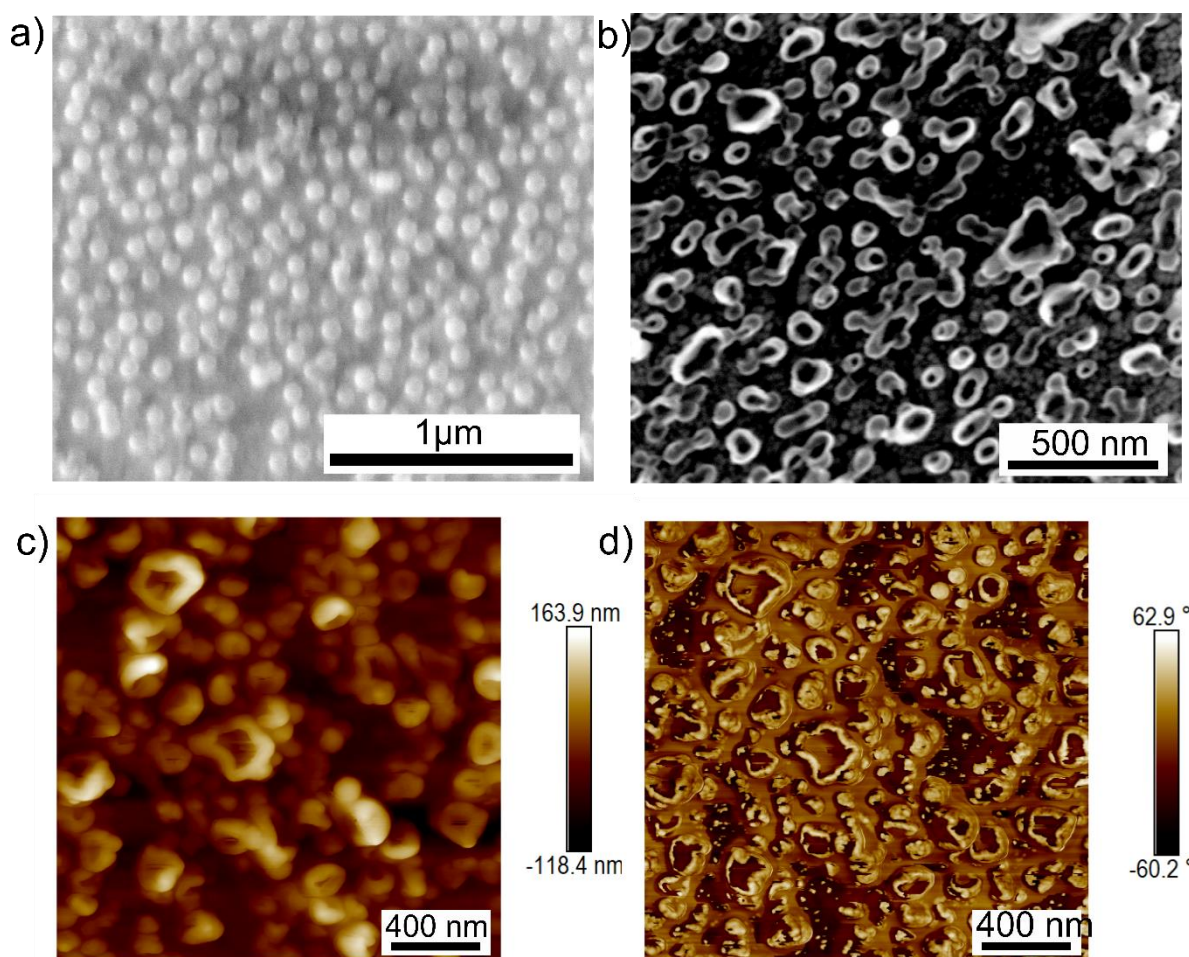wn process, and the mechanism is explained in Chapter 5. The ITO substrate modified with PDDA after exposure to PS NPs ((PS)PDDA/ITO) was subjected to polyphenol electropolymerization. The electropolymerization of phenol was monitored through CV, and the subsequent phenol oxidation curve was observed at 0.95 V vs Ag/AgCl. A decrease in the anodic current in the subsequent cycles confirmed the presence of a passivating polyphenol film on (PS)PDDA/ITO. This sample state will be denoted as pph/(PS)PDDA/ITO for brevity. This sample was exposed to toluene for 12 h to remove the PS NPs from the matrix. AFM studies of the sample after exposure to toluene exhibit similar doughnut-shaped cavities as observed in PDA/( )PDDA/ITO and *p*-pd/( )PDDA/ITO. Figure 51 shows the AFM image of the polyphenol-modified NAIM matrix after toluene immersion.
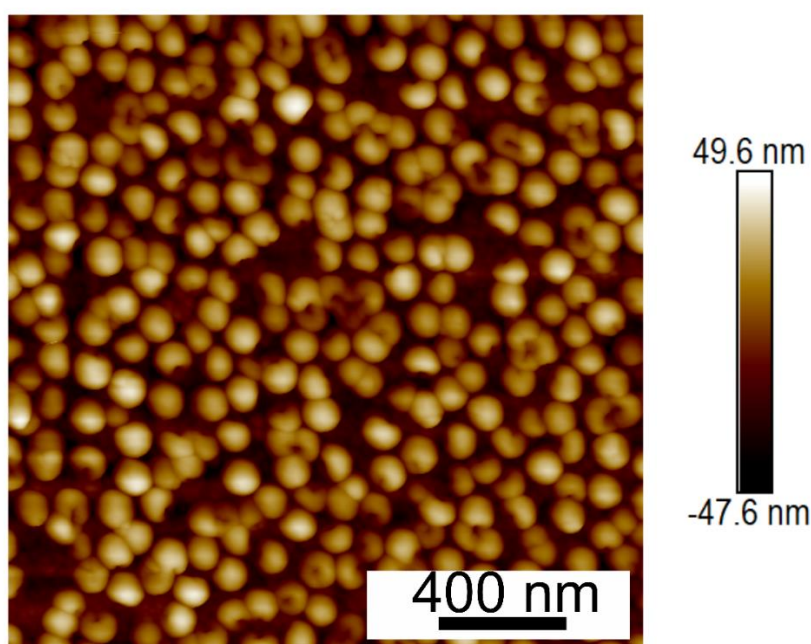


Figure 51. AFM topography image recorded after the dissolution of PS NPs from the pph-based NAIM in the intermittent mode using an NCHV-A AFM tip ($k$ = 42 N m$^{-1}$).

From the above examples, a common observation is the formation of doughnut-shaped cavities on the dissolution of PS NPs from the NAIM matrix. A long immersion time in toluene is required to form such cavities. This also led to the formation of irregularly shaped cavities. The presence of cavities was not uniform overall on the sample surface. The size of the cavities was measured to be 44 – 48 nm using ImageJ software. However, it can be observed that the cavity shape significantly limits the uptake of analyte NPs.

Insulating PS NPs were chosen to build a NAIM matrix in order to prevent the film overgrowth over the NPs, as explained in Chapter 5. Here, the unexpected occurrence of such specifically shaped cavities points to the overgrowth of polymer films over the NPs as explained before. The polymer properties can be tuned by functionalizing the polymer backbone, which can determine the physical properties of the polymer. For instance, the nature of rigid hydrophobic PS NPs transmutes to soft hydrophilic sulfate PS on sulfation.[172] PDA has been widely used to coat NPs to enable various surface properties. Previous studies have shown that the sulfonate groups on the PS NPs[173] interact readily with other functional groups of various polymers. Studies by Lu et al.[173] had shown that lightly sulfonated PS NPs can interact with polyamide-6 through hydrogen bonding between sulfonate and amide groups or via ion-dipole interaction between the sulfonate species and polarized N-H bond. Correspondingly, the hydrogen bonding between the N-H of polybenzimidazole and sulfonate groups of PS NPs produced a new polymer miscible blend. The dissolution of spherical PS NPs resulted in a hollow polybenzimidazole ring advantageous for developing PEM fuel cells.[174] The above examples suggest the different kinds of interactions between sulfonated PS NPs and multifunctional polymers. Anticipated interactions between the sulfonate groups on polystyrene NPs (PS NPs) and polymer films are likely to occur when sulfate-modified PS NPs are employed. This might result in the growth of these polymer films over PS NPs, causing the doughnut-shaped cavities.

### 6.2.4 Aryl diazonium-Based NAIM

The last approach to study the sulfate-modified PS template NP-based NAIM system was developing a matrix by in situ diazotization of 3-aminopyridine (3-AP) followed by its electrografting. Electrografting of diazonium salts is a versatile and powerful technique to modify the surface of various conductive substrates, such as metals or

carbon-based materials, with organic functional groups.[175] The process involves the electrochemical reduction of diazonium salts, converting them into stable layers that are covalently attached to the substrate. This method has gained significant interest in various fields due to its ability to tailor surface properties, impart specific functionalities, and enhance material performance[176] facilitating vast possibilities for interdisciplinary applications in various fields.[175–177] The detailed mechanism is explained in Chapter 7.

Specifically, pyridine has also been successfully electrografted on carbon and metal surfaces from the in situ-generated diazopyridinium cations.[101,178] It is to be noted that diazopyridinium salts are highly unstable and not available as salt. The surface modification with 3-diazopyridinium cations is considered stable and beneficial compared to 2-amino and 4-amino diazopyridinium cations.[101,179]
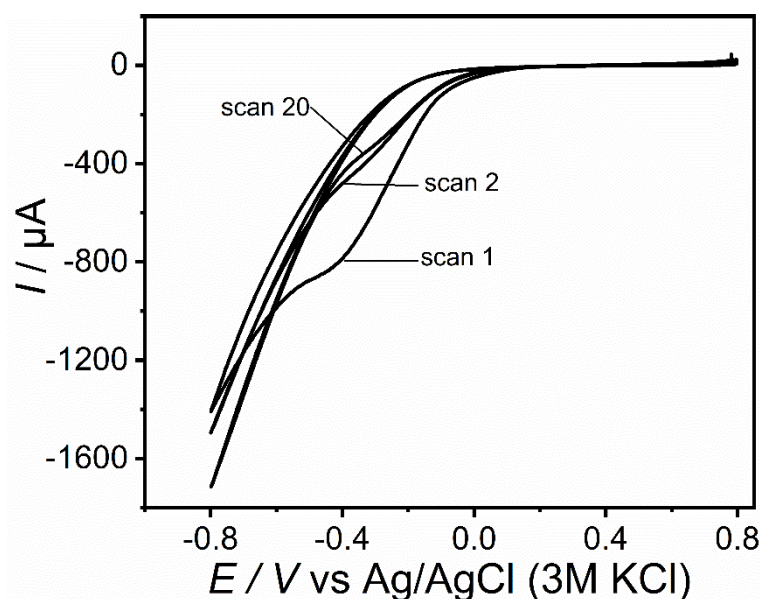


Figure 52. The 1st, 2nd, and 20th CV scans during the electrografting of 3-aminopyridine on PDDA/ITO from 20 mM 3-aminopyridine + 40 mM NaNO$_2$ in 0.5 M HCl.
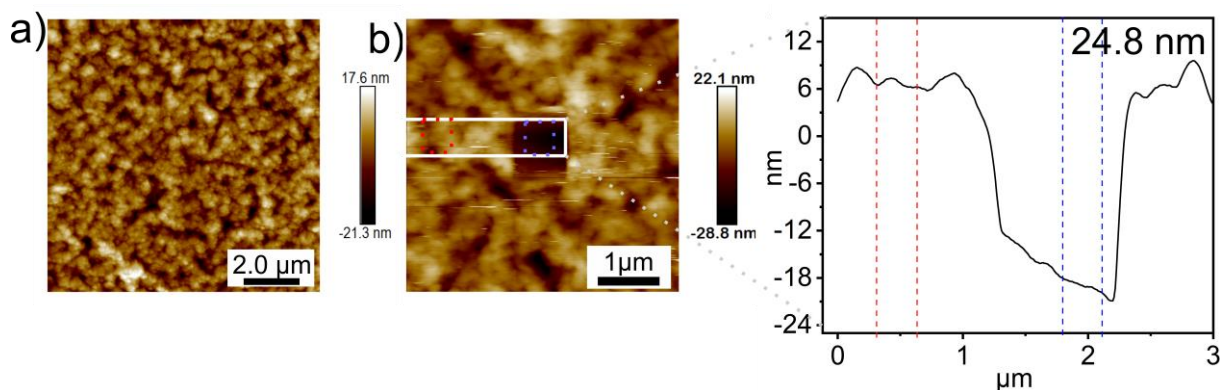
Figure 53. a) AFM topography image of the 3-aminopyridine film deposited on ITO in intermittent mode using an NCHV-A AFM tip ($k$ = 42 N m$^{-1}$) and b) AFM thickness analysis of the 3-aminopyridine film in contact mode using an MSCT AFM tip ($k$ = 0.6 N m$^{-1}$).

An ITO surface was initially modified with a PDDA layer to attach the negatively charged sulfate-modified PS NPs. After the modification with PS NPs, the PS(PDDA)/ITO was subjected to electrografting as described in section 4.6.3. The CV corresponding to the electrografting of 3-AP is shown in Figure 52. The potential of ITO was scanned between 0.8 to -0.8 vs Ag/AgNO$_3$ in the presence of 3-diazopyridinium cations. In the first scan, an irreversible reduction peak can be observed around -0.39 V which disappeared in the subsequent scans. The thickness of the electrografted aminopyridinium layer ranged between 22 – 25 nm. (Figure 53). The sample at this stage can be abbreviated as 3-AP/PS(PDDA)/ITO. Figure 54a shows the SEM image of PDDA/ITO after exposure to PS NP solution for 2 h, and Figure 54b shows the SEM image after electrografting the 3-AP film. It can be observed that the PS NPs on the surface of ITO are undisturbed during the electrografting process.
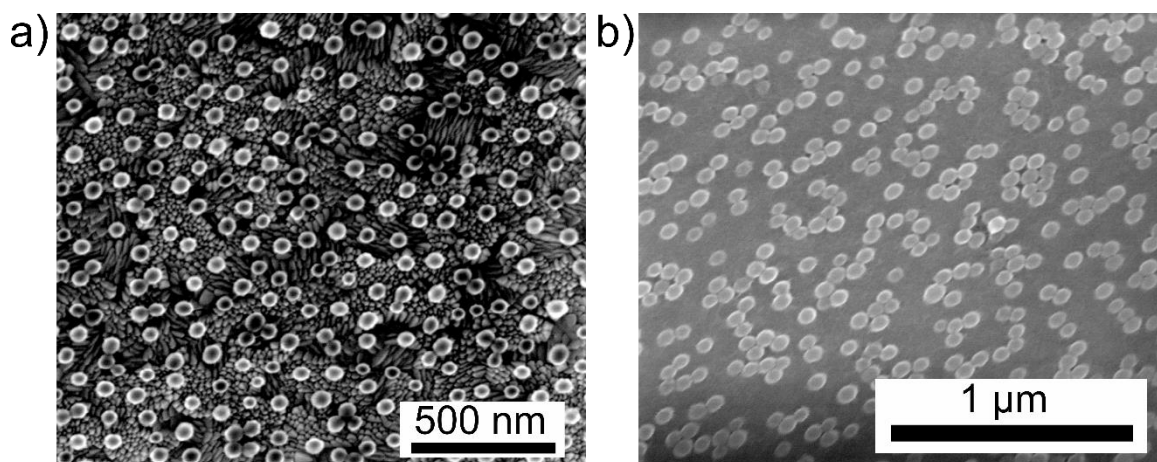
Figure 54. SEM image of a) PDDA/ITO after a 2 h immersion in sulfate-modified PS NP dispersion, b) (PS)PDDA/ITO after electrografting the 3-aminopyridine-based matrix.

After a 12 h exposure to toluene, the sample was studied by SEM and AFM to observe the morphology of the cavities. Unlike in the cases of polymerized NAIMs, the presence of well-defined cavities was detected. Figures 55a and 55b show the SEM and AFM images of the sample after the removal of PS NPs. The size of the cavities was measured to be (49 ± 7) nm using ImageJ software, and the corresponding size distribution studies are shown in Figure 55c. The difference between the size of the template NPs and the cavities was of concern. A hypothesis was the selective removal of PS NPs while the sulfate groups remained in the matrix. This was confirmed by studying the NAIM system before and after the removal of the dissolution of PS NPs. Figure 56 shows the XPS studies of (PS)PDDA/ITO, 3-AP/(PS)PDDA/ITO, and 3-AP/( )PDDA/ITO. A doublet around 167 – 169.0 eV confirms the presence of sulfate groups.[180,181] Analyzing trace elements are difficult from the background noise and require multiple scanning of small areas.
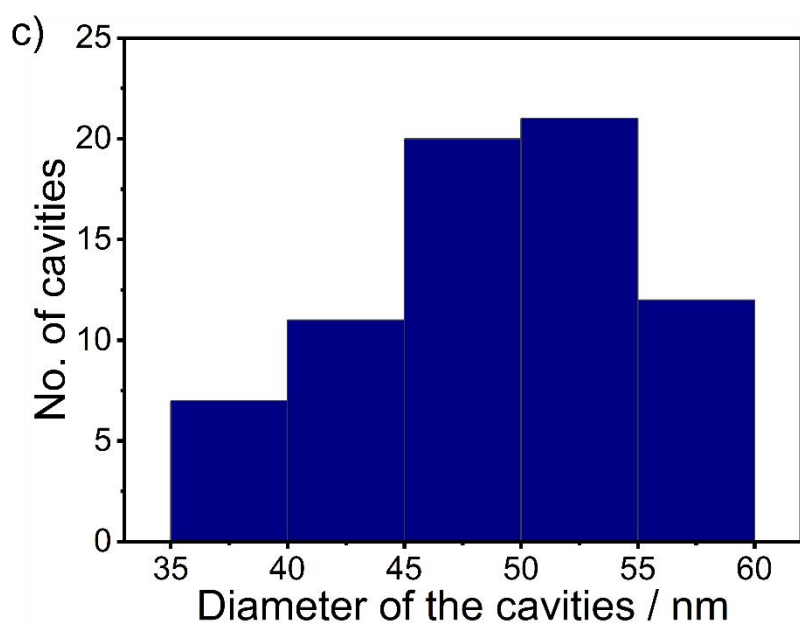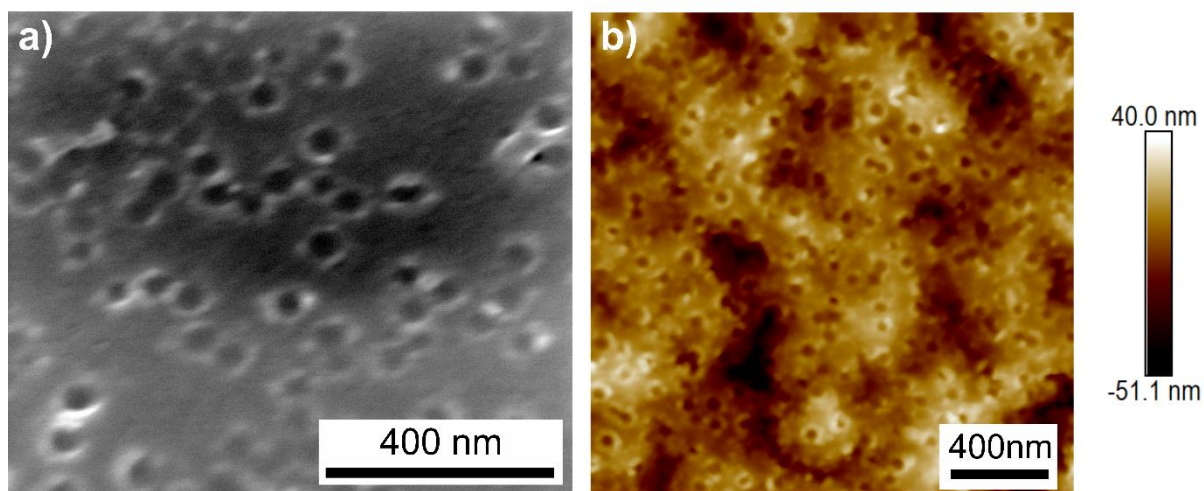
Figure 55. a) SEM image recorded after the dissolution of PS NPs from the 3-AP-based NAIM, b) AFM image of the cavities recorded in the intermittent mode using an NCHV-A AFM tip ($k$ = 42 N m$^{-1}$), and c) size distribution of the cavities measured using ImageJ software.
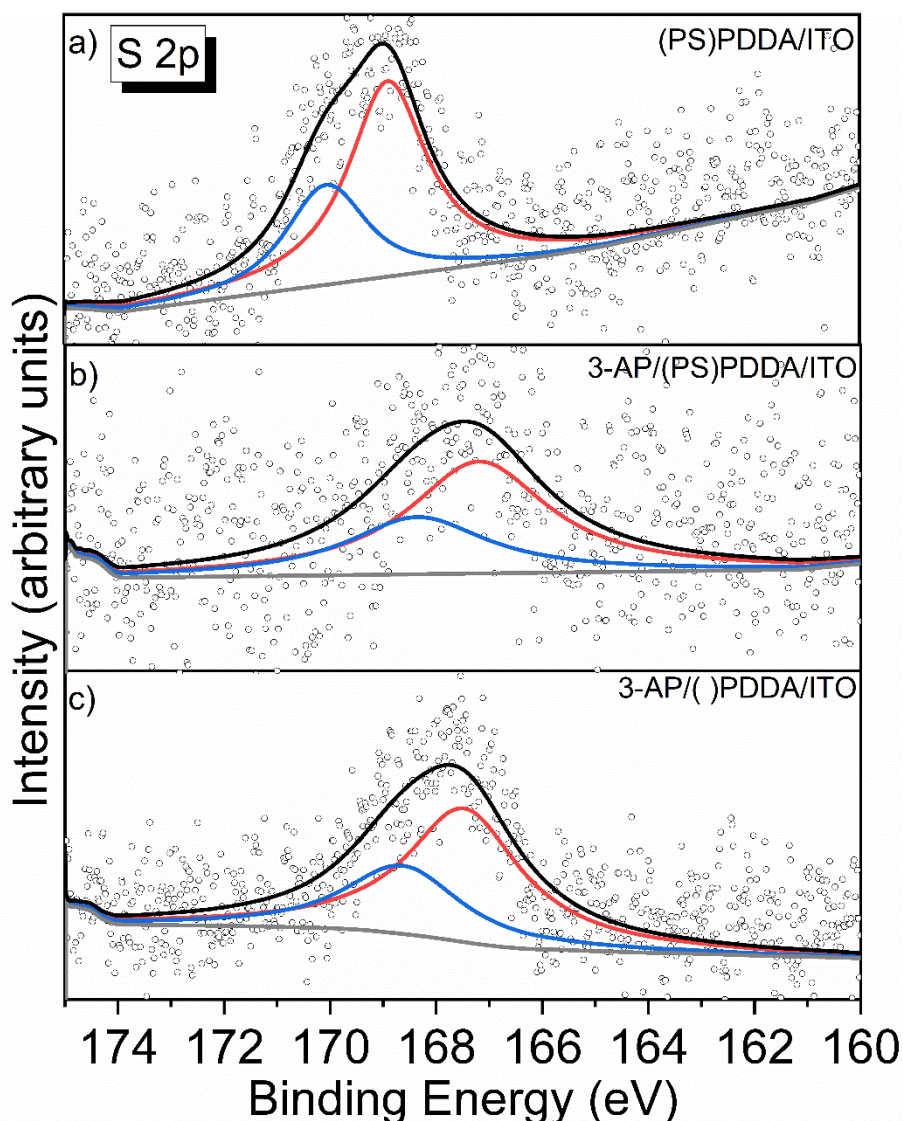
Figure 56. S 2p spectra of a) (PS)PDDA/ITO, b) 3-AP/(PS)PDDA/ITO, and c) 3-AP/( )PDDA/ITO.

The occurrence of well-defined cavities under these conditions was remarkable. Electrografting is an electron-initiated process that involves electron transfer between the substrate and the reagent. This results in a covalent bond between the substrate surface and the organic film layer (grafting).[176] The reactive species produced after electron transfer remain neutral after grafting, refraining from polymerization and avoiding interaction with the embedded PS NPs, thereby preventing the formation of a partial layer over them.[49] On analyzing the mechanism of oxidative electropolymerization, which begins with forming a cationic radical and can react with either the neighbouring radical cations or neutral monomers to produce the polymer.[182] The sulfate modification of PS NPs increases their polarity, thereby

93

attracting the monomers or the cationic radicals onto their surface forming core-shell templates.[183] This could be the explanation for the formation of a partial layer over the PS NPs during electropolymerization. Developing a partial polymer layer over the PS NPs possibly increases the time for PS NP dissolution in toluene. This may be the reason for the formation of doughnut-shaped cavities. Studies have shown that the colloidal templated electropolymerization of PANI yielded nanopatterned polymer films. Similar cavities were observed when the colloidal template (sulfonated PS NPs) was removed in a suitable solvent.[184] This property of sulfonated PS NPs is exploited in several studies to form nanopatterned surfaces as well as in the field of nanolithography.[185]

## 6.3   Reuptake Studies

In the previous section, NAIM systems developed from polymerized polydopamine, polyphenol, p-phenylene diamine, and electrografted 3-aminopyridine were studied for the size and shape of the cavities formed after the removal of template PS NPs. The NAIM systems developed were then analyzed for their ability to recognize analyte NPs based on size and shell.
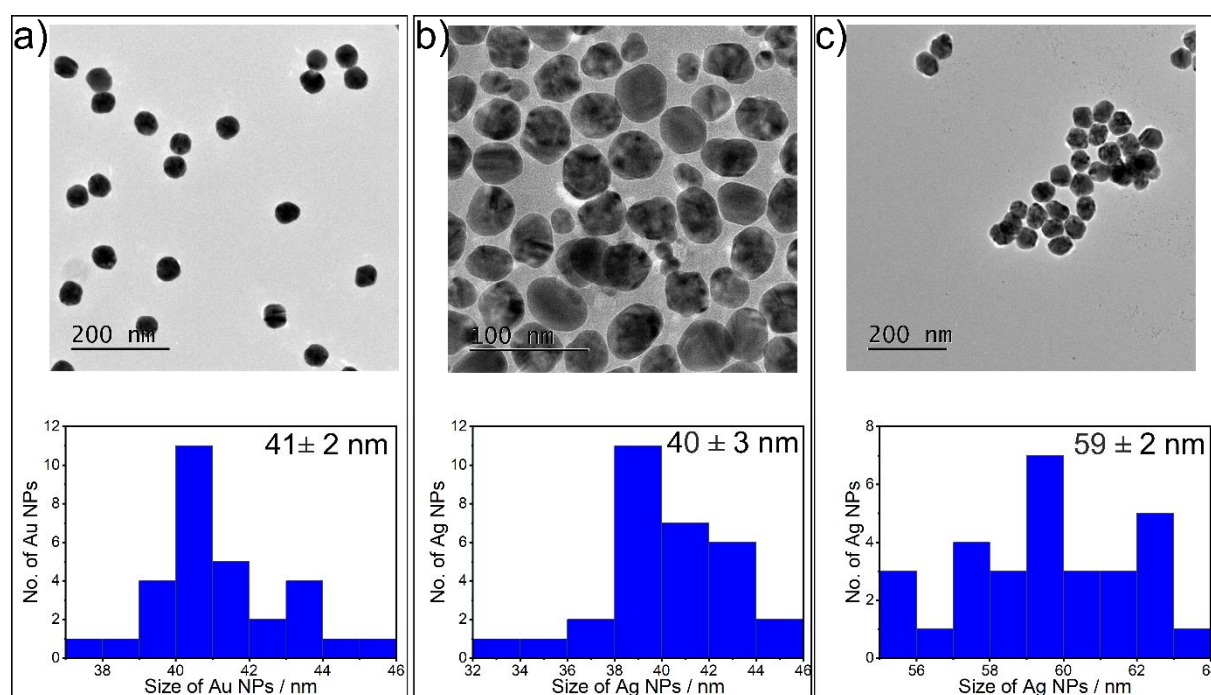


Figure 57. TEM images and size distribution of a) 40 nm Au-Cit NPs, b) 40 nm Ag-CT NPs and c) 60 nm Ag-CT NPs.

The uptake ability of the PDA-based NAIM matrix was studied for the uptake of citrate-stabilized Au NPs as analyte NPs with 40 nm diameter (Au-Cit NP) and citric acid-tannic acid complex-stabilized (CT) Ag NPs (Ag-CT NP) diameters of 40 nm and 60 nm. The TEM images of synthesized Au NPs and Ag NPs confirm the formation of spherical NPs. At least 30 NPs are counted and measured for size using ImageJ software. The TEM images and corresponding size distributions are given in Figure 57. The PDA matrix is expected to interact with the acidic groups in the ligand shell of the NPs to promote the binding to the NAIM. SEM collects information on all NP attached to the NAIM surface. In contrast, linear sweep voltammetry of the NP dissolution in halogenide-containing electrolytes informs about those NPs that communicate electronically with the ITO support electrode. Figure 58a represents the SEM image of PDA/(Au-Cit)PDDA/ITO after the uptake of 40 nm citrate-stabilized Au NPs from an aqueous colloidal suspension. The surface of the NAIM film was decorated with NPs, from which most stick to the surface outside the cavities due to the interaction between the functional groups on the PDA matrix and the carboxylate groups from the citrate functionalization on Au NPs.[186] We call the NPs outside the cavities "non-specifically adsorbed." Those NPs cannot communicate with the electrode because the NAIM matrix has a thickness of 20 nm which is larger than the tunnelling distance. Some NPs are located right in the center of the cavities of the NAIM system, which is especially evident in the enlarged reproduction of an image section in Figure 58a. Those particles are expected to contribute to the electrochemical signal in Figure 58c because their distance to the support electrode is smaller than for the non-specifically adsorbed NPs. It should be noted that not all the cavities have taken up an NP. Not all cavities may be widely open or in an upright position to allow the uptake of a 40 nm Au NP.
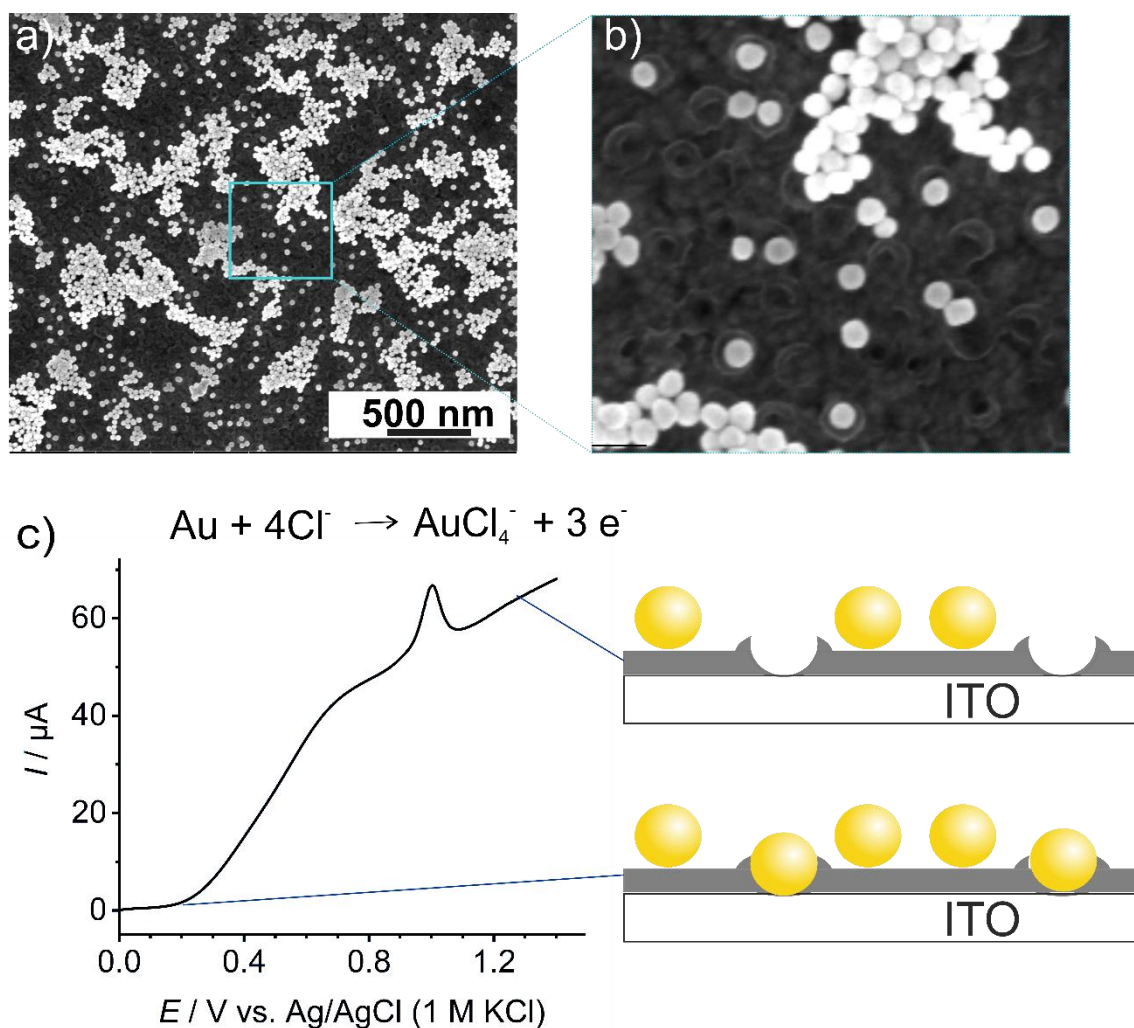
Figure 58. a) SEM image of the NAIM system after immersion in 40 nm Au-Cit NP for 15 h, b) a region is enlarged to show the uptakes c) LSV curve obtained with PDA/(Au-Cit)PDDA/ITO during the eelctrodissolution of Au-Cit NPs in 3 M KCl at a scan rate of 0.05 V s$^{-1}$.

Size-selective recognition is demonstrated with Ag NPs of 40 nm and 60 nm with citric acid-tannic acid complex-stabilized Ag NPs. The PDA/( )PDDA/ITO sample was immersed in a suspension of 40 and 60 nm Ag-CT NP for 15 h and afterward analyzed by SEM. Figure 59a and 59b shows the NAIM matrix after exposure to 40 nm and 60 nm Ag-CT NPs, respectively. Notably, there are barely any non-specifically adsorbed NPs on examining various regions of the NAIM by SEM, which points to a lack of significant non-specific electrostatic interactions between the Ag-CT NP and the PDA matrix. A few NPs of 40 nm diameter are located inside the cavities (marked by arrows), as seen in Figure 59a. On immersing a PDA/( )PDDA/ITO NAIM system in a suspension of Ag-CT NPs with 60 nm diameter, neither an uptake of the NPs into the

cavities nor any considerable signs of non-specific adsorption were observed (Figure 59b). The empty voids can be seen in this image frame. The fact that the cavities remain vacant is probably caused by the larger size of NPs that prevent their uptake into the cavities. This finding substantiates the size-selective recognition ability of the PDA-based matrix, which prefers 40 nm over 60 nm Ag-CT NPs.
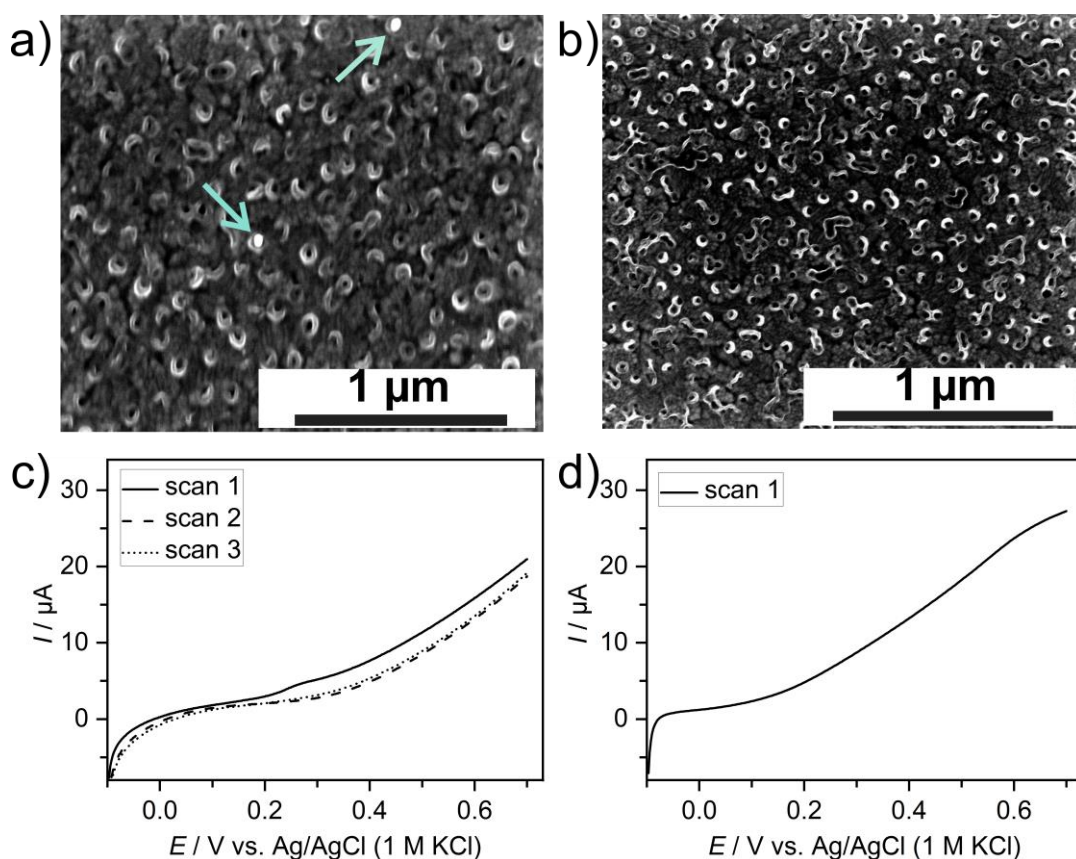


Figure 59. SEM images of the NAIM system after immersion in a) 40 nm Ag-CT NP for 15 h and b) 60 nm Ag-CT NP for 15 h. LSV curves obtained with PDA/(Ag-CT)/PDDA/ITO exposed to c) 40 nm Ag-CT NP solutions and d) 60 nm Ag-CT NP solutions for 15 h in 0.1 M NaNO$_3$ at a scan rate of 0.05 V s$^{-1}$.

In contrast to Au NPs, the used Ag NPs do not show considerable non-specific adsorption to the outer surface of the PDA NAIM layer. Au NPs and Ag NPs were synthesized according to Bastús et al.[96,97] but using different reducing agents, i.e., sodium citrate for Au NPs and a mixture of sodium citrate and tannic acid for Ag NPs. Using tannic acid decreases the size dispersity of the resulting Ag NPs. Ranoszek-Soliwoda et al.[97,187] proved the formation of the CT complex in the ligand shell of the Ag NPs when a mixture of reductants and capping agents is used in the NP synthesis.

Tannic acid acts as a reducing agent and oxidizes to a quinone.[187] In contrast to Au-Cit NPs, Ag-CT NPs do not establish an electrostatic interaction with the PDA matrix. This may explain the absence of Ag NP adsorption on the PDA NAIM surface. If the analyte NPs cannot interact with the matrix, the uptake is solely determined by size. The comparison of the uptake behavior of Au-Cit NPs and Ag-CT NPs also illustrates the importance of interaction between the ligand shell and the matrix. A relatively small change in the chemical structure of the ligand shell can cause a profound effect on the uptake behavior. We hypothesize that a slight change in the NAIM polymer may cause a profound change in the uptake behavior for the same analyte NPs.

The NPs inside the cavities can be recognized by electrolytic dissolution in linear sweep voltammetry (LSV). Figure 58c shows the electrochemical oxidation of Au NPs in 3 M KCl. The electrooxidation of Au NPs causes a distinct oxidation peak in the first scan. If the experiment is repeated, this peak does not occur because the Au NPs in the cavities are dissolved, and the non-specifically adsorbed particles cannot participate in the electrode reaction. Thus, the detection principle helps distinguish NPs in cavities and non-specifically adsorbed NPs at the outer surface of the NAIM layer. After the electrochemical detection, the non-specifically adsorbed Au NPs are still present on the surface, as shown in the SEM image recorded after electrochemical detection (Figure 60) The large number of loosely attached NPs does not contribute to the oxidation signal as the film is insulating in nature and blocks electron transfer. The NPs that contribute to the electrochemical system must therefore be those that reside inside the cavities and are, thus, size-selectively enriched.

Electrooxidation of Ag-CT NP with a 40 nm diameter taken up in the NAIM system causes a shoulder at 0.3 V in the voltammogram recorded in 0.1 M NaNO$_3$ (Figure 59c). This peak does not appear in an analogous experiment using the larger Ag-CT NP with a 60 nm diameter, as observed in Figure 59d. This corroborates the observation in SEM images in Figure 59a vs. Figure 59b that do not show uptake of the 60 nm Ag NPs in the cavities. The extreme difference in the uptake of Ag-CT NPs vs. Au-Cit NPs illustrates the potential for improving uptake and selectivity by a relatively minor modification of the ligand shell and possibly by the chemistry of the NAIM system.
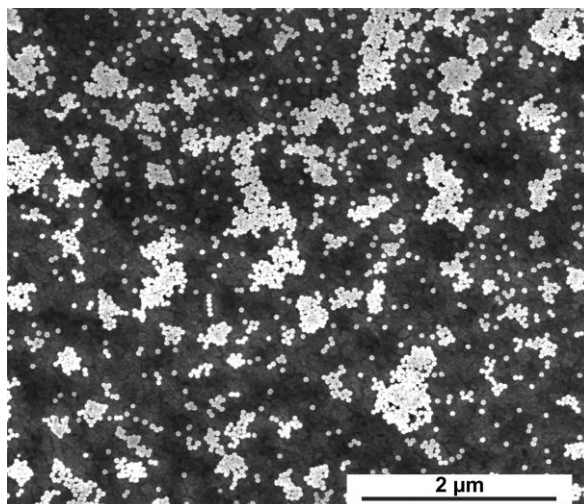
Figure 60. SEM image of a selected area of PDA/(Au-Cit )/PDDA/ITO with the non-specifically adsorbed Au-Cit NPs after the electrochemical dissolution in 3M KCl.

The *p*-pd modified NAIM system was studied briefly for its uptake ability with 40 ± 3 nm Au-Cit analyte NPs. The dissolution of Au-Cit NPs in 3 M KCl at 0.05 V s$^{-1}$ was performed to investigate the uptake efficiency of this NAIM system. A distinct peak is typical for the electrooxidation of Au-Cit NPs around 0.89 V in the first LSV cycle was observed. The peak current decreased in the subsequent scans and eventually disappeared, indicating the complete oxidation of Au-Cit NPs (Figure 61). This verifies the specific uptake of Au-Cit analyte NPs by a *p*-pd-based NAIM system. The non-specifically adsorbed NPs were visible in the SEM images even after the Au dissolution studies, substantiating the selective dissolution of Au-Cit NPs only present inside the cavities formed.

However, the specific uptake was low in the above-discussed NAIM systems. This could be due to the partially open cavities. Moreover, the size of the cavities was different throughout the NAIM system. It is evident from the size distribution studies of the cavities shown in Figure 55c. Size selectivity of the NAIM systems was studied in the plumbagin-based NAIM system, and it has been proven that the cavities selectively recognize NPs similar to the size and shape of the template NPs. In this case, the formation of concave-shaped doughnut cavities with upper rim diameter smaller than the size of the template PS NPs poses a challenge in selecting the correct size of analyte NPs. This is also why smaller analyte NPs were chosen for the uptake study. This limits the flexibility and uptake ability of the NAIM system.
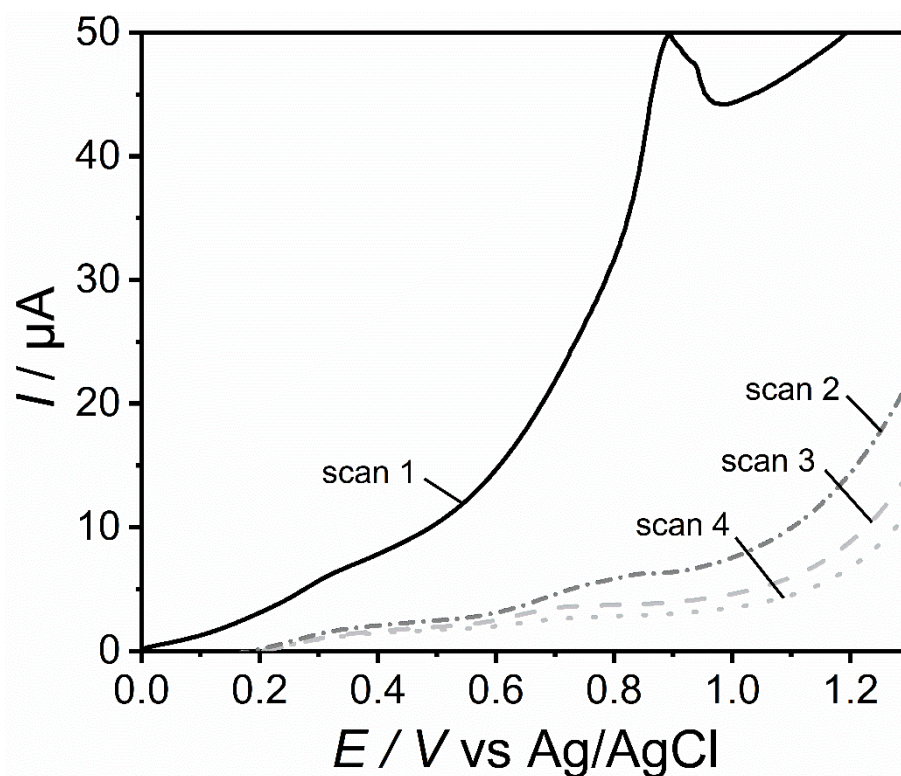
Figure 61. LSV curve in 3 M KCl at a scan rate of 0.05 V s$^{-1}$ obtained with *p*-pd/( )PDDA/ITO after exposing to 40 nm AuNP-Cit solution.

To study the aminopyridine-based NAIM system, different analyte NPs were used. Despite the presence of well-defined cavities, the broad size distribution of the cavities was of concern when selecting the size of analyte NPs. Initially, (55 ± 3) nm Au-Cit analyte NPs were chosen as the analyte NPs. The studies by SEM after the exposure to Au-Cit analyte NPs revealed the presence of a high density of non-specifically adsorbed NPs as observed in the PDA and *p*-pd-based NAIM systems. Figure 62a shows the SEM image of 3-AP/( )PDDA/ITO after the exposure to (55 ± 3) nm Au-Cit NPs. The citrate-modified Au-Cit NPs were replaced by (35 ± 3) nm amine-modified Au NPs (Au-NH$_2$), to study the aminopyridine-based NAIM system. This alteration was made to avoid the excessive non-specific adsorption of analyte NPs due to the interaction between the positive charge on the pyridine ring and the negative citrate groups on the surface Au. The studies by SEM after exposure to Au-NH$_2$ NPs revealed a surface with a considerably low density of non-specific adsorbed NPs, as expected. Few Au-NH$_2$ analyte NPs were found in the center of the cavities,

as shown in Figures 62b and c. An attempt to electrochemically address the NPs inside the cavities was unsuccessful due to the oxidation of the film in the given potential window. This makes it difficult to derive conclusions on the uptake ability of the 3-AP-based NAIM system.



Figure 62. SEM images of 3-AP/( )PDDA ITO after the exposure to a) 55 ± 3 nm Au-Cit NPs, b) and c) 35 ± 3 nm Au-NH$_2$ NPs.

# 7    Aryldiazonium-Based NAIM Systems

The requirement of a rigid and homogeneous matrix is crucial for the development of NAIM. The stability of matrices from heating, etchants, and different post-treatments is essential for the proper functioning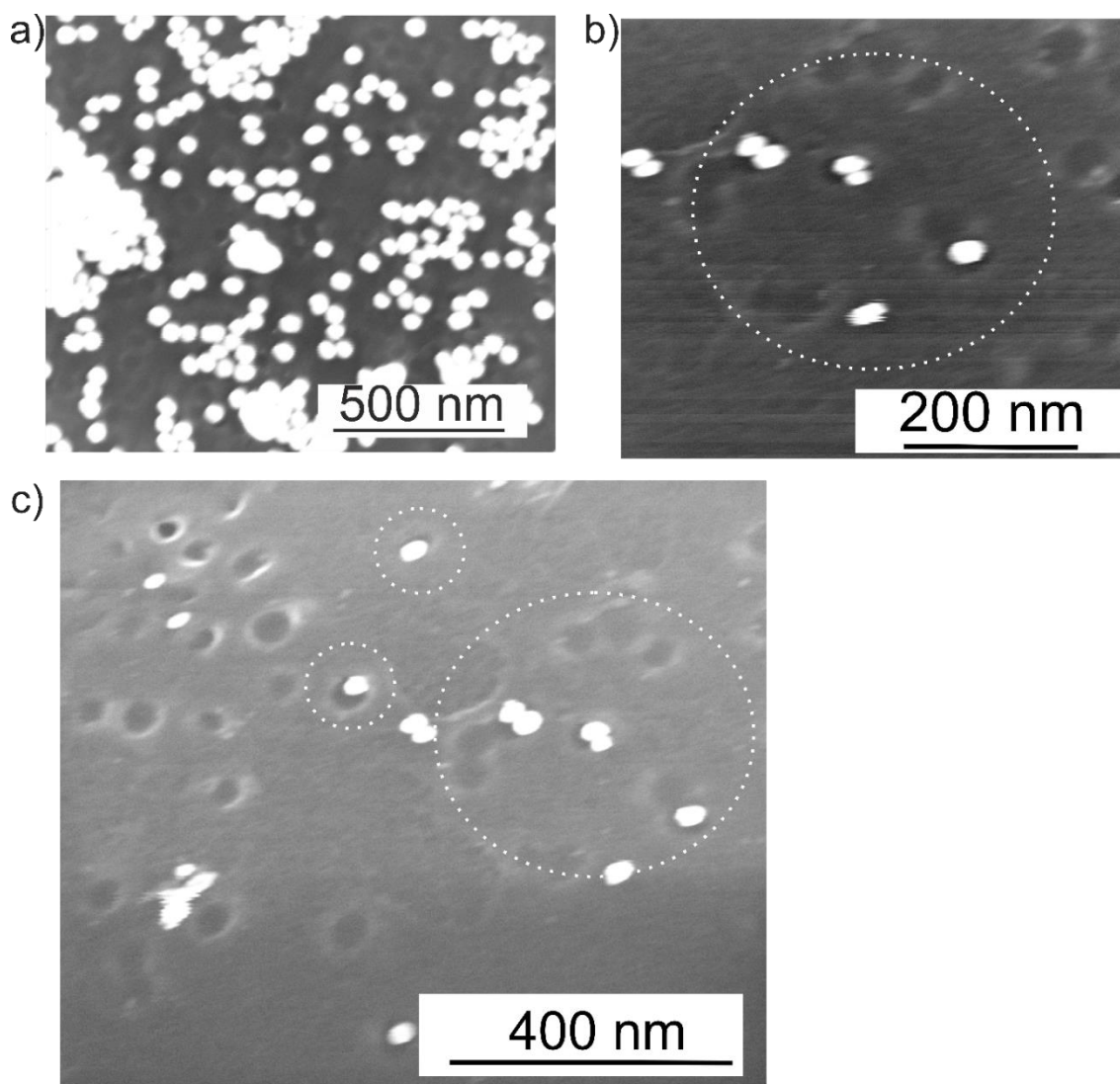 of such a system.[38,41,48] Diazonium salts, a group of organic compounds with the structure $RN_2^+X^-$, where R can be any alkyl or aryl group, and X is an inorganic or organic anion.[188] Aromatic diazonium salts, the compound of interest, are more stable than aliphatic diazonium salts due to the dispersion of their charge over the benzene ring.[188,189] Diazonium group ($N_2^+$), owing to its electron-withdrawing nature, readily undergoes dediazonation reactions to give an aryl cation ($Ar^+$) or aryl radical ($Ar^{\cdot}$).[190]

Electrografting aryl radicals can be achieved by its electrochemical reduction of aryl diazonium slats in an aprotic medium with supporting electrolyte (acetonitrile (ACN) + 0.1 M TBABF$_4$) or acidic aqueous medium (0.1 M H$_2$SO$_4$), where the cathode is set to the reduction potential or more negative potential of the diazonium salt using a potentiostat.[176,191] On reaction with the surface, diazonium compounds undergo homolytic dediazonation generating aryl radicals that react with the surface. Diazonium salts with different functional groups can be synthesized due to the versatility of aromatic rings, leading to modified surfaces with diverse functional groups like cyanides, halides, nitro, alcohols, alkyl, thiols, carboxylic, ester, and various bulky groups.[175]

Delamar et al.,[190] the pioneers in the study of surface modification by reduction of diazonium salts found that electroreduction of diazonium salts leads to a stable, non-corrosive covalent attachment of aryl groups onto the carbon surface. Electroreduction of 4-nitrobenzene diazonium salt in ACN resulted in a broad irreversible reduction peak at -0.04V (SCE) by a one-electron reduction yielding an anion radical. The nitrobenzene layer formed was stable for several months, substantiated by the single broad symmetrical signal as that of nitrobenzene observed after electrolysis of the modified GC electrode in a pure supporting electrolyte.[190]

The versatility of electrografting through the reduction of diazonium salts was investigated by Allongue et al.[192], who observed the attachment of solid films from various aryl radicals. Studies revealed that surface coverage depends on diazonium

salt concentration and electrolysis duration. Besides GC, highly ordered pyrolytic graphite (HOPG) was also modified by the electroreduction of diazonium salt, whose Raman spectra are similar to modified GC, except for the absence of the D band common in disordered carbon.[193]

The stability of the covalently attached layers has been studied and corroborated through various methods. The aryl layer-modified substrate remained stable even after six months of exposure to the atmosphere. Sonication in different solvents left the layer on the substrate, verified from the unchanged cyclic voltammetric signal.[192] Carbon nanotubes and mesoporous carbon modified with aryl layers showed thermal stability, where bond cleavage occurred at 300-500 °C.[194,195]

The electroreduction mechanism of diazonium salts is concerted, where cleavage of $N_2$ and radical formation co-occur, as in the case of aryl halides. The mechanism is detailed in Chapter 7.1. Unlike aryl halides, phenyl radicals formed by the reduction of diazonium cations spontaneously react with the surface, forming a layer. The reaction is self-limiting, and a multilayer of thickness ranging from a few nanometres to micrometres will be formed. Once a monolayer of the aryl group is formed, generated radicals will react with the aryl group of the first layer and grow to a multilayer. Electron transfer becomes difficult through thick layers and finally stops.[175] The thickness of the layer varies with the substrate,[196] potential[197], and techniques used for electrografting.[198]

## 7.1 Controlled Formation of Matrices by Reduction of ADS

The development of the NAIM systems requires a stable film with suitable thickness compatible with the size of the template and analyte NPs. Initially, nitrobenzene diazonium salts (NBD) were chosen as the precursor for advancing a new NAIM system based on electrografting from ADS.
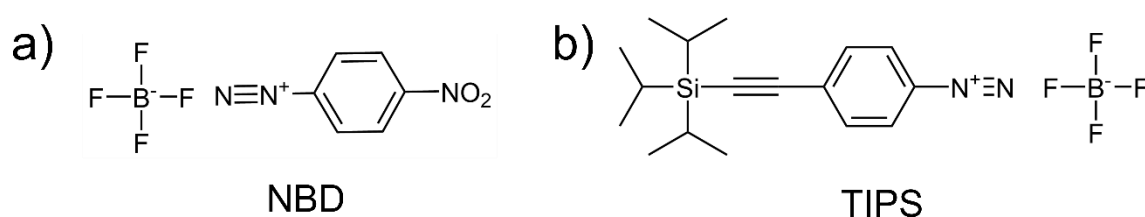


Figure 63. Diazonium salts used for the construction of the NAIM-System a) NBD (4-nitrobenzene diazonium [BF4]-) and b) TIPS (4-((triisopropylsilyl)ethynyl) benzene diazonium [BF4]-).

Electrografting of nitrobenzene diazonium salt is a process used to modify the surface of an electrode or substrate by covalently attaching nitrobenzene groups onto it. The electrografting of nitrobenzene diazonium salt allows for the creation of functionalized electrode surfaces with various applications, such as electrocatalysis,[199] corrosion resistance,[200,201] sensors[202,203], and electronic devices.[204] Nitrobenzene groups on the electrode surface can introduce specific chemical properties that can be exploited for targeted chemical reactions or surface interactions. Additionally, electrografting provides a stable and robust attachment of the nitrobenzene groups, allowing the modified electrode to be used in various electrochemical experiments.
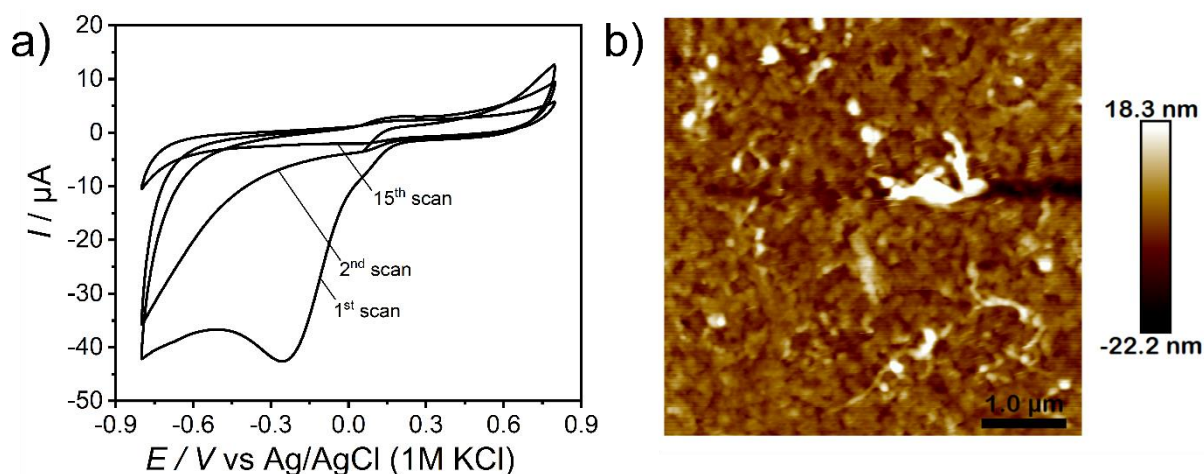


Figure 64. a) Cyclic voltammogram during grafting of NB onto ITO in 1 mM NBD + 0.1 M TBABF$_4$ in ACN at v = 0.05 V s$^{-1}$and b) AFM topography image of NB/ITO recorded in intermittent contact mode using an NCHV-A AFM tip ($k$ = 42 N m$^{-1}$).

The ITO substrate to be electrografted was cleaned and dried in the Argon stream, as explained in Chapter 4. The substrate was later subjected to modification via the electroreduction of 4-NBD. Figure 64a shows the 1st, 2nd, and 10th CV scans recorded during the electrografting of a 4-nitrobenzene layer. A broad peak around —0.25 V corresponds to the formation of the aryl radical. A decrease in the cathodic current in the successive scans following the first scan confirms the formation of an insulating nitrobenzene (NB) layer. When the topography of the electrografted NB film over ITO (NB/ITO) was studied by AFM, a non-homogeneous film was observed.

Figure 64b shows the topography image of NB/ITO, which reveals cauliflower-like features. The cauliflower-like growth of the NB film was witnessed in different areas of the ITO. The topography studies corroborate that the growth of NB film is irregular and unstable, forming a heterogeneous film unsuitable for the NAIM system.

Kariuki et al.[205,206] have studied the electrochemical modification of carbon electrodes with aryl film and confirmed the multilayer growth of film with a thickness of approximately 20 nm with the aid of AFM. The layer growth leading to the heterogeneity of the NB films might be due to a) the electrophilic attack of dediazonated aryl carbocations or b) the attack of an aryl radical onto the grafted aryl moieties,[177,205,206] as shown in the mechanism in Figure 65. The latter mechanism was confirmed by FT-IR studies by Kariuki et al.[205] Without precautions, these mechanisms lead to films that are too rough to adjust the thickness of the NAIM system.
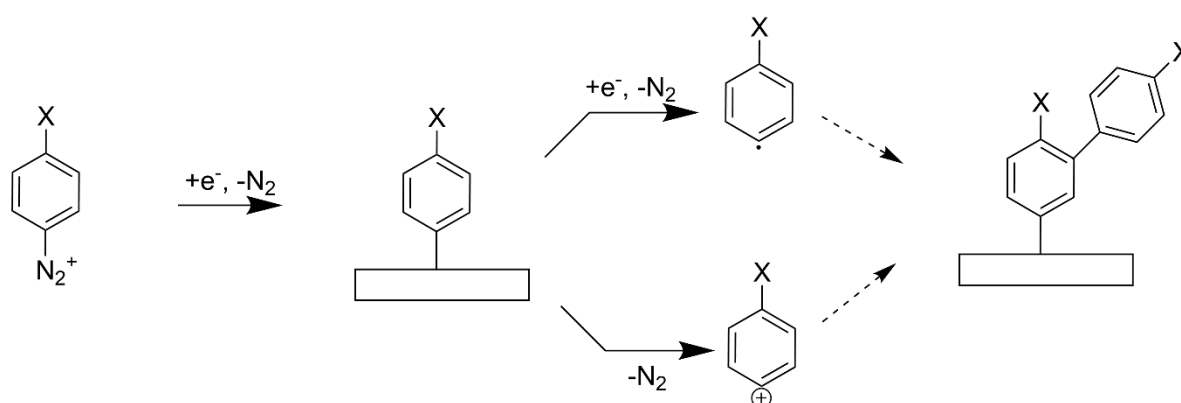


Figure 65. Proposed mechanisms for the multilayer formation during the electrografting of NBD.

Although electrografting of diazonium salts is a versatile method allowing to graft different functional groups on the substrate surface, the resulting disordered film is a significant drawback. However, on carefully controlling the charge during the electrochemical reduction of the ion, an organized monolayer on atomically flat H-terminated Si(111) substrate was obtained.[207] Likewise, AFM studies substantiated the formation of a dense, homogeneous, and thin film of 4-nitrophenyl groups on the surface of pyrolized photoresist films (PPFs) on controlling the electrografting conditions.[208,209] Combellas et al.[210,211] have used sterically hindered diazonium salts for controlled electrografting. Sterically hindered diazonium salts refer to diazonium

salts with bulky substituents, which are typically large and hinder access to the different sites of the diazonium ion. A thin layer close to a monolayer was formed when 3,5-bis-tert-butyl benzene diazonium salts were used for electrografting.[211] This is due to the presence of bulky substituents on the initially grafted layer, which hinders the access of other radicals to attack the grafted layer and either prevents or slows down the formation of the multilayer.[211]

Considering that sterically hindered diazonium salts can promote dense, uniform, and thin film formation on various substrates, Leroux et al.[102] exploited triisopropylsilyl (TIPS)-protected ethynyl aryldiazonium salt for forming a stable, controlled organic layer on the carbon substrate. The TIPS group provides steric hindrance and protects the aryl groups from further attack by the aryl radicals in the solution. The resulting covalently modified carbon surface contains the desired TIPS-protected ethynyl aryl functionality, which can be further functionalized through click chemistry or can be utilized for binary layer formation. This process enables controlled and efficient modification of carbon or metal surfaces with tailored organic layers, which find applications in sensors, catalysis, and biomedical devices.[102,212]

Building upon the previous studies, we used the electroreduction of 4-((triisopropylsilyl)ethynyl) benzene diazonium salt (TIPS, Figure 63b) for the formation of a controlled matrix, a requisite for the NAIM system. The compound TIPS was synthesized according to Leroux et. al.[102]., which was detailed in section 4.6.3. An organic layer was electrografted on a cleaned ITO by the electroreduction of TIPS. Figure 66a shows the corresponding cyclic voltammogram for the electrografting of TIPS on ITO (TIPS/ITO). A peak at -0.38V is related to the formation of the TIPS aryl radical. A decrease in the cathodic current in the successive scans following the first scan signifies an insulating TIPS layer formation. The topography and the thickness of the deposited layer were studied using AFM in intermittent contact and contact modes, respectively. Figure 66b shows the AFM image of the TIPS layer grafted on the ITO. The roughness of the TIPS film on ITO was measured to be 2.5 nm from an area of 1 μm x 1 μm, where the roughness of bare ITO from an area of 1 μm x 1 μm was measured to be 2.45 nm. The TIPS film grafted on ITO from 5 potential cycles revealed a 2 to 3 nm film thickness.

Leroux et al.[104] explored the prospect of binary film design by a subsequent electrografting of NBD on TIPS-modified GC. The presence of pinholes in the initial

grafted film allows the grafting of a second layer forming a structured surface. This preserved the homogeneous film morphology. In our work, we explored the binary film design by electrografting a second layer of NB by the electroreduction of NBD over TIPS/ITO. The sample can be abbreviated as NB/TIPS/ITO. The corresponding CV for the electrografting of NB is given in Figure 66c.

AFM studies of NB/TIPS/ITO revealed the presence of a homogeneous and smooth film of roughness 3.1 nm measured from an area of 1 μm x 1 μm. The thickness studies on the sample confirmed an increase in the thickness of the film ranging between 9-10 nm. This also ensures a slow growth of the NB layer over TIPS/ITO. Figures 66d and 66e show the topography and thickness studies of NB/TIPS film on ITO.

The response of electrodes at different stages towards ferrocene methanol (FcMeOH) as a redox probe was studied to analyze the modifications. The well-developed quasi-reversible redox peaks corresponding to $Fc/Fc^+$ were obtained on the bare ITO (peak 1, Figure 67). Cyclic voltammograms obtained after modifying the ITO surface with the primary layer of TIPS reveal a decrease in the anodic and cathodic peak currents (peak 2, Figure 67). This exhibits a partial blockage of the ITO electrode. In similar studies, when conducted on the NB/TIPS/ITO (peak 3, Figure 67), a complete inhibition of the redox peak currents confirmed the formation of a defect-free homogeneous film.
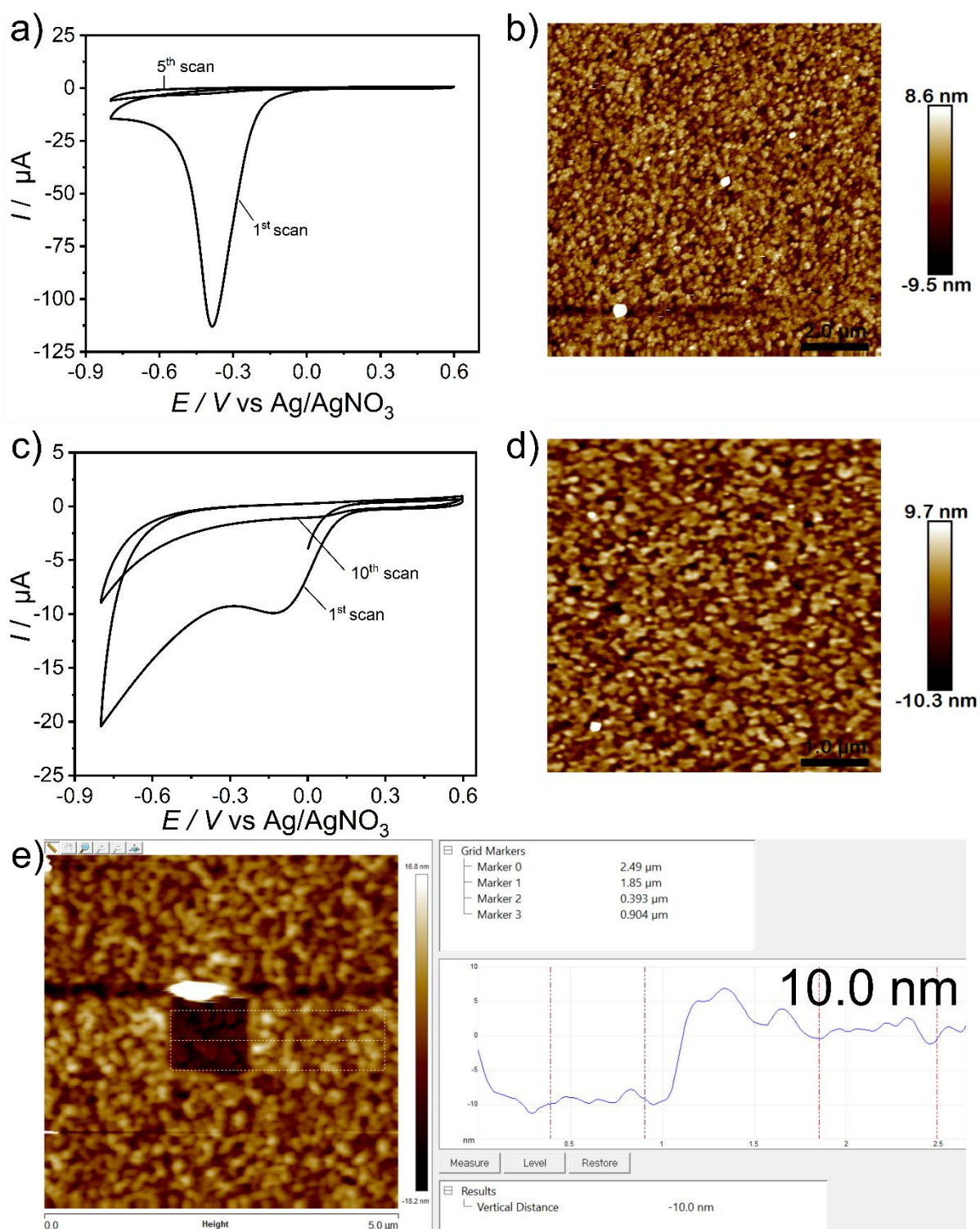
Figure 66. a) Cyclic voltammogram during grafting of TIPS onto ITO in 1 mM TIPS + 0.1 M TBABF$_4$ in ACN at $v$ = 0.05 V s$^{-1}$; b) AFM topography image of TIPS/ITO recorded in intermittent contact mode using an NCHV-A AFM tip ($k$ = 42 N m$^{-1}$); c) cyclic voltammogram during grafting of NB onto TIPS/ITO in 1 mM NBD + 0.1 M TBABF$_4$ in ACN at $v$ = 0.05 V s$^{-1}$; d) AFM topography image of NB/TIPS/ITO recorded in intermittent mode using an NCHV-A AFM tip ($k$ = 42 N m$^{-1}$), and e) AFM thickness determination of electrografted NB/TIPS layer on ITO in contact mode using an MSCT AFM tip ($k$ = 0.6 N m$^{-1}$).
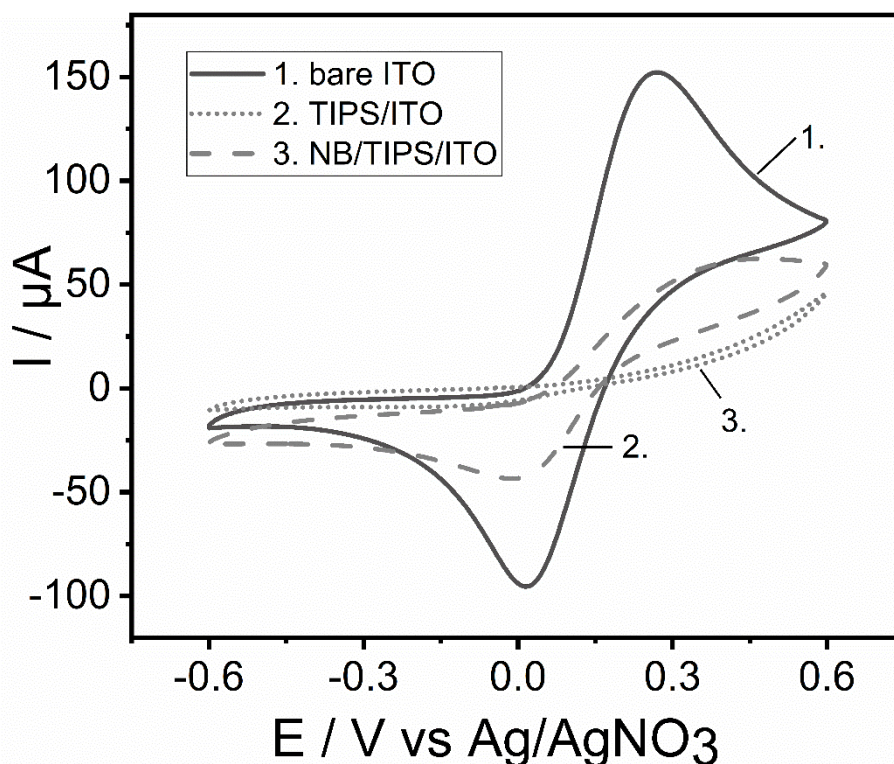
Figure 67. Redox probe studies at 1) bare ITO, 2) TIPS/ITO, and 3) NB/TIPS/ITO in 1 mM FcMeOH + 0.1 M TBAPF$_6$/ACN at 0.1 Vs$^{-1}$.

The substrates were examined using XPS after the electrografting of TIPS and NB layers. The Si 2p and N 1s XP spectra of ITO modified with TIPS/NB are shown in Figure 68a and 68b, respectively. The Si 2p signal at 100.5 eV can be assigned to Si within the the TIPS protection group.[212] The Si 2p signal at 101.8 eV might be due to the formation of oxidized species.[212] The N 1s spectra recorded after the electrografting of the NB layer over TIPS/ITO displays three peaks. The nitro (NO$_2$) groups exhibit a peak around 405.7 eV, confirming the electrografting of the binary NB layer.[192,213–215] The peaks around 399.8 eV and 402 eV could be due to the partial reduction of nitro groups of NB.[213–215] The investigation of the NB/TIPS film on ITO using CV, AFM, and XPS confirmed the presence of a homogeneous, defect-free, and smooth film, as required for the NAIM system.
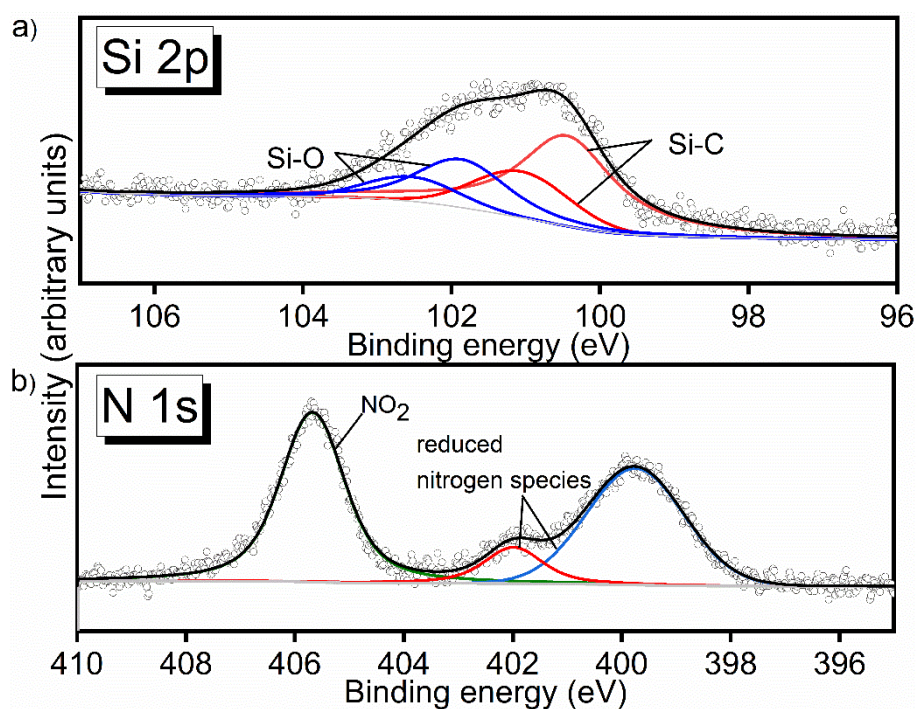
Figure 68. a) Si 2p and b) N 1s spectra after electrografting NB/TIPS layer over ITO.

For the development of the NAIM system, the initial step involves the adsorption of a positively charged primer layer, PDDA, chemisorbed on the surface of cleaned ITO substrate (PDDA/ITO). The presence of a PDDA layer on ITO attracts negatively charged carboxyl functionalized $SiO_2$ NPs ($SiO_2$-COOH) of size 20 nm diameter. Figure 69a shows the SEM images of PDDA/ITO after exposure to $SiO_2$-COOH NPs for 2 h. Followed by the modification with template $SiO_2$-COOH NPs, the surface was subjected to electrografting of the NB/TIPS binary layer. SEM images after the electrografting process confirm the presence of $SiO_2$-COOH NPs, unaffected during the electrografting process (Figure 69b). Following the concept of orthogonal removal techniques for template and analyte NPs, the $SiO_2$-COOH template NPs were etched by exposure to an aqueous 5 % HF solution for 3 min, which removed the NPs. The removal of template NPs was confirmed by SEM imaging.
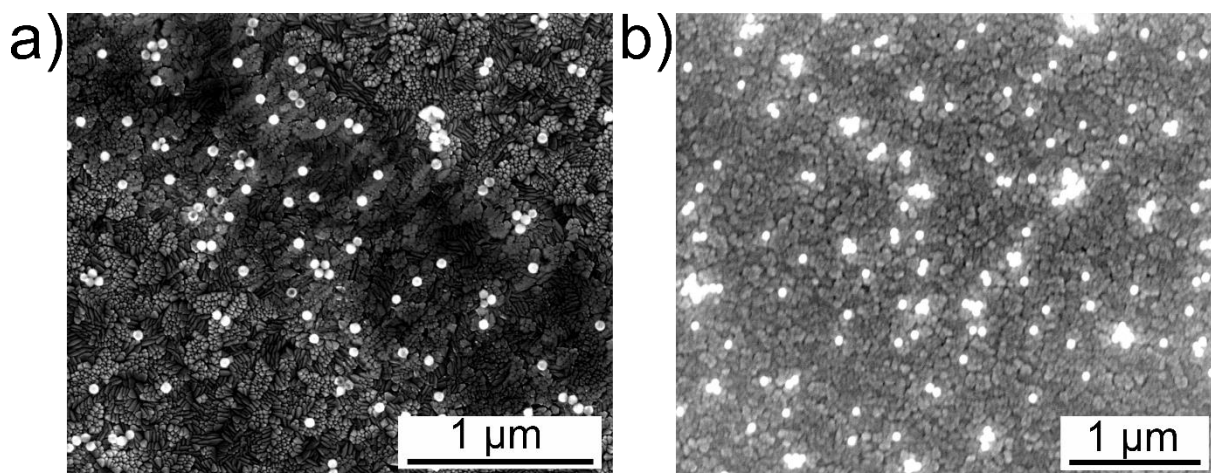
Figure 69. SEM images after a) the attachment of SiO$_2$-COOH NPs on PDDA-modified ITO and b) the electrografting of NB/TIPS layer over (SiO$_2$-COOH)PDDA/ITO.

Cavities complimentary to the used template NPs were visible in the SEM images, after the removal of SiO$_2$-COOH NPs (Figures 70a and 70b). The size of the cavities was measured to be (21 ± 3) nm using ImageJ software, and the corresponding size distribution studies are given in Appendix B1. The sample at this stage can be abbreviated as NB/TIPS/( )PDDA/ITO. The brackets indicate the cavities formed after the removal of template NPs. The cavities could take up citrate-protected Ag NPs (Ag-Cit) when exposed to 20 nm citrate-protected Ag NPs (Ag-Cit). The film is abbreviated as (NB/TIPS/(Ag-Cit)PDDA/ITO). The analyte NPs could be detected by LSV in 0.1 M NaNO$_3$ solution by an oxidation peak at 0.23 V (Figure 70c). The uptake was relatively low.

Nevertheless, the studies on the system were unsatisfactory due to the lack of stability of ITO and the NB/TIPS matrix during the short exposure to HF. The damage of the matrix film during the brief exposure to HF causes the film to be removed from irregular parts of the sample, as detected by visual appearance and by XPS. The XPS studies of NB/TIPS/(SiO$_2$-COOH)PDDA/ITO before and after exposure to HF are given in Figure 71. The C 1s and N 1s signals in Figure 71a originate from the electrografted film, while Si 2p and O 1s peaks are possibly from the electrografted film, SiO$_2$-COOH NPs, and the underlying ITO substrate. Figure 71b shows the survey scan of the same sample after exposure to HF. The appearance of In 3d and Sn 3d peaks corresponding to the ITO substrate and the decrease in the intensity of N 1s and C 1s peaks from the NB/TIPS film confirmed the partial removal of the film after exposure to HF.
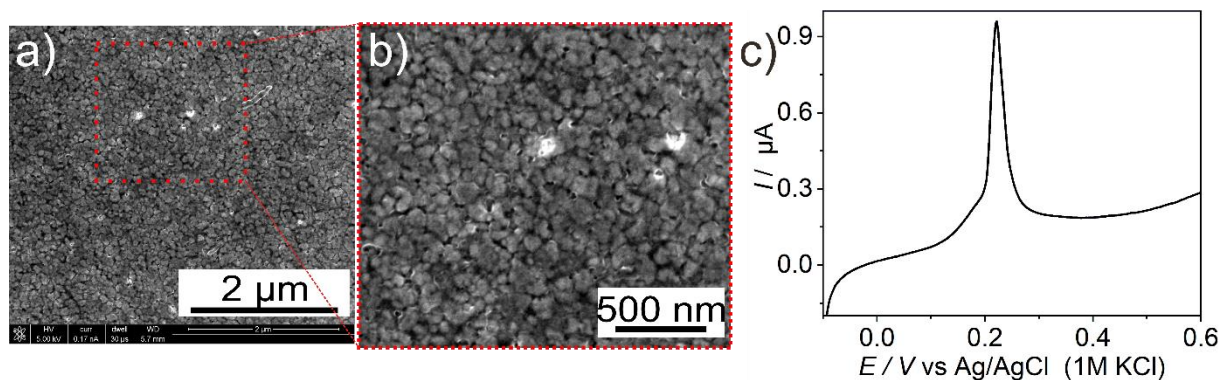
Figure 70. SEM image of NB/TIPS/( )PDDA/ITO after the removal of template $SiO_2$-COOH NPs, b) enlarged area of the selected region, and c) LSV curve in 3 M KCl at $v$ = 0.05 V s$^{-1}$ for Ag-Cit NP dissolution from NB/TIPS/(Ag-Cit)PDDA/ITO.
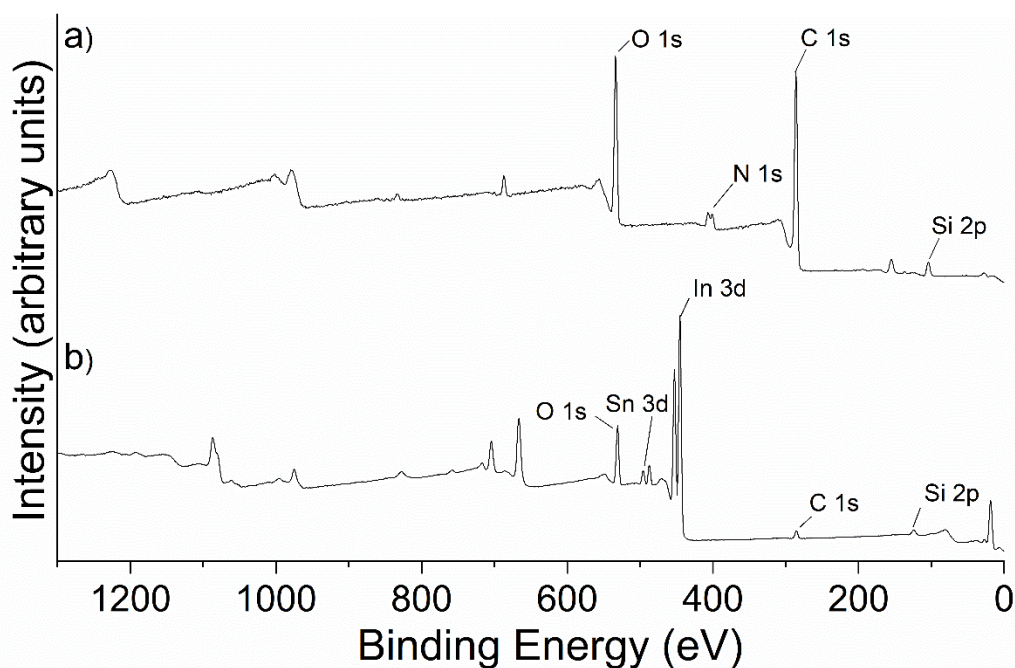


Figure 71. XPS survey scan of NB/TIPS/($SiO_2$-COOH)PDDA/ITO a) before and b) after exposure to 5 % HF for removing $SiO_2$-COOH NPs.

The exposure of modified ITO to remove the template NPs introduce cavities in the NAIM system, thereby exposing the ITO surface. Aqueous HF can reach the ITO through the cavities and probably cause the under-etching of ITO, as shown in the schematics in Figure 72a. This can affect the electrografted NB/TIPS layers on the ITO surface and probably remove the layers on the top of the affected region of ITO. When

bare ITO was exposed to HF briefly, the difference in the surface morphology can be observed in Figures 72b and 72c. Another drawback of this system was the need for an easy opportunity to adjust the chemical functionalities within the film to different ligand shells of the analyte NPs. Despite the formation of well-controlled film, the NAIM system was not studied further due to the limitations explained before.
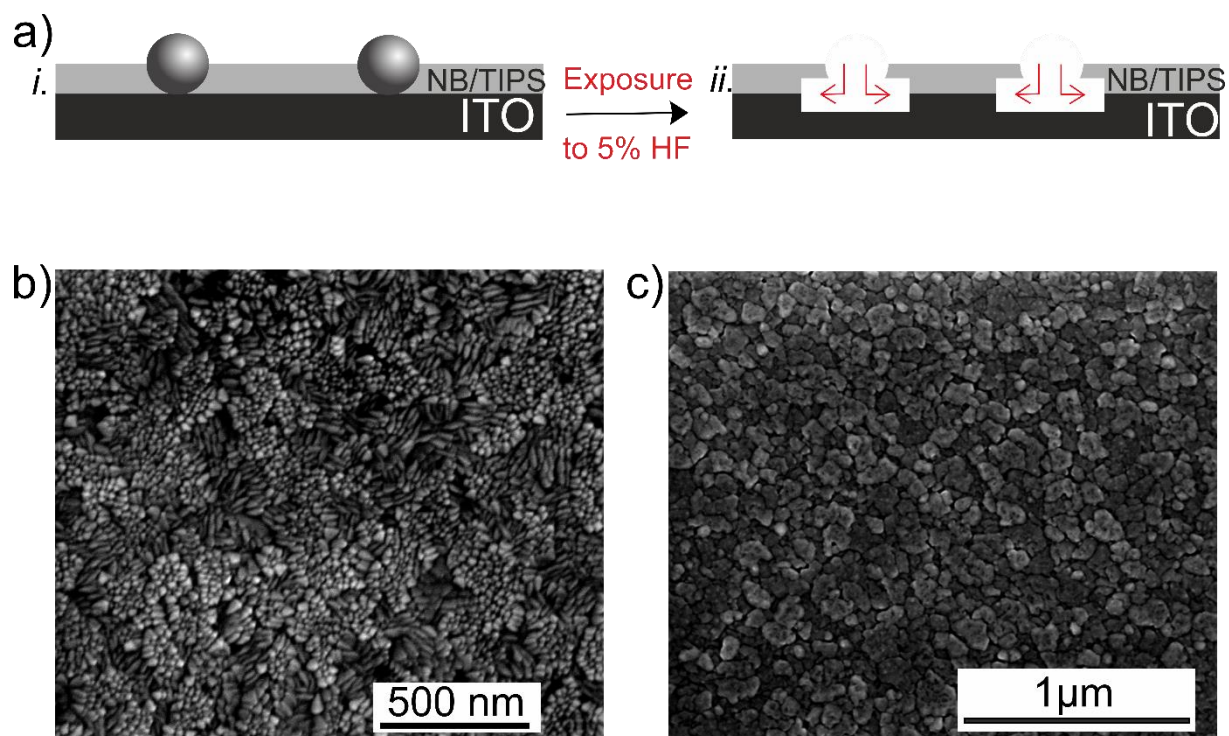


Figure72. a) Schematics showing under-etching of ITO on exposure of NB/TIPS/(SiO$_2$-COOH)PDDA/ITO to 5 % HF; SEM images of bare ITO b) before and c) after exposure to 5 % HF.

## 7.2   Matrices from Electroreduction of In Situ Generated ADS

New NAIM systems were prepared from aromatic amines with further functional groups. Figure 73 shows the chemical structures of the aromatic amines used to synthesize diazonium salts. The diazonium salt is generated in situ by reacting an aromatic amine with NaNO$_2$.[101,105,178] The substrate, often a conducting material, is immersed in the diazonium salt solution, followed by applying a suitable electric potential between the substrate (working electrode) and a counter electrode in an electrochemical cell. The diazonium cations are reduced to radicals at the working

electrode surface, which react with the surface to form covalent bonds, grafting the organic layer onto the substrate.

### 7.2.1 Electrografting from In Situ Generated Diazonium Salts

Grafting an organic layer derived from 3-diazo pyridinium cations onto a substrate through electrografting can introduce specific functional groups to the surface. This modified surface can exhibit new properties, such as enhanced chemical reactivity, improved adhesion, altered wettability, or tailored electronic properties. Also, the aminopyridine-modified surface can act as an anchor for the attachment of different metallic ions or other functional groups.[216,217] The modification with 3-diazo pyridinium cations on the substrate material will influence the final characteristics of the modified surface. The complexation ability of the pyridinium layer on the GC electrode was studied by Yesildag et al.[218] The pyridinium layer offers many ligand sites and was used for the formation of organometallic films by coordination with different metals.
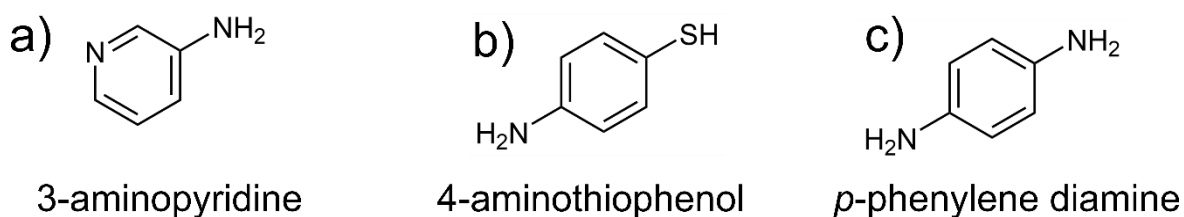


Figure 73. Amines for preparation of diazonium salts used to construct the NAIM-System a) 3-aminopyridine, b) 4-aminothiophenol, and c) *p*-phenylene diamine.

According to Agullo et al.[178], a stable and homogeneous pyridinium layer can be electrografted on a GC substrate. The grafting time and potential have a direct impact on the grafting efficiency. With more grafting time, more coverage of the pyridinium layer on glassy carbon can be obtained. Likewise, an increase in the amine concentration also improves the coverage of the pyridinium layer, but excess $NaNO_2$ can decrease the grafting efficiency.[178] The proposed mechanism of electrografting of in situ generated diazonium salts is given in Figure 74a.

114
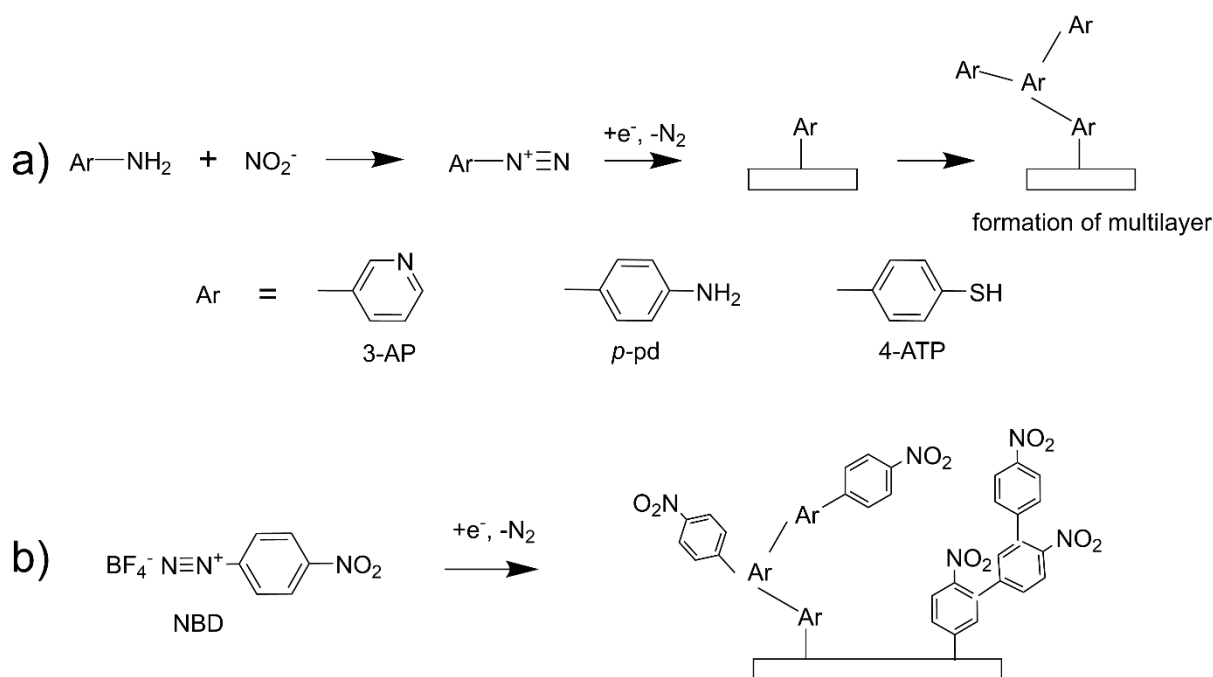
Figure 74. Proposed mechanism for the a) grafting from the reduction of in-situ formed diazonium salts and b) overgrowing with another layer of NB to limit the non-specific adsorption of analyte NPs.

Here, a cleaned GC was used as the substrate for the studies. The GC substrate, after cleaning, was immersed in a solution of in situ-generated 3-diazopyridinium cations and a potential of 0.8 V vs Ag/AgCl was applied for 10 s and the GC electrode was once cycled in the same solution. Appendix B3a and Appendix B3b show the corresponding chronoamperogram and cyclic voltammogram. A monolayer thick layer of 3-amino pyridinium cation (3-AP$^+$) was formed on the GC substrate, which was used as the primary layer for the attachment of negatively charged SiO$_2$-COOH template NPs of 40 nm. The sample at this stage can be abbreviated as (SiO$_2$-COOH)3-AP$^+$/GC. After this step, the actual matrix of 3-AP$^+$ was built by first performing the in-situ formation of diazonium salts and their grafting once more with 3-AP$^+$, but this time for more cycles to obtain a thicker layer. The sample will be referred to 3-AP$^+$/(SiO$_2$-COOH)3-AP$^+$/GC for brevity. This was followed by a similar step using 4-nitrobenzene diazonium salt. The second layer was intended to overgrow the first layer to cover the pyridine groups at the film-solution interface to prevent the non-specific adsorption of the analyte NPs in a later step, as shown in Figure 74b. Appendix B3c and B3d shows the cyclic voltammogram corresponding to the electrografting of 3-AP$^+$ and NB. SEM image of (SiO$_2$-COOH)3-AP$^+$/GC after forming

the thicker matrix is given in Figure 75a. After subsequent removal of the template NPs, only the cavities should expose pyridine rings, with which the citrate–protected Au or Ag NPs could interact. The thickness of the NB/3-AP$^+$ film was measured to be around 10.0 nm using AFM (Appendix B2).

The exposure of NB/3-AP$^+$/(SiO$_2$-COOH)3-AP$^+$/GC to 5 % HF removed the template SiO$_2$-COOH NPs. The removal of the template NPs was confirmed by SEM (Figure 75b). No cavities were observed in the SEM images. Subsequent exposure to solutions of citrate-protected Au nanoparticles of 25 nm showed a strongly reduced extent of non-specific adsorption. However, the specific adsorption was also reduced compared to other NAIM systems. While a few analyte nanoparticles could be detected in SEM, their density was insufficient to generate an analytical signal in LSV. Figures 75c and d show the SEM images and LSV studies after the uptake of Au-Cit NPs.

The film composition was varied by forming the matrix from 4-amino thiophenol (ATP) or $p$-phenylene diamine ($p$-pd) as a precursor for the in-situ formation of the diazonium salts.[105] Grafting an organic layer derived from ATP or $p$-pd onto a substrate through electrografting can introduce specific functional groups to the surface, which was expected to interact with the ligand shell of the analyte NPs, improving the uptake. After the attachment of SiO$_2$-COOH NPs on a PDDA-modified GC, the films were electrografted to form an organic layer of either ATP or $p$-pd. The corresponding samples are denoted as ATP/(SiO$_2$-COOH)PDDA/GC and $p$-pd/(SiO$_2$-COOH)PDDA/GC and had suitable thicknesses of 11-13 nm and 10-12 nm, respectively (Appendix B2).

After removing template NPs, the samples were exposed to analyte Au-Cit NPs with a diameter of 25 nm. These films could uptake citrate-protected Au-Cit NPs, as seen by SEM and by electrooxidation peak (marked in the red box) in the LSV scan at 0.99 V vs Ag/AgCl. (Figure 76). However, a rising background current can be observed in a similar potential range, where the oxidation of Au-Cit NP is expected. This makes it difficult to distinguish the oxidation curve from the background current.
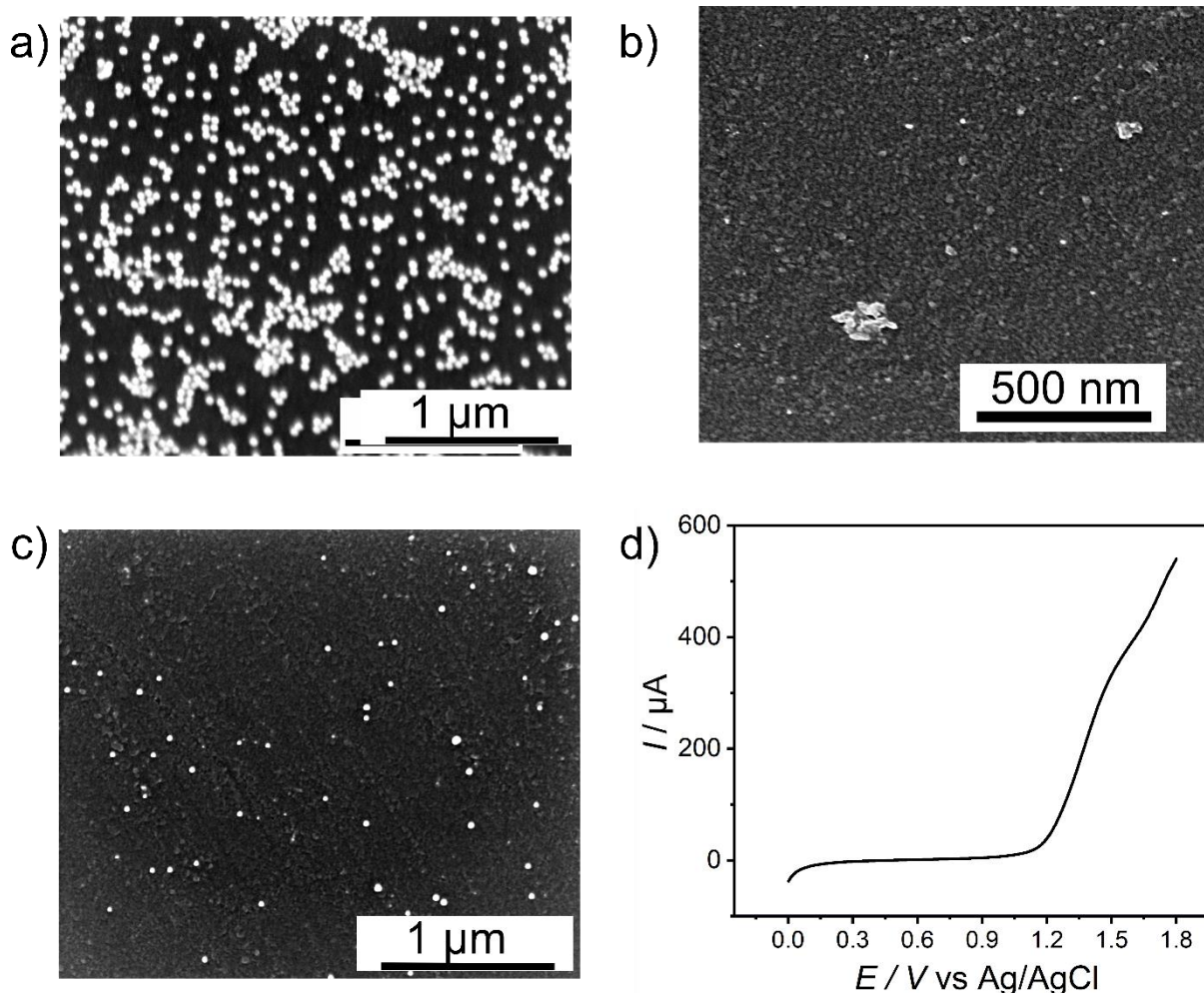
Figure 75. SEM images a) of SiO$_2$-COOH modified PDDA/GC after the electrografting of 3-AP$^+$, b) after the removal of SiO$_2$-COOH NPs, c) after the exposure of 3-AP$^+$/( )3-AP$^+$/PDDA/GC to Au-Cit analyte NPs and d) LSV curves in 3 M KCl at $v$ = 0.05 Vs$^{-1}$ for Au-Cit NP dissolution from 3-AP$^+$/(Au-Cit)3-AP$^+$/PDDA/GC.

Correspondingly, another problem occurred during the electrografting of ATP or *p*-pd. During the electrografting process, unexpected additional peaks were observed, as shown in Appendix B4a-d. Extensive but finally unsuccessful attempts were made to avoid their appearance by variation of the substrate cleaning procedures, potential scan ranges, scan rates, and solution concentrations. This made it challenging to reproduce similar electrografted films for further studies.
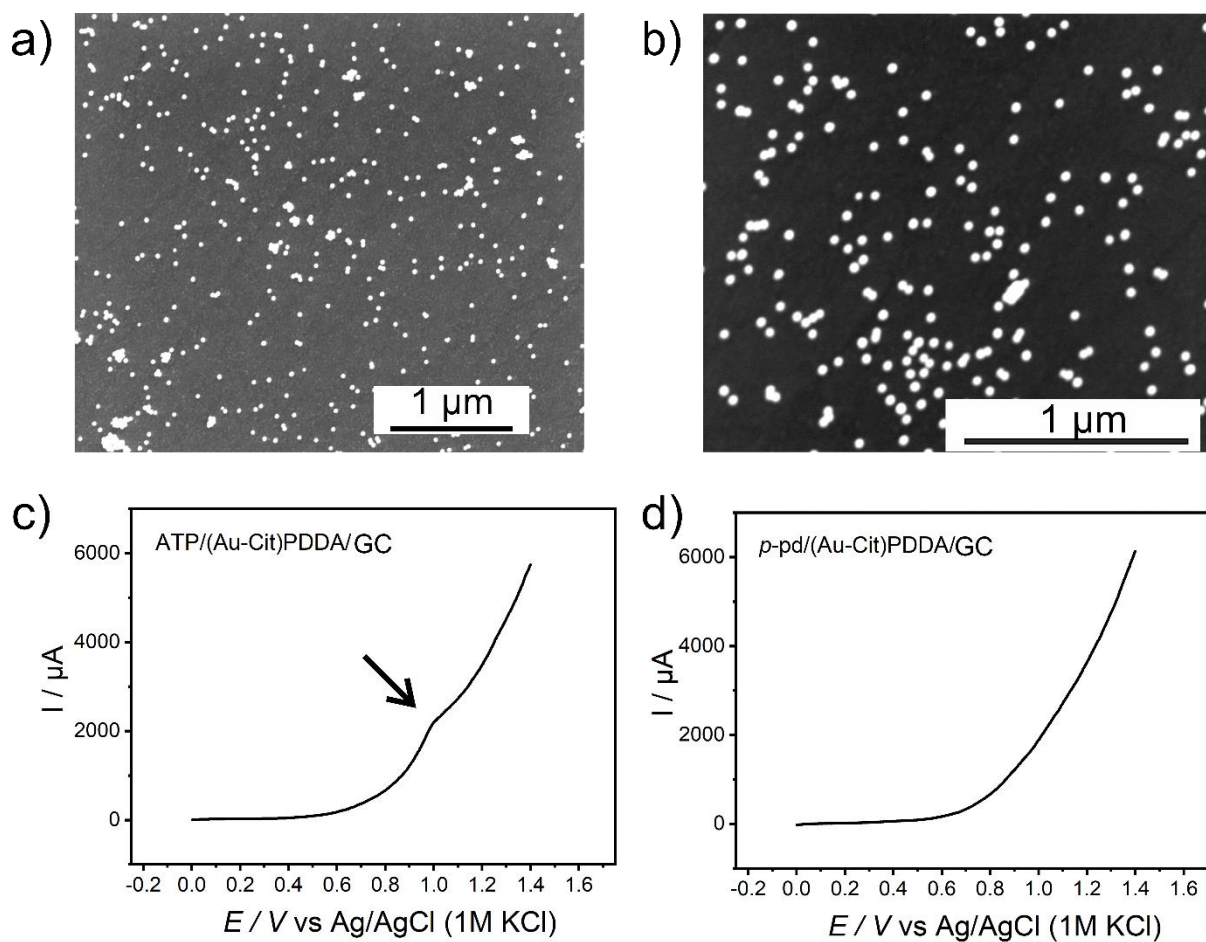
Figure 76. SEM images of a) ATP-modified GC b) PDD-modified NAIM system after the uptake of Au-Cit analyte NP; LSV curves in 3 M KCl at $v = 0.05$ Vs$^{-1}$ for Au-Cit NP dissolution from c) ATP-modified NAIM system and d) $p$-pd modified NAIM system.

118

# 8    SUMMARY AND OUTLOOK

The thesis aimed to develop NAIM systems with flexible tuning of functional groups, overcoming challenges in maintaining cavity shape, and able to selectively recognize different NPs. NAIM systems have selective binding sites within the matrix, facilitating the recognition of specific NPs, and contributing to advancements in targeted recognition and separation technologies. This chapter provides a summary of the developed NAIM systems, highlights the findings, and presents an outlook for future studies.

The first NAIM system presented in this thesis is the plumbagin-based NAIM system, detailed in Chapter 5. Here, three distinct NAIM systems were designed to investigate the influence of matrix modifications on NAIM selectivity. The ability for post-modification of the plumbagin-based matrix deposited on an activated GC substrate allows for the inclusion of various functional groups into the NAIM system. These groups can aid in the recognition process between the NAIM system and the analyte NPs. Covalent modification of polyplumbagin matrix with cysteamine or 1,2-ethanedithiol demonstrated the advantage of this approach. The matrix modified by cysteamine exhibited the highest uptake at pH 5, attributed to interactions between protonated amino groups of cysteamine and citrate groups on Au-Cit NPs, while the dithiol-modified matrix showed the highest uptake at pH 10.

The pH level significantly impacted the recognition ability, with the dithiol-modified matrix showing five times higher uptake efficiency at pH 10 compared to pH 5. This difference is attributed to the formation of more thiolate anions in an alkaline solution, enhancing interaction with Au-Cit NPs. Covalent matrix modifications had a notable effect on the recognition ability of the NAIM systems, as the introduced functional groups allowed for diverse interactions like electrostatic, hydrogen bonding, or covalent bonding with the matrix.

Furthermore, the size matching of analyte and template NPs played a crucial role in NAIM selectivity, with high uptake efficiency observed when analyte NPs and template NPs were within the same size range. This investigation highlights that by employing an insulating template NP with a core material such as $SiO_2$, it is possible to prevent the overgrowth of the matrix, leading to the formation of a well-defined cavity. The findings propose a method for the post-modification of the matrix, improving the uptake process and providing flexibility in the development of the NAIM system.

Chapter 6 provides an account of the development of other NAIM systems, employing PS NPs as the template NPs. The process involves coating the ITO substrate with a positively charged PDDA layer, which then attracts negatively charged template sulfate-modified PS NPs. Subsequently, a polymer matrix of polydopamine is electrodeposited from dopamine, and

it contains functional groups like amine, imine, and catechol beneficial for selective recognition process.

However, the overgrowth of the polydopamine film over PS NPs leads to the formation of doughnut-shaped cavities in the NAIM system. This overgrowth complicates the removal of PS NPs, requiring prolonged exposure to toluene and affecting the reproducibility of the system. The study explores other polymer films like *p*-phenylenediamine and polyphenol to address the overgrowth issue. Doughnut-shaped cavities persist in these cases as well, and the formation of irregularly shaped cavities is observed by SEM and AFM. The matrix, created through electrografting 3-aminopyridine exhibited well-defined cavities, as evidenced by SEM and AFM. Upon investigating the recognition capabilities of the NAIM systems, both the polydopamine-based NAIM system and the *p*-phenylene diamine-based NAIM system demonstrated size-selective uptake, as confirmed by LSV studies. The demonstrated uptake ability was relatively low due to the non-uniform cavities. Despite the presence of well-defined cavities in the 3-aminopyridine-based NAIM system, the LSV study resulted in the oxidation of the film in the given potential window. Drawing accurate conclusions about the uptake ability of these NAIM systems is challenging due to these limitations.

In Chapter 7, an alternative method for constructing NAIM systems, focusing on the electrografting of aryl diazonium salts is discussed. The NAIM system discussed here involves initially forming a positively charged PDDA primer layer on ITO, followed by attaching 20 nm $SiO_2$-COOH NPs. Subsequently, a matrix is electrografted from 4-((triisopropylsilyl)ethynyl)benzenediazonium tetrafluoroborate (TIPS), and 4-nitrobenzenediazonium tetrafluoroborate (NBD) is electrografted over the initial TIPS film to produce a 10 nm thick film. Template $SiO_2$-COOH NPs are then removed from the NAIM system through brief exposure to 5% HF, as confirmed by SEM, which verifies the cavity formation and complete removal of the template NPs. The system is later exposed to 20 nm Ag-Cit NPs for uptake studies, revealing relatively low uptake as detected by LSV. An XPS study before and after template NP removal confirms partial film removal during the short exposure to HF, possibly due to the penetration of HF through the cavities reaching the ITO substrate, causing under-etching of the substrate.

In section 7.2, matrices with useful functional groups were deposited through the electroreduction of aryldiazonium salts generated in situ on a GC substrate. The matrices subjected to the study are deposited from the diazonium salts of *i)* 3-aminopyridine and 4-nitrobenzene *ii)* *p*-phenylene diamine and *iii)* 3-aminothiophenol. After the removal of template $SiO_2$-COOH NPs, samples were exposed to analyte Au-Cit NPs. These films exhibited the uptake of Au-Cit NPs, evident through SEM and an electrooxidation peak in the LSV scan. However, the presence of a rising background current in a similar potential range, where the

oxidation of Au-Cit NP is expected, posed a challenge in distinguishing the oxidation curve from the background current. Additionally, unexpected peaks were observed during the electrografting of 3-aminothiophenol or *p*-phenylene diamine, creating difficulties in reproducing similar electrografted films for further studies despite various attempts to mitigate their appearance through procedural variations.
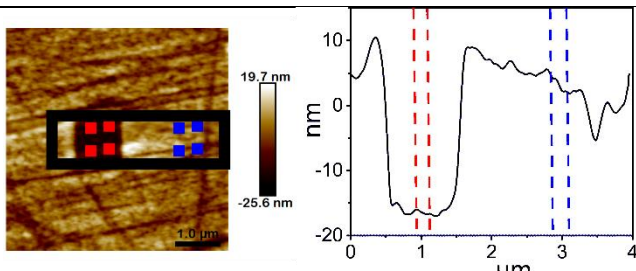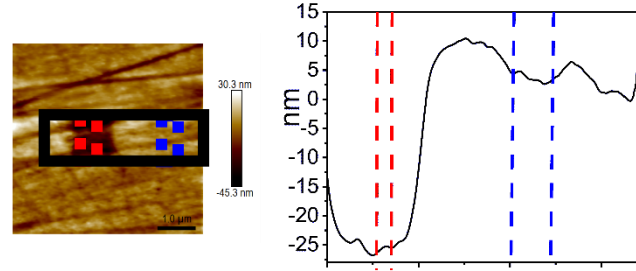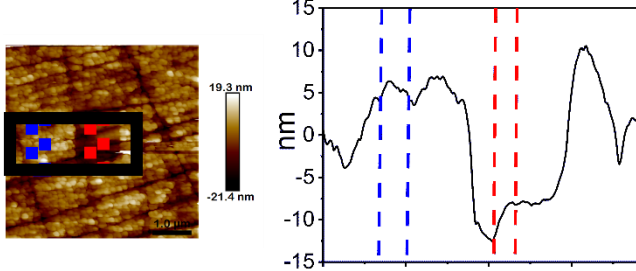
The efficiency of the NAIM system studied in this thesis relies significantly on the careful selection of template NPs, matrix material, and analyte NPs. The advantageous aspect of introducing functional groups into the matrix that are complementary to the analyte NPs effectively contributes to selective recognition, especially when the size of the template and analyte NPs are in the same range. Through careful matrix selection, an opportunity arises to adjust the matrix properties, leading to significantly improved recognition capabilities. However, additional flexibility is necessary to expand the system to accommodate analyte NPs that lack electrochemical activity. This might be feasible through the incorporation of responsive materials within the imprinted matrix. These materials are triggered by changes in their environment, such as changes in conductivity or colour in response to interactions with insulating analyte NPs. The monitoring of these alterations can then function as an indirect yet effective method for the detection of such NPs.

Selective functionalization of the cavities can be possibly achieved through the careful selection of template NPs, where NPs with a shell enriched with complementary functional groups serve as ideal templates. The idea revolves around the selective removal of these template NPs, leaving the remaining shell with tailored functionality for precise capture of analyte NPs. This system may enhance selectivity by eliminating non-specific adsorption by carefully choosing the matrix, paving the way for various applications in the field of NAIM.

# 9    Appendix

## A. Thickness Determination by AFM (Chapter 5)

Table A. AFM thickness determination of a) pph/cysteamine/polyplg/plg/GC b) pph/dithiol/polyplg/plg/GC and c) pph/polyplg/plg/GC.

| AFM thickness study | Thickness (nm) |
|---|---|
| a.  *pph/cysteamine/polyplg/plg/GC* | 20.0 |
| b.  *pph/dithiol/polyplg/plg/GC* | 22.0 |
| c.  *pph/polyplg/plg/GC* | 19.0 |

## B1.　Size Determination of the Cavities of NB/TIPS/ ( )/ITO (Chapter 7)
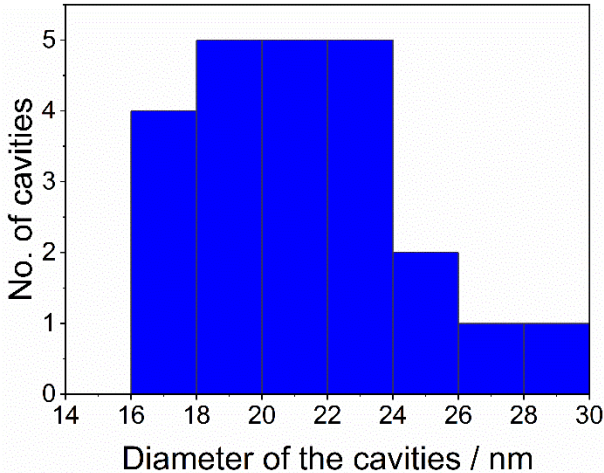


Figure B1. Size determination of the cavities of NB/TIPS/( )/ITO.

## B2.　Thickness Determination by AFM
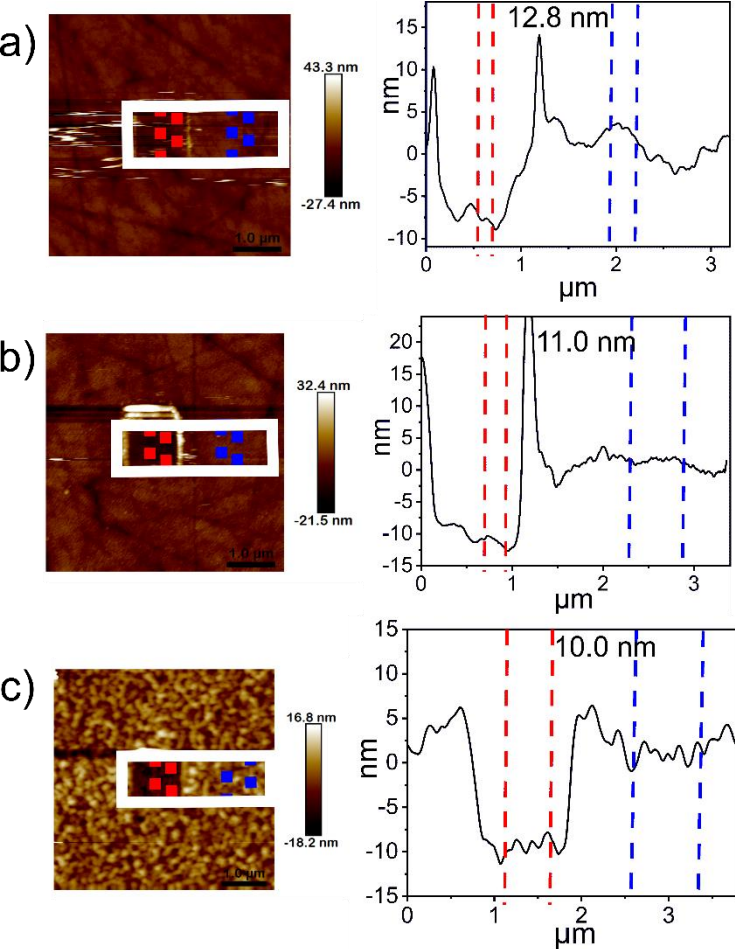


Figure B2. AFM thickness determination of a) ATP/(SiO$_2$-COOH)PDDA/GC b) *p*-pd/(SiO$_2$-COOH)PDDA/GC and c) NB/TIPS/ITO.

123

## B3. Electrodeposition of NB/TIPS Film
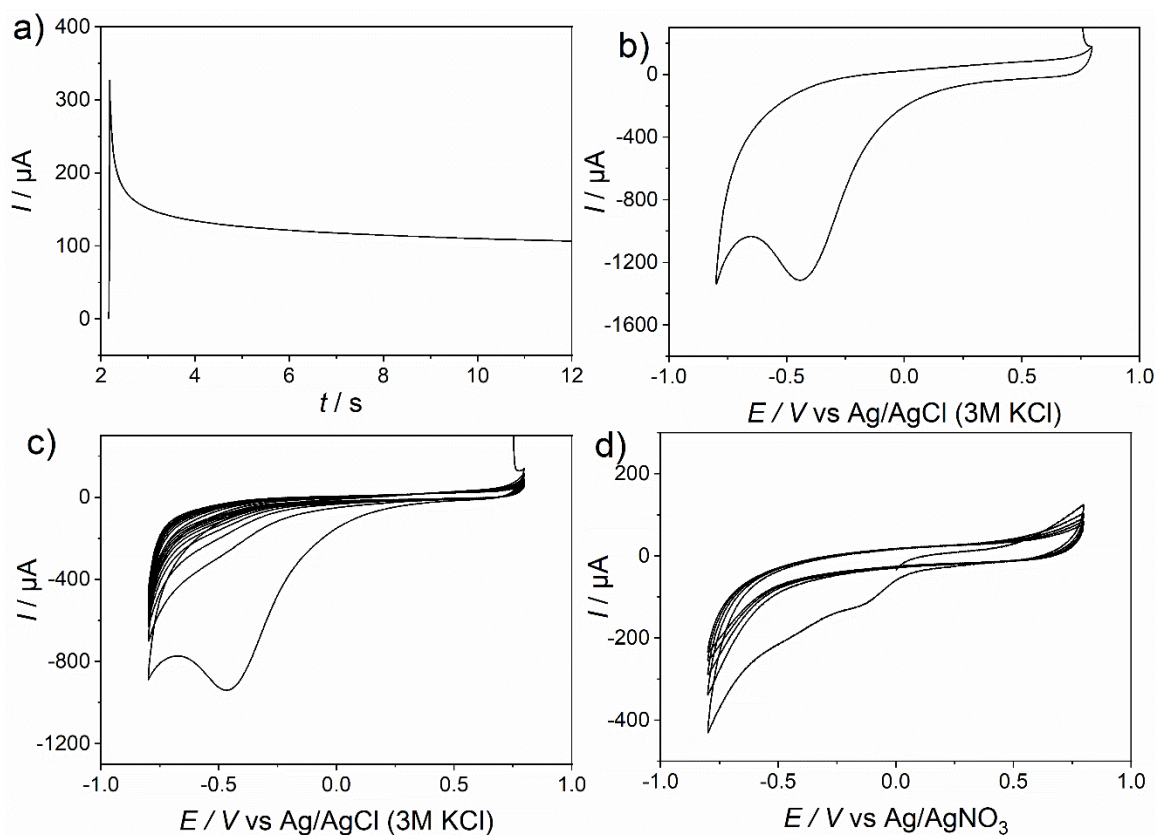


Figure B3. a) Chronoamperrogram recorded at 0.8 V applied for 10 s in 5 mM of 3-AP$^+$ + 10 mM NaNO$_2$ in 0.1 M HCl, b) cyclic voltammogram for the electrografting of 5 mM of 3-AP$^+$ + 10 mM NaNO$_2$ in 0.1 M HCl for the attachment of negatively charged SiO$_2$-COOH template NPs, c) cyclic voltammogram for the electrografting of 5 mM of 3-AP$^+$ + 10 mM NaNO$_2$ in 0.1 M HCl for the formation of initial 3-AP$^+$ based film and d) cyclic voltammogram for the electrografting of 0.01 M of NBD + 0.1 M TBAPF$_6$ in ACN for the formation of the binary layer.

## B4. Electrodeposition of ATP and *p*-pd Film
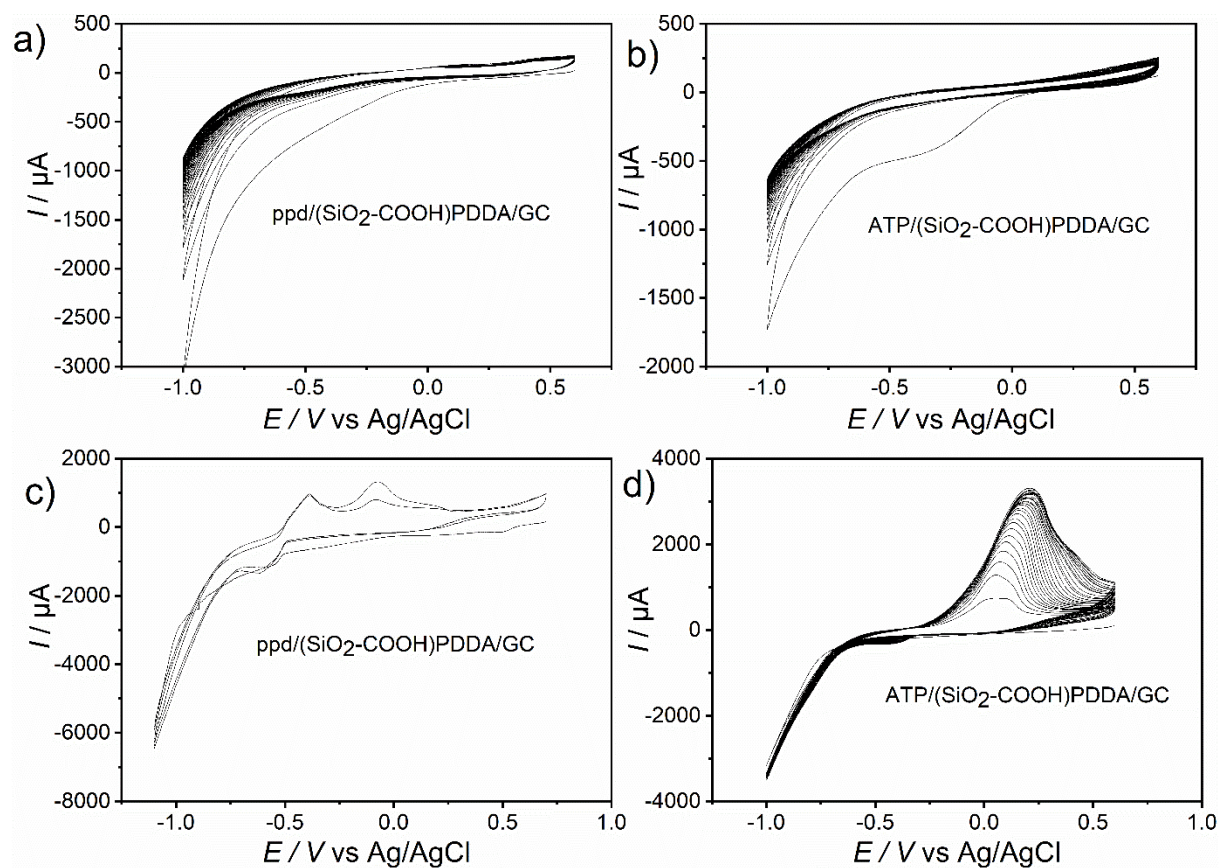


Figure B4. Successful cyclic voltammograms recorded during the electrodeposition of a) *p*-pd film on (SiO$_2$-COOH)PDDA/GC and b) ATP film on (SiO$_2$-COOH)PDDA/GC from 1 mM *p*-pd or ATP in 1 mM NaNO$_2$ + 0.5 M HCl. The appearance of unexpected additional peaks during the electrodeposition of *p*-pd or ATP can be observed in c) and d).

## 9.1   Abbreviation

| | |
|---|---|
| AFM | atomic force microscopy |
| Ag-CT | citric acid-tannic acid stabilized silver |
| $AgNO_3$ | silver nitrate |
| ATP | aminothiophenol |
| Au-Cit | citrate stabilized gold |
| $Au-NH_2$ | amine modified gold |
| CA | chronoamperometry |
| CV | cyclic voltammetry |
| cysteamine/polyplg/plg( )/GC | NAIM after the removal of $SiO_2-NH_2$ NPs from a cysteamine modified plumbagin based matrix on GC |
| cysteamine/polyplg/plg($SiO_2-NH_2$)/GC | NAIM formed from a cysteamine modified plumbagin-based matrix on $SiO_2-NH_2$ NPs attached GC |
| dithiol/polyplg/plg( )/GC | NAIM after the removal of $SiO_2-NH_2$ NPs from a dithiol modified plumbagin-based matrix on GC |
| dithiol/polyplg/plg($SiO_2-NH_2$)/GC | NAIM formed from a dithiol modified plumbagin-based matrix on $SiO_2-NH_2$ NPs attached GC |
| EDX | energy dispersive X-ray spectroscopy |
| FE-SEM | field emission scanning electron microscopy |
| GC | glassy carbon |
| ITO | indium tin oxide |
| LSV | linear sweep voltammetry |

| | |
|---|---|
| MIP | molecularly imprinted polymer |
| NAIM | nanoparticle-imprinted matrix |
| NB/TIPS/(SiO$_2$-COOH)PDDA/ITO | NAIM formed from a binary layer of 4-(triisopropylsilyl) ethynyl)benzene diazonium [BF4]$^-$ and nitrobenzene diazonium [BF4]$^-$ on SiO$_2$-NH$_2$ NPs attached GC |
| NB/TIPS/ITO | NAIM formed from a binary layer of 4-(triisopropylsilyl) ethynyl)benzene diazonium [BF4]$^-$ and nitrobenzene diazonium [BF4]$^-$ on GC |
| NBD | nitrobenzene diazonium [BF4]$^-$ |
| NPs | nanoparticles |
| PDA | polydopamine |
| PDDA | poly(diallyldimethylammonium chloride) |
| PDA/(PS)PDDA/ITO | NAIM formed from a polydopamine-based matrix on PS NP attached on PDDA modified ITO |
| plg | plumbagin |
| polyplg/plg( )/GC | NAIM after the removal of SiO$_2$-NH$_2$ NPs from a plumbagin-based matrix on GC |
| polyplg/plg(SiO$_2$-NH$_2$)/GC | NAIM formed from a dithiol modified plumbagin-based matrix on SiO$_2$-NH$_2$ NPs attached GC |
| p-pd | para phenylene diamine |
| p-pd/(SiO$_2$-COOH)PDDA/ITO | NAIM formed para phenylene diamine-based matrix on SiO$_2$-NH$_2$ NPs attached PDDA modified GC |
| p-pd/ITO | para phenylene diamine electrodeposited on ITO |
| p-pd/PS(PDDA)/ITO | NAIM formed from para phenylene diamine-based matrix on PS NP attached PDDA modified GC |

| | |
|---|---|
| pph | polyphenol |
| pph/PS(PDDA)/ITO | NAIM formed from polyphenol-based matrix on PS NP attached PDDA modified ITO. |
| PS NPs | polystyrene nanoparticles |
| PS/PDDA/ITO | polystyrene nanoparticles attached PDDA modified ITO |
| RAM | randomly arranged electrodes |
| SEM | scanning electron microscopy |
| $SiO_2$-COOH | carboxylate modified silica NPs |
| $SiO_2$-$NH_2$ | amine modified silica NPs |
| TEM | transmission electron microscopy |
| TIPS [BF4]- | 4-((triisopropylsilyl)ethynyl) benzenediazonium |
| XPS | x-ray photoelectron spectroscopy |
| ($SiO_2$-$NH_2$)/PDDA/ITO | amine modified silica NPs on PDDA modified ITO |
| 3-AP | 3-aminopyridine |
| 3-AP/PS(PDDA)/ITO | 3-aminopyridine based matrix formed on PS NP attached PDDA modified ITO |
| 4-ATP/($SiO_2$-COOH)PDDA/ITO | NAIM formed 4-aminothiophenol-based matrix on $SiO_2$-COOH NPs attached PDDA modified GC |

## 9.2 Symbols

| | |
|---|---|
| $\Delta_{Abbe}$ | abbe criterion |
| $A$ | electrode surface area |
| $c$ | bulk concentration |
| $c*$ | bulk concentration of the redox probe |
| $D$ | diffusion coefficient of the redox probe |
| $E_B$ | binding energy |
| $E_{kin}$ | kinetic energy |
| $E^{o'}$ | formal potential |
| $E_{pa}$ | anodic potential |
| $E_{pc}$ | cathodic potential |
| $F$ | Faraday constant |
| $i_d$ | diffusion-limited current at an inlaid electrode |
| $I_p$ | peak current |
| $i_{RAM}$ | diffusion-limited current at a recessed electrode |
| $j_{RAM}$ | expected current |
| $l$ | thickness of the film |
| $M_{Au}$ | molar mass of gold |
| $m_{NP}$ | mass of one gold NP |
| $n$ | no. of electrons involved in the reaction |
| $N_{atom}$ | amount of gold atoms in one gold NP |
| $Q_{NP}$ | charge required to remove one gold NP |
| $Q/A$ | charge density |
| $Q_{total}$ | integrated charge |

| | |
|---|---|
| $R$ | gas constant |
| $R(i)$ | residuals |
| $\Gamma^*$ | surface coverage of the adsorbed species |
| $v$ | scan rate |
| $V_{Au\ NP}$ | volume of gold NP |
| $X$ | ratio between the diffusion-limited currents at an inlaid nanodisk electrode and a recessed nanoelectrode |
| $\Gamma_{NP}$ | total number of electrochemically dissolved NPs |
| $\Pi$ | ratio of the active nanocavities |
| $\Phi$ | work function of the spectrometer |

# 10 References

[1] ISO, *Nanotechnologies — Vocabulary — Part 2: Nano-objects*, **2015**, ISO, Vernier, Geneva, Switzerland, can be found under https://standards.iteh.ai/catalog/standards/sist/b429a968-ba00-4b20-a4a3-72744d8d57b6/iso-ts-80004-2-2015.

[2] P. Kumar, A. Robins, S. Vardoulakis, R. Britter, *Atmos. Environ.* **2010**, *44*, 5035.

[3] J. M. Ngoy, N. Wagner, L. Riboldi, O. Bolland, *Energy Procedia* **2014**, *63*, 2230.

[4] A. K. Khan, R. Rashid, G. Murtaza, A. Zahra, *Trop. J. Pharm. Res.* **2014**, *13*, 1169.

[5] T. Patel, J. Zhou, J. M. Piepmeier, M. W. Saltzman, *Adv. Drug Delivery Rev.* **2012**, *64*, 701.

[6] A. V. Vergoni, G. Tosi, R. Tacchi, M. A. Vandelli, A. Bertolini, L. Costantino, *Nanomedicine (N. Y., NY, U. S.)* **2009**, *5*, 369.

[7] I. Khan, K. Saeed, I. Khan, *Arabian J. Chem.* **2019**, *12*, 908.

[8] W. J. Stark, P. R. Stoessel, W. Wohlleben, A. Hafner, *Chem. Soc. Rev.* **2015**, *44*, 5793.

[9] I. Ijaz, E. Gilani, A. Nazir, A. Bukhari, *Green Chem. Lett. Rev.* **2020**, *13*, 223.

[10] I. Matsui, *J. Chem. Eng. Jpn.* **2005**, *38*, 535.

[11] H. W. C. Postma, T. Teepen, Z. Yao, M. Grifoni, C. Dekker, *science* **2001**, *293*, 76.

[12] J.-H. Lee, H.-Y. Cho, H. K. Choi, J.-Y. Lee, J.-W. Choi, *Int. J. Mol. Sci.* **2018**, *19*.

[13] M. Sharifi, F. Attar, A. A. Saboury, K. Akhtari, N. Hooshmand, A. Hasan, M. A. El-Sayed, M. Falahati, *J. Controlled Release* **2019**, *311-312*, 170.

[14] V. Amendola, R. Pilot, M. Frasconi, O. M. Maragò, M. A. Iatì, *J. Phys.: Condens. Matter* **2017**, *29*, 203002.

[15] K. J. Fahnestock, M. Manesse, H. A. McIlwee, C. L. Schauer, R. Boukherroub, S. Szunerits, *Analyst* **2009**, *134*, 881.

[16] D. T. Thompson, *Nano Today* **2007**, *2*, 40.

[17] M. Boutonnet, S. Lögdberg, E. E. Svensson, *Curr. Opin. Colloid Interface Sci.* **2008**, *13*, 270.

[18] V. L. Colvin, *Nat. Biotechnol.* **2003**, *21*, 1166.

[19] G. Oberdörster, V. Stone, K. Donaldson, *Nanotoxicology* **2007**, *1*, 2.

[20] P. Khanna, C. Ong, B. H. Bay, G. H. Baeg, *Nanomaterials* **2015**, *5*, 1163.

[21] Z. Fu, H. L. Feng, X. D. Xiang, M. M. Rao, W. Wu, J. C. Luo, T. T. Chen, Q. P. Hu, A. B. Feng, W. S. Li, *J. Power Sources* **2014**, *261*, 170.

[22] P. P. Fu, Q. Xia, H.-M. Hwang, P. C. Ray, H. Yu, *J. Food Drug Anal.* **2014**, *22*, 64.

[23] A. Nel, T. Xia, L. Mädler, N. Li, *Science* **2006**, *311*, 622.

[24] M. C. Garnett, P. Kallinteri, *Occup. Med.* **2006**, *56*, 307.

[25] A. Sukhanova, S. Bozrova, P. Sokolov, M. Berestovoy, A. Karaulov, I. Nabiev, *Nanoscale Res. Lett.* **2018**, *13*, 44.

[26] X.-D. Zhang, Di Wu, X. Shen, P.-X. Liu, N. Yang, B. Zhao, H. Zhang, Y.-M. Sun, L.-A. Zhang, F.-Y. Fan, *Int. J. Nanomed.* **2011**, *6*, 2071.

[27] A. M. El Badawy, R. G. Silva, B. Morris, K. G. Scheckel, M. T. Suidan, T. M. Tolaymat, *Environ. Sci. Technol.* **2011**, *45*, 283.

[28] M. Sajid, M. Ilyas, C. Basheer, M. Tariq, M. Daud, N. Baig, F. Shehzad, *Environ. Sci. Pollut. Res.* **2015**, *22*, 4122.

[29] M. V. Park, A. M. Neigh, J. P. Vermeulen, L. J. de La Fonteyne, Verharen Henny W., J. J. Briedé, H. van Loveren, W. H. de Jong, *Biomaterials* **2011**, *32*, 9810.

[30] Y. Guo, M. Yang, R.-C. Xie, R. G. Compton, *Chem. Sci.* **2021**, *12*, 397.

[31] G. Gu, J. Song, M. Chen, X. Peng, H. Liang, J. Qu, *Nanoscale* **2018**, *10*, 14182.

[32] P. Zijlstra, M. Orrit, *Rep. Prog. Phys.* **2011**, *74*, 106401.

[33] S. K. Brar, M. Verma, *TrAC, Trends Anal. Chem.* **2011**, *30*, 4.

[34] C. Zhang, R. Zhu, W. Yang, *Sensors (Basel, Switzerland)* **2016**, *16*, 399.

[35] X. Xiao, A. J. Bard, *J. Am. Chem. Soc.* **2007**, *129*, 9610.

[36] D. Qiu, S. Wang, Y. Zheng, Z. Deng, *Nanotechnology* **2013**, *24*, 505707.

[37] Y.-G. Zhou, N. V. Rees, R. G. Compton, *Chem. Commun.* **2012**, *48*, 2510.

[38] S. Kraus-Ophir, J. Witt, G. Wittstock, D. Mandler, *Angew. Chem. Int. Ed.* **2014**, *53*, 294.

[39] M. Hitrik, Y. Pisman, G. Wittstock, D. Mandler, *Nanoscale* **2016**, *8*, 13934.

[40] D. Zelikovich, S. Dery, N. Bruchiel-Spanier, N. Tal, P. Savchenko, E. Gross, D. Mandler, *ACS Appl. Nano Mater.* **2021**, *4*, 10819.

[41] J. Witt, D. Mandler, G. Wittstock, *ChemElectroChem* **2016**, *3*, 2116.

[42] N. Bruchiel-Spanier, L. Dery, N. Tal, S. Dery, E. Gross, D. Mandler, *Nano Res.* **2019**, *12*, 265.

[43] R. Ginzburg-Turgeman, D. Mandler, *Phys. Chem. Chem. Phys.* **2010**, *12*, 11041.

[44] K. Haupt, K. Mosbach, *Chem. Rev.* **2000**, *100*, 2495.

[45] S. Tokonami, H. Shiigi, T. Nagaoka, *Anal. Chim. Acta* **2009**, *641*, 7.

[46] K. D. Shimizu, C. J. Stephenson, *Curr. Opin. Chem. Biol.* **2010**, *14*, 743.

[47] L. Uzun, A. P. F. Turner, *Biosens. Bioelectron.* **2016**, *76*, 131.

[48] N. Bruchiel-Spanier, D. Mandler, *ChemElectroChem* **2015**, *2*, 795.

[49] S. Palacin, C. Bureau, J. Charlier, G. Deniau, B. Mouanda, P. Viel, *ChemPhysChem* **2004**, *5*, 1468.

[50] G. Wulff, *Angew. Chem. Int. Ed.* **1995**, *34*, 1812.

[51] A. Bossi, F. Bonini, A. P. F. Turner, S. A. Piletsky, *Biosens. Bioelectron.* **2007**, *22*, 1131.

[52] K. Haupt, *Analyst* **2001**, *126*, 747.

[53] W. J. Cheong, S. H. Yang, F. Ali, *J. Sep. Sci.* **2013**, *36*, 609.

[54] J. J. BelBruno, *Chemical reviews* **2019**, *119*, 94.

[55] S. M. Marinakos, J. P. Novak, L. C. Brousseau, A. B. House, E. M. Edeki, J. C. Feldhaus, D. L. Feldheim, *J. Am. Chem. Soc.* **1999**, *121*, 8518.

[56] S. M. Marinakos, M. F. Anderson, J. A. Ryan, L. D. Martin, D. L. Feldheim, *J. Phys. Chem. B* **2001**, *105*, 8872.

[57] L. Sun, R. M. Crooks, V. Chechik, *Chem. Commun.* **2001**, 359.

[58] S. Koenig, V. Chechik, *Chem. Commun.* **2005**, 4110.

[59] D. Zelikovich, P. Savchenko, D. Mandler, *ACS applied materials & interfaces* **2023**, *15*, 32687.

[60] P. T. Kissinger, W. R. Heineman, *J. Chem. Educ.* **1983**, *60*, 702.

[61] A. J. Bard, L. R. Faulkner, *Electrochemical Methods. Fundamentals and Applications*, John Wiley & Sons, **2004**.

[62] O. Kasian, N. Kulyk, A. Mingers, A. R. Zeradjanin, K. J. Mayrhofer, S. Cherevko, *Electrochimica Acta* **2016**, *222*, 1056.

[63] P. Vanysek.

[64] G. Binnig, C. F. Quate, *Phys. Rev. Lett.* **1986**, *56*, 930.

[65] G. Binnig, H. Rohrer, *Helv. Phys. Acta* **1982**, *55*, 726.

[66] G. Binnig, H. Rohrer, *Angew. Chem. Int. Ed.* **1987**, *26*, 606.

[67] K. D. Jandt, *Surf. Sci.* **2001**, *491*, 303.

[68] J. C. Vickerman, I. S. Gilmore (Eds.) *Surface analysis: the principal techniques*, Wiley, Chichester, **2009**.

[69] B. Voigtländer, *Atomic Force Microscopy*, Springer Cham, **2019**.

[70] F. L. Leite, C. C. Bueno, A. L. Da Roz, E. C. Ziemath, Oliveira, Osvaldo N., Jr., *Int. J. Mol. Sci.* **2012**, *13*, 12773.

[71] T. R. Albrecht, C. F. Quate, *J. Vac. Sci. Technol., A* **1988**, *6*, 271.

[72] C. A. J. Putman, K. O. van der Werf, B. G. de Grooth, N. F. van Hulst, J. Greve, *Appl. Phys. Lett.* **1994**, *64*, 2454.

[73] I. Schmitz, M. Schreiner, G. Friedbacher, M. Grasserbauer, *Appl. Surf. Sci.* **1997**, *115*, 190.

[74] S.-L. Gao, E. Mäder, *Composites, Part A* **2002**, *33*, 559.

[75] D. Raghavan, X. Gu, T. Nguyen, M. VanLandingham, A. Karim, *Macromolecules* **2000**, *33*, 2573.

[76] E. Nagao, J. A. Dvorak, *Biophys. J.* **1999**, *76*, 3289.

[77] D. Briggs, J. T. Grant (Eds.) *Surface analysis by Auger and X-ray photoelectron spectroscopy*, IM Publ. [u.a.], Chichester [u.a.], **2003**.

[78] L. Chen, R. W. Hoffman, *J. Vac. Sci. Technol., A* **1993**, *11*, 2303.

[79] C. Jiang, M. T. Alam, S. G. Parker, N. Darwish, J. J. Gooding, *Langmuir : the ACS journal of surfaces and colloids* **2016**, *32*, 2509.

[80] M. T. Dang, J. Lefebvre, J. D. Wuest, *ACS Sustainable Chem. Eng.* **2015**, *3*, 3373.

[81] M. P. Seah, W. A. Dench, *Surface & Interface Analysis* **1979**, *1*, 2.

[82] R. Hesse, T. Chasse, P. Streubel, R. Szargan, *Surf. Interface Anal.* **2004**, *36*, 1373.

[83] R. Hesse, T. Chasse, R. Szargan, *Fresenius' J. Anal. Chem.* **1999**, *365*, 48.

[84] R. Hesse, P. Streubel, R. Szargan, *Surf. Interface Anal.* **2005**, *37*, 589.

[85] B. Singh, R. Hesse, M. Linford, *Vacuum Technology & Coating* **2015**.

[86] D. N. Leonard, G. W. Chandler, S. Seraphin in *Characterization of Materials* (Ed.: E. N. Kaufmann), **2012**.

[87] K. D. Vernon-Parry, *III-Vs Rev.* **2000**, *13*, 40.

[88] W. Zhou, Z. L. Wang, *Scanning Microscopy for Nanotechnology: Techniques and Applications*, Springer New York, **2007**.

[89] J. I. Goldstein, D. E. Newbury, J. R. Michael, N. Ritchie, J. Scott, D. C. Joy, *Scanning Electron Microscopy and X-Ray Microanalysis*, Springer New York, **2017**.

[90] A. M. Donald, *Nat. Mater.* **2003**, *2*, 511.

[91] D. B. Williams, C. B. Carter, *Transmission Electron Microscopy: A Textbook for Materials Science*, Springer, New York, **2009**.

[92] K. L. Klein, I. M. Anderson, N. de Jonge, *J. Microsc.* **2011**, *242*, 117.

[93]   G. H. Woehrle, J. E. Hutchison, S. ÖZKAR, R. G. FINKE, *Turk. J. Chem.* **2006**, *30*, 1.

[94]   W. D. Pyrz, D. J. Buttrey, *Langmuir* **2008**, *24*, 11350.

[95]   C. Schneider, W. Rasband, K. Eliceri, *Nat. Methods* **2012**, *9*, 671.

[96]   N. G. Bastús, J. Comenge, V. Puntes, *Langmuir* **2011**, *27*, 11098.

[97]   N. G. Bastús, F. Merkoçi, J. Piella, V. Puntes, *Chem. Mater.* **2014**, *26*, 2836.

[98]   T. Niidome, K. Nakashima, H. Takahashi, Y. Niidome, *Chem. Commun.* **2004**, 1978.

[99]   M. M. Ardakani, P. E. Karami, H. R. Zare, M. Hamzehloo, *Microchim. Acta* **2007**, *159*, 165.

[100]   S. Dongmo, J. Witt, G. Wittstock, *Electrochim. Acta* **2015**, *155*, 474.

[101]   J. Agullo, M. Morin, D. Bélanger, *ECS Trans.* **2011**, *35*, 19.

[102]   Y. R. Leroux, H. Fei, J.-M. Noël, C. Roux, P. Hapiot, *J. Am. Chem. Soc.* **2010**, *132*, 14039.

[103]   S. Anderson, *Chem. Eur. J.* **2001**, *7*, 4706.

[104]   Y. R. Leroux, F. Hui, J.-M. Noël, C. Roux, A. J. Downard, P. Hapiot, *Langmuir* **2011**, *27*, 11222.

[105]   G. Liu, E. Luais, J. J. Gooding, *Langmuir* **2011**, *27*, 4176.

[106]   S. A. Samuel, G. Wittstock, *ChemElectroChem* **2023**, *19*, e202300173/1-9.

[107]   S. Srivastava, D. Nykypanchuk, M. Fukuto, O. Gang, *ACS Nano* **2014**, *8*, 9857.

[108]   C. Barbero, R. Kötz, *J. Electrochem. Soc.* **1993**, *140*, 1.

[109]   C. Barbero, Silber, Juana, J., L. Sereno, *J. Electroanal. Chem.* **1988**, *248*, 321.

[110]   A. M. Abdel-Aziz, H. H. Hassan, I. H. A. Badr, *ACS Omega* **2022**, *7*, 34127.

[111]  L. F. Fieser, *J. Am. Chem. Soc.* **1928**, *50*, 439.

[112]   Alt, H., Binder, H., Köhling, A., Sandstede, G., *Electrochim. Acta* **1972**, *17*, 873.

[113]   J. Robertus, W. R. Browne, B. L. Feringa, *Chem. Soc. Rev.* **2010**, *39*, 354.

[114]   J. Davis, M. T. Molina, C. P. Leach, M. F. Cardosi, *ACS Appl. Mater. Interfaces* **2013**, *5*, 9367.

[115]   B. Piro, S. Reisberg, G. Anquetin, H.-T. Duc, M.-C. Pham, *Biosensors* **2013**, *3*, 58.

[116]   J. J. Inbaraj, C. F. Chignell, *Chem. Res. Toxicol.* **2004**, *17*, 55.

[117]   M. Ferreira, H. Varela, R. M. Torresi, G. Tremiliosi-Filho, *Electrochim. Acta* **2006**, *52*, 434.

[118]   L. A. A. Newton, E. Cowham, D. Sharp, R. Leslie, J. Davis, *New J. Chem.* **2010**, *34*, 395.

[119]   S. Dongmo, J. Leyk, C. Dosche, C. Richter-Landsberg, U. Wollenberger, G. Wittstock, *Electroanalysis* **2016**, *28*, 2400.

[120]   P. N. Bartlett, J. M. Cooper, *J. Electroanal. Chem.* **1993**, *362*, 1.

[121]   M. S. Damle, L. A. A. Newton, M. M. Villalba, R. Leslie, J. Davis, *Electroanalysis* **2010**, *22*, 2491.

[122]   J. C. Harfield, C. Batchelor-McAuley, R. G. Compton, *Analyst* **2012**, *137*, 2285.

[123]   K. A. Joshi, P. C. Pandey, W. Chen, A. Mulchandani, *Electroanalysis* **2004**, *16*, 1938.

[124]   Lawrence, Nathan, S., J. Davis, R. G. Compton, *Talanta* **2001**, *53*, 1089.

[125]   P. T. Lee, D. Lowinsohn, R. G. Compton, *Analyst* **2014**, *139*, 3755.

[126]   A. Hammami, N. Raouafi, V. M. Mirsky, *Biosens. Bioelectron.* **2018**, *121*, 72.

[127]   K. Gong, X. Zhu, R. Zhao, S. Xiong, L. Mao, C. Chen, *Anal. Chem.* **2005**, *77*, 8158.

[128]   J. E. Baio, T. Weidner, J. Brison, D. J. Graham, L. J. Gamble, D. G. Castner, *J. Electron Spectrosc. Relat. Phenom.* **2009**, *172*, 2.

[129]   N. Hellgren, R. T. Haasch, S. Schmidt, L. Hultman, I. Petrov, *Carbon* **2016**, *108*, 242.

[130]   Lindberg B. J., Hamrun K., Johansson G., Gelius U., Fahlman A., Nordling C., Siegbahn K., *Phys. Scr.* **1970**, *1*, 286.

[131]   S. Ahl, P. J. Cameron, J. Liu, W. Knoll, J. Erlebacher, F. Yu, *Plasmonics* **2008**, *3*, 13.

[132]   D. W. M. Arrigan, P. N. Bartlett, *Biosens. Bioelectron.* **1998**, *13*, 293.

[133]   R. J. Geise, J. M. Adams, N. J. Barone, A. M. Yacynych, *Biosens. Bioelectron.* **1991**, *6*, 151.

[134]   P. N. Bartlett, P. Tebbutt, C. H. Tyrrell, *Anal. Chem.* **1992**, *64*, 138.

[135]   *DGUV Information 213-071 Fluorwasserstoff, Flusssäure und anorganische Fluoride (Merkblatt M 005 der Reihe "Gefahrstoffe")*, **2018**.

[136]   S. Verhaverbeke, Teerlinck, I., Vinckier, C., G. Stevens, R. Cartuyvels, M. M. Heyns, *J. Electrochem. Soc.* **1994**, *141*, 2852.

[137]   Y.-G. Zhou, N. V. Rees, J. Pillay, R. Tshikhudo, S. Vilakazi, R. G. Compton, *Chem. Commun.* **2012**, *48*, 224.

[138]   J.-W. Park, J. S. Shumaker-Parry, *ACS Nano* **2015**, *9*, 1665.

[139]   Y. Xue, X. Li, H. Li, W. Zhang, *Nat. Commun.* **2014**, *5*, 4348.

[140]   J. J. Gooding, M. T. Alam, A. Barfidokht, L. Carter, *J. Braz. Chem. Soc.* **2013**, *25*, 418.

[141]   J. Kim, A. J. Bard, *J. Am. Chem. Soc.* **2016**, *138*, 975.

[142]   K. Z. Brainina, L. G. Galperin, E. V. Vikulova, *J. Solid State Electrochem.* **2012**, *16*, 2357.

[143]   L. Kankate, A. Turchanin, A. Goelzhauser, *Langmuir* **2009**, *25*, 10435.

[144]   F. Tielens, E. Santos, *J. Phys. Chem. C* **2010**, *114*, 9444.

[145]   G. I. Sakellari, N. Hondow, P. H. Gardiner, *Chemosensors* **2020**, *8*, 80.

[146]   L. Dery, N. Shauloff, Y. Turkulets, I. Shalish, R. Jelinek, D. Mandler, *ACS Sens.* **2022**, *7*, 296.

[147]   K. Kik, B. Bukowska, P. Sicińska, *Environ. Pollut. (Oxford, U. K.)* **2020**, *262*, 114297.

[148]   P. M. van Midwoud, A. Janse, M. T. Merema, G. M. M. Groothuis, E. Verpoorte, *Anal. Chem.* **2012**, *84*, 3938.

[149]   C. Loos, T. Syrovets, A. Musyanovych, V. Mailänder, K. Landfester, G. U. Nienhaus, T. Simmet, *Beilstein J. Nanotechnol.* **2014**, *5*, 2403.

[150]   M. T. Charreyre, J. Revilla, A. Elaissari, C. Pichot, Gallot B., *J. Bioact. Compat. Polym.* **1999**, *14*, 64.

[151]   S. Moulay, *Polym.-Plast. Technol. Eng. (Polymer-Plastics Technology and Engineering)*, *57*, 1045.

[152]   L. Pei, C. A. Lucy, *J. Chromatogr. A* **2014**, *1365*, 226.

[153]   B. B. Berkes, A. S. Bandarenka, G. Inzelt, *J. Phys. Chem. C* **2015**, *119*, 1996.

[154]   T. Osaka, *Electrochim. Acta* **1997**, *42*, 3015.

[155]   M. Li, M. Dincă, *Chem. Sci.* **2014**, *5*, 107.

[156]   R. Batul, T. Tamanna, A. Khaliq, A. Yu, *Biomaterials science* **2017**, *5*, 1204.

[157]   H. Lee, S. M. Dellatore, W. M. Miller, P. B. Messersmith, *Science* **2007**, *318*, 426.

[158]   W. Yang, C. Liu, Y. Chen, *Langmuir* **2018**, *34*, 3565.

[159]   S. Li, H. Wang, M. Young, F. Xu, G. Cheng, H. Cong, *Langmuir* **2019**, *35*, 1119.

[160]   M. D. Hawley, S. V. Tatawawadi, S. Piekarski, R. N. Adams, *J. Am. Chem. Soc.* **1967**, *89*, 447.

[161]   T. Łuczak, *Electrochim. Acta* **2008**, *53*, 5725.

[162]   G. Wittstock, P. Gründler, *Nachr. Chem.* **2002**, *50*, 1353.

[163]   Y. Saito, *Rev. Polarogr.* **1968**, *15*, 177.

[164]   Z. Wang, C. Li, J. Xu, K. Wang, X. Lu, H. Zhang, S. Qu, G. Zhen, F. Ren, *Chem. Mater.* **2015**, *27*, 848.

[165]   C. Xie, P. Li, L. Han, Z. Wang, T. Zhou, W. Deng, K. Wang, X. Lu, *NPG Asia Mater.* **2017**, *9*, e358.

[166]   R. A. Zangmeister, T. A. Morris, M. J. Tarlov, *Langmuir* **2013**, *29*, 8619.

[167]   X.-G. Li, M.-R. Huang, W. Duan, Y.-L. Yang, *Chem. Rev.* **2002**, *102*, 2925.

[168]   Q. L. Pham, Y. Haldorai, H. van Nguyen, D. Tuma, J.-J. Shim, *Bull. Mater. Sci.* **2011**, *34*, 37.

[169]   N. Shaabani, N. W. C. Chan, W. E. Lee, A. B. Jemere, *J. Electrochem. Soc.* **2020**, *167*, 137508.

[170]   L. M. Samyn, R. S. Babu, M. Devendiran, A. L. F. de Barros, *Ionics* **2020**, *26*, 3041.

[171]   B. Lakard, G. Herlem, S. Lakard, B. Fahys, *J. Mol. Struct.: THEOCHEM* **2003**, *638*, 177.

[172]   M. Hazarika, K. Malkappa, T. Jana, *Polym. Int.* **2012**, *61*, 1425.

[173]   X. Lu, R. A. Weiss, *Macromolecules* **1991**, *24*, 4381.

[174]   M. Hazarika, D. Arunbabu, T. Jana, *J. Colloid Interface Sci.* **2010**, *351*, 374.

[175]   M. M. Chehimi (Ed.) *Aryl Diazonium Salts. New Coupling Agents in Polymer and Surface Science*, WILEY-VCH Verlag GmbH & Co. KGaA, Weinheim, Germany, **2012**.

[176]   J. Pinson, F. Podvorica, *Chem. Soc. Rev.* **2005**, *34*, 429.

[177]   T. Menanteau, M. Dias, E. Levillain, A. J. Downard, T. Breton, *J. Phys. Chem. C* **2016**, *120*, 4423.

[178]   J. Agullo, S. Canesi, F. Schaper, M. Morin, D. Bélanger, *Langmuir* **2012**, *28*, 4889.

[179]   H. Smida, E. Lebègue, J.-F. Bergamini, F. Barrière, C. Lagrost, *Bioelectrochemistry* **2018**, *120*, 157.

[180]   W. E. E. Stone, J. H. Stone-Masui in *Science and Technology of Polymer Colloids: Characterization, Stabilization and Application Properties* (Eds.: G. W. Poehlein, R. H. Ottewill, J. W. Goodwin), Springer Netherlands, Dordrecht, **1983**, pp. 480–502.

[181]   J. Moulder, W. M. Stickle, P. E. Sobol, K. D. Bomben, *Handbook of X-ray Photoelectron Spectroscopy*, Physical Electronics, **1995**.

[182]  M. A. Jafar Mazumder, H. Sheardown, A. Al-Ahmed, *Functional Polymers*, Springer International Publishing, Cham, **2019**.

[183]  S. H. Piao, C. Y. Gao, H. J. Choi, *Polymer* **2017**, *127*, 174.

[184]  A. Cernat, E. Bodoki, C. Farcau, S. Aştilean, S. Griveau, F. Bedioui, R. Săndulescu, *J. Nanosci. Nanotechnol.* **2015**, *15*, 3359.

[185]  L. Santos, J. Ghilane, J.-C. Lacroix, *Electrochem. Commun.* **2012**, *18*, 20.

[186]  M. Ben Haddada, J. Blanchard, S. Casale, J.-M. Krafft, A. Vallée, C. Méthivier, S. Boujday, *Gold Bull.* **2013**, *46*, 335.

[187]  K. Ranoszek-Soliwoda, E. Tomaszewska, E. Socha, P. Krzyczmonik, A. Ignaczak, P. Orlowski, M. Krzyzowska, G. Celichowski, J. Grobelny, *J. Nanopart. Res.* **2017**, *19*, 273.

[188]  M. Smith, J. March, *March's advanced organic chemistry. Reactions, mechanisms, and structure*, Wiley-Interscience, Hoboken N.J., **2007**.

[189]  D. F. Acevedo, C. R. Rivarola, M. C. Miras, C. A. Barbero, *Electrochimica Acta* **2011**, *56*, 3468.

[190]  M. Delamar, R. Hitmi, J. Pinson, J. M. Saveant, *J. Am. Chem. Soc.* **1992**, *114*, 5883.

[191]  J. Pinson in *Aryl Diazonium Salts. New Coupling Agents in Polymer and Surface Science* (Ed.: M. M. Chehimi), WILEY-VCH Verlag GmbH & Co. KGaA, Weinheim, Germany, **2012**, pp. 1–35.

[192]  P. Allongue, M. Delamar, B. Desbat, O. Fagebaume, R. Hitmi, J. Pinson, J.-M. Saveant, *J. Am. Chem. Soc.* **1997**, *119*, 201.

[193]  Y.-C. Liu, R. L. McCreery, *J. Am. Chem. Soc.* **1995**, *117*, 11254.

[194]  M. Toupin, D. Bélanger, *J. Phys. Chem. C* **2007**, *111*, 5394.

[195]  Z. Li, W. Yan, S. Dai, *Langmuir* **2005**, *21*, 11999.

[196]  M.-C. Bernard, A. Chaussé, E. Cabet-Deliry, M. M. Chehimi, J. Pinson, F. Podvorica, C. Vautrin-UI, *Chem. Mater.* **2003**, *15*, 3450.

[197]  A. Ghorbal, F. Grisotto, M. Laudé, J. Charlier, S. Palacin, *J. Colloid Interface Sci.* **2008**, *328*, 308.

[198]  M. Ceccato, A. Bousquet, M. Hinge, S. U. Pedersen, K. Daasbjerg, *Chem. Mater.* **2011**, *23*, 1551.

[199]  S. Smołka, K. Krukiewicz, *Int. J. Mol. Sci.* **2023**, *24*, 12575.

[200]  J. Su, J. C. Calderón Gómez, G. Grundmeier, A. González Orive, *Nanomaterials* **2021**, *11*.

[201]  A. Chaussé, M. M. Chehimi, N. Karsi, J. Pinson, F. Podvorica, C. Vautrin-Ul, *Chem. Mater.* **2002**, *14*, 392.

[202]  F. Le Floch, G. Bidan, L. Pilan, E.-M. Ungureanu, J.-P. Simonato, *Mol. Cryst. Liq. Cryst.* **2008**, *486*, 271/[1313]-281/[1323].

[203]  D. Hetemi, V. Noël, J. Pinson, *Biosensors* **2020**, *10*, 1.

[204]  A. M. Mahmoud, A. J. Bergren, N. Pekas, R. L. McCreery, *Adv. Funct. Mater.* **2011**, *21*, 2273.

[205]  J. K. Kariuki, M. T. McDermott, *Langmuir* **2001**, *17*, 5947.

[206]  J. K. Kariuki, M. T. McDermott, *Langmuir* **1999**, *15*, 6534.

[207]  P. Allongue, C. Henry de Villeneuve, G. Cherouvrier, R. Cortès, M.-C. Bernard, *J. Electroanal. Chem.* **2003**, *550-551*, 161.

[208]  P. A. Brooksby, A. J. Downard, *Langmuir* **2004**, *20*, 5038.

[209]  F. Anariba, S. H. DuVall, R. L. McCreery, *Anal. Chem.* **2003**, *75*, 3837.

[210]  C. Combellas, D. Jiang, F. Kanoufi, J. Pinson, F. Podvorica, *Langmuir* **2009**, *25*, 286.

[211]  C. Combellas, F. Kanoufi, J. Pinson, F. I. Podvorica, *J. Am. Chem. Soc.* **2008**, *130*, 8576.

[212]  Y. R. Leroux, P. Hapiot, *Chem. Mater.* **2013**, *25*, 489.

[213]  B. Ortiz, C. Saby, G. Y. Champagne, D. Bélanger, *J. Electroanal. Chem.* **1998**, *455*, 75.

[214]  S. S. C. Yu, E. S. Q. Tan, R. T. Jane, A. J. Downard, *Langmuir* **2007**, *23*, 11074.

[215]  T. Menanteau, E. Levillain, A. J. Downard, T. Breton, *Phys. Chem. Chem. Phys.* **2015**, *17*, 13137.

[216]  H. Tanaka, A. Aramata, *J. Electroanal. Chem.* **1997**, *437*, 29.

[217]  F. Geneste, C. Moinet, G. Jezequel, *New J. Chem.* **2002**, *26*, 1539.

[218]  A. Yeşildağ, D. Ekinci, *Electrochimica Acta* **2010**, *55*, 7000.

# 11 Own Publication and Conference Contributions

## 11.1 Publication

- Samuel, S. A., Wittstock, G. Covalent Modification of Nanoparticle-Imprinted Matrices for Selective Nanoparticle Recognition, *ChemElectroChem*, e202300173."

## 11.2 Oral Presentations

- S.A. Samuel, G. Wittstock; "Polydopamine-Based Matrix for Size Selective Recognition of Nanoparticles", 72nd Annual Meeting of the ISE, 2021.
- S.A. Samuel, G. Wittstock; "Study of Matrix-Nanoparticle Interactions with a Thiol Modified Plumbagin Based Nanoparticle-Imprinted Matrix", Regional Meeting of the ISE, Prague, Czech Republic, 2022.
- S.A. Samuel, G. Wittstock; "Study of Matrix-Nanoparticle Interactions with a Thiol Modified Plumbagin Based Nanoparticle-Imprinted Matrix", 73rd Annual Meeting of the ISE, 2022.

## 11.3 Poster Presentations

- S.A. Samuel, G. Wittstock; "Selective Recognition by Nanoparticle-Imprinted Matrices", 71st Annual Meeting of the ISE, 2020.
- S.A. Samuel, G. Wittstock; "Selective Recognition by Nanoparticle-Imprinted Matrices", GDCh Electrochemistry Undercover, 2020.

## 11.4 Award

- Best Poster Prize (GDCh Electrochemistry Undercover 23 – 24 September 2020)

# 12   Erklärung

Hiermit erkläre ich, dass ich die vorliegende Dissertation selbstständig verfasst und die hierfür benutzten Hilfsmittel vollständig angegeben habe. In Teilen wurde die vorliegende Arbeit bereits veröffentlicht. Diese Teile betreffen die im Kapitel 11.1 "Publication". Ich erkläre außerdem, dass die Dissertation weder in ihrer Gesamtheit noch in Teilen einer anderen Hochschule zur Begutachtung in einem Promotionsverfahren vorliegt oder vorgelegen hat. Die Leitlinien guter wissenschaftlicher Arbeit der Carl von Ossietzky Universität Oldenburg wurden befolgt und im Zusammenhang mit dem Promotionsvorhaben sind keine kommerziellen Vermittlungs- oder Beratungsdienste in Anspruch genommen worden.

Oldenburg, den 17.07.2024                                          Sweety Ann Samuel